



<https://theses.gla.ac.uk/>

Theses Digitisation:

<https://www.gla.ac.uk/myglasgow/research/enlighten/theses/digitisation/>

This is a digitised version of the original print thesis.

Copyright and moral rights for this work are retained by the author

A copy can be downloaded for personal non-commercial research or study, without prior permission or charge

This work cannot be reproduced or quoted extensively from without first obtaining permission in writing from the author

The content must not be changed in any way or sold commercially in any format or medium without the formal permission of the author

When referring to this work, full bibliographic details including the author, title, awarding institution and date of the thesis must be given

Enlighten: Theses

<https://theses.gla.ac.uk/>
research-enlighten@glasgow.ac.uk

Behaviour of Bioceramics Under Impact Loading

by

Jin Siong Soh

**Thesis submitted to the Faculty of Engineering, University of Glasgow
for Degree of Master of Science**

December 1997

ProQuest Number: 10391166

All rights reserved

INFORMATION TO ALL USERS

The quality of this reproduction is dependent upon the quality of the copy submitted.

In the unlikely event that the author did not send a complete manuscript and there are missing pages, these will be noted. Also, if material had to be removed, a note will indicate the deletion.



ProQuest 10391166

Published by ProQuest LLC (2017). Copyright of the Dissertation is held by the Author.

All rights reserved.

This work is protected against unauthorized copying under Title 17, United States Code
Microform Edition © ProQuest LLC.

ProQuest LLC.
789 East Eisenhower Parkway
P.O. Box 1346
Ann Arbor, MI 48106 – 1346

GLASGOW UNIVERSITY
LIBRARY

-11297 (copy 2)

i. Acknowledgement

It is my greatest privilege to be under the supervision of *Dr. R.D Thomson*. Deepest appreciation for his kindness, patience and many more. Special thanks to *para Alan Birkbeck, Jesper Ankersen* and *Tim Lucas*. And also thanks to members of the staff in the Mechanical Engineering Department, Glasgow University, Scotland.

ii. Abstract

Stabbing incidents are of continued concern and the need to quantify the force required to cause a stab-wound is increasingly urgent. Only through an understanding of the mechanics of penetration of human tissue can forensic engineers and pathologists infer, after the event, whether any particular wound track is likely to have been due to homicide, suicide or accident.

In stabbing incidents, the main resistance to knife penetration is provided by bone tissue. Structurally, bone is a complex material. It is neither as brittle as a monolithic ceramic nor as ductile as a polymer. Rather, it lies within an intermediate class of material that the author has called "near-brittle" and which exhibits limited damage evolution up to failure. A computational constitutive model of near-brittle bone must be benchmarked against experiments on the real material but it is prudent to perform preliminary static and impact tests on simpler model materials which mimic, in at least one aspect, the behaviour of bone. To bracket this behaviour, for which very little relevant data is available, experiments were therefore done on the two extreme cases, ie brittle monolithic ceramics and ductile polymers. At the same time, experience in computational constitutive modelling of a damaging material was gained using pre-existing data on the static behaviour of a ceramic composite. Though quantitatively different from bone, this has a qualitatively similar near-brittle response.

The experimental work on ductile materials raised the contentious question of the role of kinetic energy versus momentum during impact. While damage certainly increases with kinetic energy, there may also be a small increase with momentum. There is no simple explanation for any such effect and the results are not conclusive but they do point the way towards additional work.

The computational modelling proved difficult. The damage model used by Gibson & Thomson (1995) is erroneous but attempts to devise an accurate substitute were hampered by the nature of the explicit finite element solver. The work concludes with experiments on real bone under static and impact loading, to generate data which is essential if this objective is to be eventually met.

iii. Contents

- i. Acknowledgement
- ii. Abstract
- iii. Content Pages

Chapter 1- Introduction

- 1.1 Background and Motivation
- 1.2 Objective
- 1.3 Brief Introduction to Continuum Damage Mechanics

Chapter 2 - Experiments On Model Materials

- 2.1 Model Materials
- 2.2 The Impact Rig
- 2.3 Blade Profile
- 2.4 The Velocities and Kinetic Energy of The Crosshead Assembly At Impact
 - 2.4.1 Domestic Video Recording Technique
 - 2.4.1.1 Discussion
 - 2.4.2 High Speed Video Camera Technique
 - 2.4.2.1 Results And Discussion
- 2.5 Impact Tests
 - 2.5.1 Test On Domestic Tiles
 - 2.5.1.1 Protocol And Results
 - 2.5.1.2 Discussions And Conclusions
 - 2.5.2 Tests On Aluminium Nitride Machinable Ceramic
 - 2.5.2.1 Protocol And Results
 - 2.5.2.2 Discussions And Conclusions
 - 2.5.3 Alumina Ceramic
 - 2.5.3.1 Protocol And Results
 - 2.5.3.2 Discussions And Conclusions
- 2.6 The Role of Momentum Vs KE In Impact Resistance
 - 2.6.1 Protocol And Results
 - 2.6.2 Discussions And Conclusions

Chapter 3 - Damage Propagation In Toughened Ceramic

- 3.1 Introduction
- 3.2 Dupont Lanxide Corporation Composite
 - 3.2.1 Composite Manufacture
 - 3.2.2 Three-Point Bend On Dupont Lanxide Composite
- 3.3 Experimental Results
- 3.4 Damage Propagation In Three-Point Bend
 - 3.4.1 Continuum Damage Mechanics
- 3.5 Finite Element Analysis
 - 3.5.1 Introduction
 - 3.5.2 Computational Modelling Of Damage Propagation
 - 3.5.3 Conclusions

Chapter 4 - Constitutive Modelling Of A Damaging Almost-Brittle Ceramic

4.1 Introduction

4.2 Finite Element Analysis

4.2.1 Mesh Generation And Boundary Conditions

4.2.2 Vumat Subroutine File

4.3 Determination Of Damage Evolution Law By FEA

4.3.1 Mesh Size

4.3.1.1 Results And Discussions

4.3.2 Damage Evolution Rate

4.3.2.1 Discussions And Results

4.3.3 The Sensitivity Of The Results To Matrix Microcracking Stress

4.3.3.1 Results And Discussions

4.4 Conclusions

Chapter 5 - Damage In Multiaxial Stress State

5.1 Introduction

5.2 Three-Point Bending On T-Sections

5.3 Finite Element Analysis

5.3.1 Results And Discussions

5.4 Conclusions

Chapter 6 - The Constitutive Modelling Of Bone

6.1 Introduction

6.2 Macrostructure Of Bone

6.3 Compact Bone

6.3.1 Biological Structure

6.3.2 Mechanical Structure

6.4 Preparation Of Bone Specimen

6.4.1 Compact

6.4.2 Ribs

6.4.3 Conclusions On Specimen Selection And Preparation

6.5 Experiments On Compact Bone

6.5.1 Monotonic Loading

6.5.1.1 Results And Conclusions

6.5.2 Cyclic Loading Test

6.5.2.1 Results And Discussions

6.6 Experiments On Ribs

6.6.1 Monotonic Loading

6.6.1.1 Results And Discussions

6.6.2 Cyclic Loading

6.6.2.1 Results And Conclusions

6.6.3 Impact Test

6.7 Conclusions

Chapter 7- Final Conclusions

References

Appendix

Chapter One

INTRODUCTION

1.1. Background And Motivation

Until the twentieth century, the aim of materials scientists and engineers was to produce materials, mainly metals, of increased strength suitable for the increasingly arduous loads imposed on machine components following the industrial revolution. However, in practice, components made from high strength materials using a "strength of materials" approach to design, were often prone to unexpected and catastrophic failures.

It was eventually realised that strength alone was not sufficient to guarantee safety particularly in a material which fails in a brittle manner. The necessary paradigm shift in engineering design was to adopt a "fracture mechanics" approach based on the pioneering work of Griffith (1920), G.R Irwin (1973) etc. This showed that, in addition to strength, it was necessary to retain some ductility in the material to allow for the inevitable presence of crack-like defects. Materials with both strength and ductility are said to be "tough".

This might seem to imply that brittle materials are not of any use but there are a number of fields in which brittleness is tolerated because it is not a practical disadvantage, or because any disadvantage is outweighed by other advantages or even simply because there is no option. Engineering ceramics, for example, offer a combination of high melting point, chemical stability, strength and extreme hardness which makes them prime candidates for use in extreme thermomechanical service environments and their use is increasing in such applications as aero- and auto-engines, particularly if the component is under largely compressive loads (as is a piston crown).

Unfortunately, these desirable properties are associated with low fracture toughness, which makes ceramic components sensitive to the presence of tensile stresses resulting from service loads, from manufacturing defects in multiaxial states of stress or from accidental impact damage. Monolithic ceramic components are then problematic and it is necessary to use composite systems.

However these need not be woven composites and for many years, aero-engines such as the Rolls-Royce RB211 have used non-structural ceramic coatings as thermal barriers in metallic combustion chambers and turbine stator blades. Such coatings modify the film coefficients and so eliminate the need for the cooling air required with uncoated components.

If the service loads are likely to include significant tensile components, it is desirable to improve the toughness of the main structural materials by such means as fibre-toughening. Here, a ceramic matrix such as Al_2O_3 is deposited onto a mesh of ceramic fibres such as SiC. At stresses in excess of the "matrix microcracking stress", the matrix cracks and the fibres either break progressively or pull out of the matrix, giving a degree of inelastic behaviour and toughness. Such materials are described by Mecholsky (1986). Recently, McCafferty & Hancock (1994) and Gibson & Thomson (1995), who showed that the materials retain their ductility at high temperatures but that manufacturing defects can degrade the performance of components made from them.

In another context, the very brittleness of engineering ceramics is a positive advantage and recently, composite armours comprising a sandwich of ceramic, metals and polymers have been developed to provide protection from ballistic projectiles both in military and civilian industrial applications.

For example, the effectiveness of a long rod penetrator, such as the depleted uranium darts which form the main armour-defeating component of modern anti-tank weapons, is largely dependent on the kinetic energy density and hence on the sharpness of the tip. This tip can be blunted and indeed the whole dart eroded by the abrasive particles which form ahead of it as it pulverises a hard ceramic such as Al_2O_3 .

At lower ballistic velocities, typical of small-arms bullets or of the fragments which can detach from high-speed machinery in industrial accidents, a similar effect is observed and most of the ballistic armours and protective clothing rely on a hard but heavy layer of engineering ceramic. Such protection is uncomfortable and degrades the wearer's performance after prolonged use. Furthermore, bullets are not particularly sharp and can be more effectively stopped by woven fabric armours. However these are not particularly effective at stopping sharp objects such as the flechettes which are of increasing military significance. Nor are they particularly effective against attack by a sharp instrument such as a knife blade. In these circumstances, there remains a need to understand the behaviour of brittle materials under impact loading.

Forensic case studies have shown that the main barrier to injury by a sharp object such as a knife blade is the skin or clothing. If this is punctured, the underlying tissue offers very little resistance until bone is met. While not strictly a ceramic in the sense that it is not fired, bone is mechanically similar to toughened engineering ceramics and the penetration behaviour of human bone provides a challenging scientific focus for the current work.

In addition, an understanding of the penetration mechanics of bone would go a long way to solving a serious practical problem in forensic medicine. The lack of quantitative knowledge of the force needed for a sharp instrument to penetrate human tissue (and clothing) makes it impossible to model stabbing mathematically with any degree of confidence. This presents a problem in forensic pathology since it is impossible to infer, after the event, whether a specific wound was necessarily the result of a deliberate blow.

The common defence "he fell upon the knife" then becomes difficult to challenge in cases where evidence suggests otherwise. The requirement is for a quantitative method of assessing the force used in any stabbing incident.

This will reduce the margin of doubt, both in single stabbing "alleged accidental" cases and in multiple stabbings where the effort required and hence the speed of repetition of the blow, is often a critical factor (Fig 1). A quantitative force assessment method should therefore lead to speedier resolution of cases and, by reducing to subjectivity of expert opinion, improve the soundness of the verdict. In addition, sounder knowledge of the forces involved in the production of stab wounds, in relation to location on the body and likely damage to underlying structures, would enable clinicians to make a more rapid and appropriate assessment of the severity of injury. This is important since unnecessary deaths still occur from time to time in cases where the stab wound track length and the severity of trauma to the underlying structures had not been fully appreciated.



Fig 1 Multiple Stabbed Wound

1.2 Objectives

Research of the constitutive modelling of the impact of knife blade on human tissues, mainly skin, has been carried out for the past few decades (e.g Green (1978) and Knights(1975)). The purpose here was to quantify the forces involved in the infliction of particular wounds which will contribute vital information to forensic pathologists, as well as the Court.

It was found that skin provides the main initial resistance against sharp objects but once a certain force has been exerted, the sharp instrument will penetrate the skin without further resistance, into the flesh. In most instances, further resistance is provided by the knife fracturing the ribs or bone. Research at the Forensic Department, University of Glasgow, has shown that in most stabbing incidents on upper abdominal areas, the ribs have actually fractured. However, very little research has been carried out to quantify the force to fracture or penetrate the ribs or bone in such a manner as to admit constitutive modelling.

Bone is a complex material and initially it is prudent to study model materials with more consistent engineering properties. Bone is also fairly brittle but not entirely so and it is better modelled by a toughened engineering ceramic than by a monolithic ceramic. However the latter is more readily available. The work will then begin on two concurrent threads. The first will be an experimental study of the impact response of monolithic engineering ceramics e.g domestic tiles, alumina and machinable ceramic. Apart from contributing towards the development of a test methodology, the results of this thread are required in their own right to answer questions raised by police officers, end-users on the knife-resistance of ceramic body armour. At the same time, a start will be made on the computational modelling of damage in a toughened ceramic in conjunction with continuum damage mechanics.

These simulations will be modelled under quasi-static loading, since experimental data for such a material (ceramic composite T-section and bar) is already available (Gibson(1995)).

Eventually, these two threads will be combined in an attempt to model the results of impact tests on the toughened ceramic which is bone. Fig 2 shows how the present and future work will contribute to the final synthesis of a constitutive model for bone.

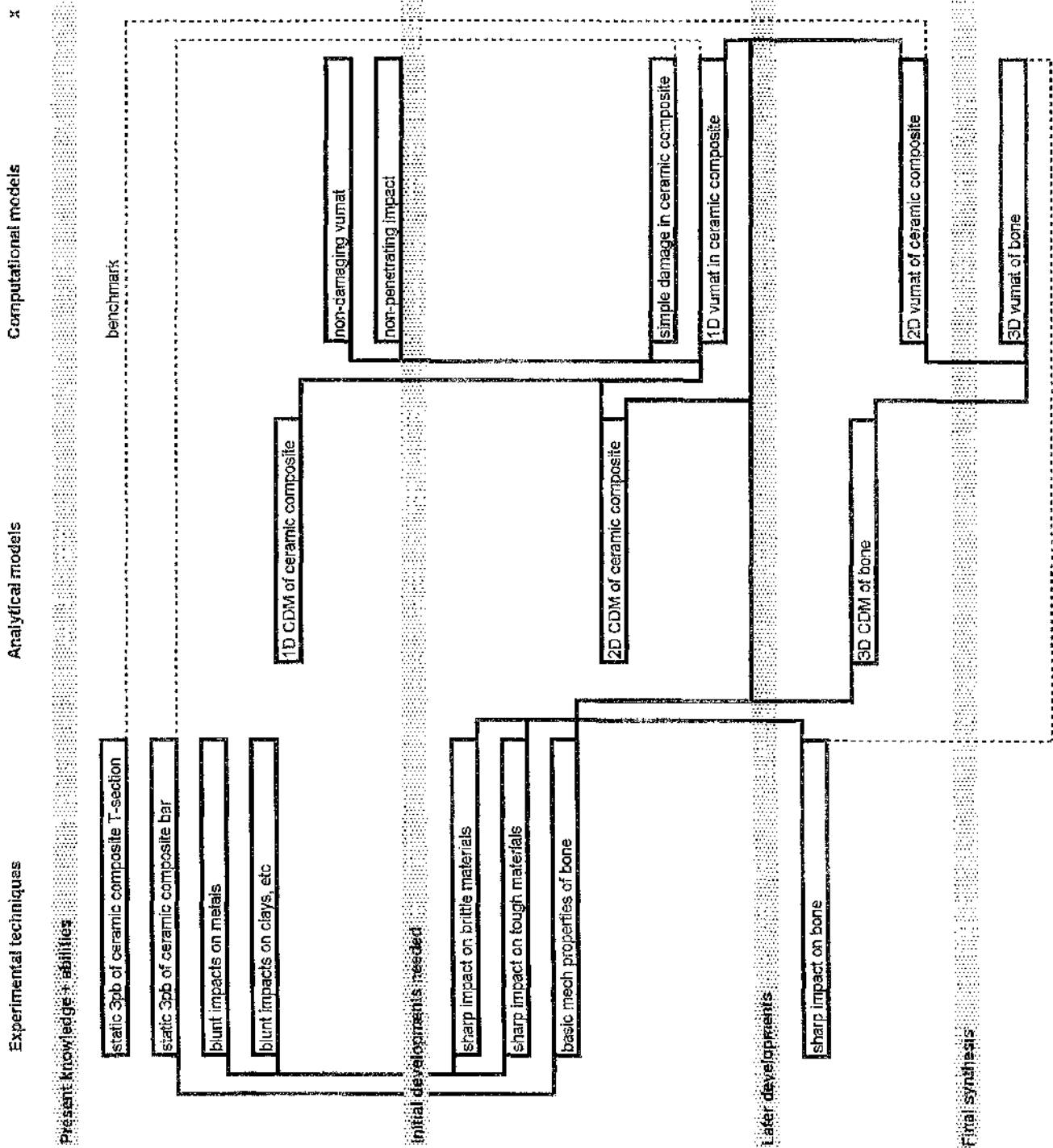


Fig 2 Project plan

1.3 Brief Introduction to Continuum Damage Mechanics

The term “damage” refers to the decrease in the desirable property of a material subjected to unfavourable mechanical or environment conditions. Some examples of “damage” of materials are:

- Creep damage
- brittle cracking, e.g in concrete
- fatigue damage
- environment degradation

In fracture mechanics we focus attention on a single well-defined crack and assume that almost all of the available strain energy, within the volume of interest, is used to drive forward this crack in a direction essentially normal to the loading direction. If any of these features is absent, fracture mechanics is inapplicable. So, while it is well suited to model the final stages of fracture, fracture mechanics is not suited to model the initial evolution of damage in materials where there is a sufficient amount of microcracking to provide a significant additional energy sink within the volume of interest. In principle, each micro-defect could be modelled individually and the results integrated to give a macroscopic constitutive model of the damaged material. However the large number of defects in real materials and their complex interaction make this an impractical proposition.

To introduce the concepts of damage mechanics, reference may be made to the experimental σ - ϵ curve for a uniaxial but notched or already necked tensile specimen of ductile steel subjected to several loading/ unloading cycles, shown in Figure 1.3(a).

Normally E is considered to be unaffected by plastic deformation and so all the elastic loading/unloading lines should be parallel.

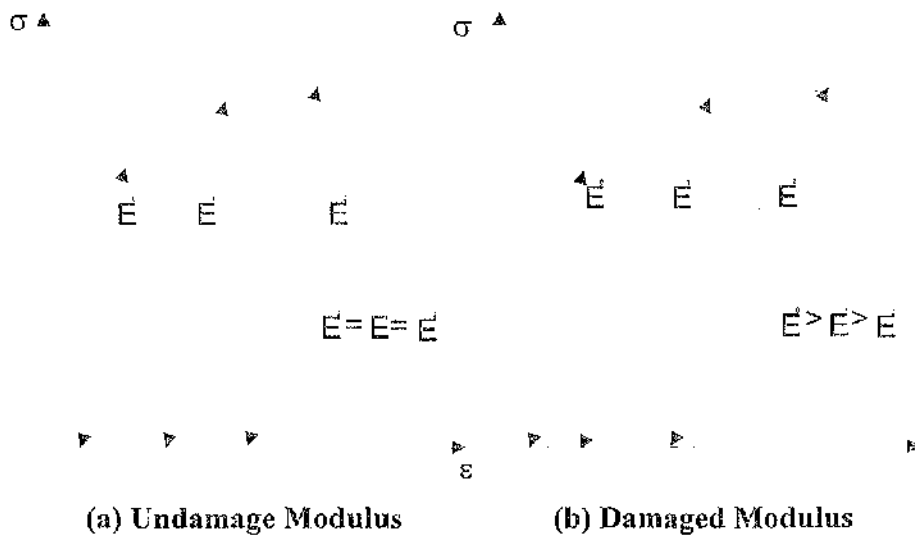


Fig 1.3

However closer examination of the plot shows (Fig 1.3(b)) that in fact the elastic modulus decreases slightly as plastic strain, and hence damage, accumulates. This can be explained by noting that within the notch or neck in the specimen there exists a triaxial stress state in which the voids grow normal as well as parallel to the loading direction. This normal growth reduces the proportion of the cross-section occupied by load-bearing matrix and so reduces the elastic modulus of the increasingly porous material.

Brittle materials such as ceramics also show a reduction in E on loading/unloading but here the mechanism is microcracking normal to the tensile axis, which occurs even under purely uniaxial loading. In such purely elastic materials the cracks also close completely on unloading, returning the material to (0,0) on the σ - ϵ curve.

Since stress depends on the area but not the shape of the material cross-section, the reduction in stiffness should depend on the total area occupied by defects but not on their individual geometries.

We can thus introduce a damage measure D ., defined as:

$$D = (A - A_x)/A$$

$$= 1 - A_x/A$$

where A_x is the area of load-bearing **matrix** and A is the aggregate area of matrix plus defects. We can distinguish between the matrix stress:

$$\sigma_x = F/A_x$$

and the aggregate stress:

$$\sigma = F/A.$$

For any particular specimen:

$$F = \sigma * A = \sigma_x * A_x$$

So:

$$\sigma = \sigma_x * A_x/A$$

$$= \sigma_x * (1 - D)$$

where $(1-D)$ is sometimes called the **integrity** of the material.

It should be noted that, σ_x and σ are both averages and the averaging process smears out the damage to the whole cross-section, modelling the heterogeneous porous aggregate as a homogeneous damaged continuum. Unlike fracture mechanics therefore, **Continuum Damage Mechanics (CDM)** cannot account for the shape of individual defects and does not even recognise their individuality. A full understanding of failure thus requires input from both approaches.

We now assume that the strain produced in a damaged aggregate subject to a uniaxial stress σ is the same as that produced in an undamaged aggregate (ie pure matrix) subject to $\sigma_x = \sigma/(1-D)$. Essentially this means that no distinction is made between the aggregate and matrix strains and the only effect of macroscopic damage is to vary the ratio σ/σ_x . Hence:

$$\varepsilon = \sigma/E = \sigma_x/E_x$$

where E and E_x are the aggregate and matrix elastic moduli respectively. Hence:

$$\sigma_x * E = \sigma * E_x$$

$$\Rightarrow \sigma_x * E = \sigma_x * (1 - D) * E_x$$

$$\Rightarrow E = (1 - D) * E_x.$$

There is no micromechanism to cause E_x to change so it is assumed to remain constant throughout the deformation. E must therefore reduce as damage accumulates, in agreement with the experiments and as shown in Figure 1.3(b).

Rearranging the last expression gives:

$$D = 1 - E/E_x$$

and D can conveniently be determined as a function of strain. If the material sustains inelastic strain, this requires us to unload periodically during the test to get the current E . Since the aggregate is initially undamaged, the matrix modulus E_x is equal to the initial modulus 0E of the aggregate.

Since E reduces with increasing D , the constitutive response for a damaging material must be nonlinear even if the aggregate is perfectly elastic, returning to $(\sigma, \epsilon) = (0,0)$ on unloading, and the matrix is linear elastic. Indeed, in this case there is no need to unload periodically during the test to get the current E . For such materials this is just the secant modulus $ES = \sigma/\epsilon$.

EXPERIMENTS ON MODEL MATERIALS

2.1. Model Materials

Structurally, human bone is a complex material with mechanical properties which depend on the original location of the specimen on the body, the age of the specimen and even the preparation of the specimen. It is therefore prudent to perform some preliminary experiments on much simpler "model" materials and to correlate their experimental behaviour under impact with computational analyses. This not only reduces the learning time for the computational modelling but also cuts the cost of preparation of bone specimens.

A number of model materials were proposed, including domestic tile, through commercial aluminium nitride (a machinable ceramic) and alumina, to a specially manufactured DuPont Lanxide. These are all brittle or toughened ceramics with a wide range of properties and costs, the last being a fibre-toughened ceramic composite of SiC fibres in an alumina matrix.

The simplest mechanical test is the uniaxial tensile test but problems associated with premature cracking of the brittle materials at the grips mean that three point bending tests are more appropriate. Such tests were carried out on domestic tiles but the results showed insignificant strength in the material. Gibson and Thomson (1995) carried out similar tests on DuPont Lanxide and their results are presented in Chapter 4, together with manufacturers' data for the commercial monolithic ceramics.

The ultimate aim of the current work is to computationally and experimentally model the impact of a sharp object on a near-brittle material and so impact tests were also carried out on the model materials. For the impact tests, coupons of about 70 x 70 x 3 mm were used, except for the Lanxide, which was not available in such a size.

2.2 The Impact Rig

The Home Office Police Scientific Development Branch (PSDB) has carried out stabbing experiments to assess the protection offered by commercial stab-resistance body-armour (Parker ,1993). In these tests, a gas-gun was used to launch a knife-carrying missile horizontally onto the target from a pre-determined distance. The pressure of the gas could be adjusted via a compressor to give the desired velocity of up to 14 m/s and hence to control the kinetic energy. The target had Roma Plastilina modelling clay as a backing for the body armour while a photocell sensor was used to measure the velocity of the knife leaving the cannon muzzle.

In the current work, measurements taken from video footage of simulated knife attacks showed the velocity of the blade at impact to be of the order of 3 m/s. This is low in comparison with the 8 m/s, occasionally 14 m/s, found by Parker and specified for the gas-gun design. However this difference may simply reflect particular styles of attack. Those recorded here were close-quarter events involving an essentially stationary victim and assailant. In such cases, the simulation may well be done by a simple gravity-driven drop-tower apparatus. It also remains controversial as to whether energy, momentum or force is the controlling parameter in ballistic penetration (Hetherington , 1995) and indeed, the present author believes that many knife incidents involve relatively low velocities with high follow-through forces, i.e. low energy but high momentum, and are not well simulated by the gas-gun apparatus specified by the UK Home Office. This conclusion has also been reached by the US Department of Justice (1993).

A schematic diagram of the drop-tower is shown in Fig.2.1. In this, stabbing impact is simulated when the crosshead, to which a knife blade may be attached, is released from a preset height and allowed to fall under gravity. The total mass of the crosshead assembly was 4.4kg.

The release latch could be affixed at any level and so the impact could be observed under a range of velocities and kinetic energies. The height of the drop tower is 3.26m with a width of 0.68m. The maximum drop height of crosshead is 2.75m, and so the maximum attainable velocity under full gravitational acceleration is 6.2m/s. In practice, while sliding friction between the railings and the crosshead was reduced by linear bearings, this speed is unlikely to be reached.

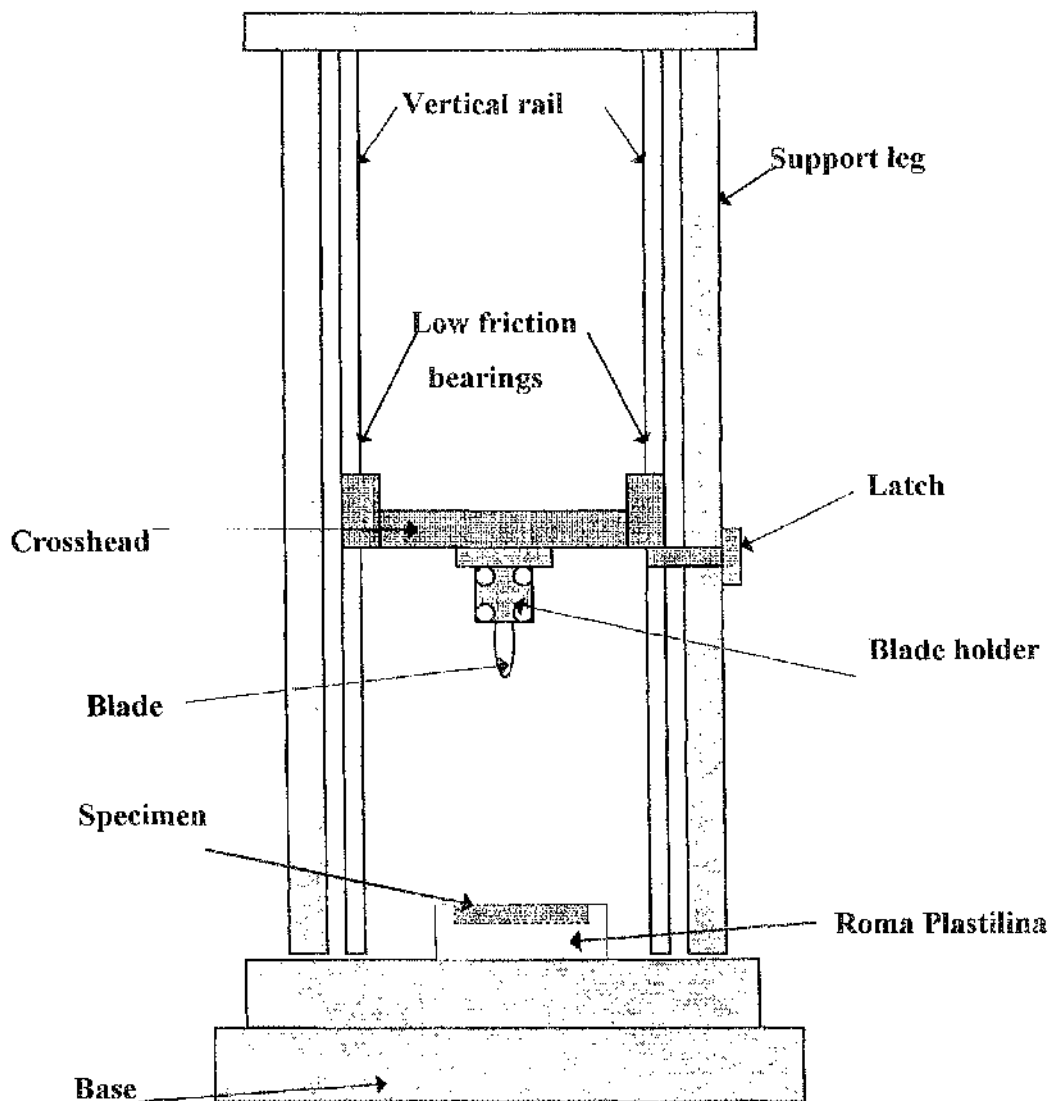


Fig.2.1 Drop Tower

Various forms of instrumentation were tried to measure the velocity of the crosshead, from a simple stop watch, through accelerometers, optical switches and a Doppler transducer. None of these proved entirely satisfactory and the final choice was for video recording. The initial experiments used standard domestic video with a refresh rate of 25 frames/s. Later, a high video speed system capable of 600 frames/s was used for more accurate measurement. This allows direct calculation of the final crosshead velocity without the need to make assumptions about the acceleration profile.

2.3. Blade Profiles

The profile of the knife blade does influence the force needed to cause penetration damage to a material (Knight, 1975) but the commercially manufactured knife blades described by Parker are rather too complicated to admit simple finite element modelling. A number of simplified model blades were therefore devised by Ankersen (1996) as shown in Figure 2.2. These were ground from high-quality steel, readily available as broken sections of power-hacksaw blades. Such blades typically break in service at lengths of about 20 cm with no damage to the microstructure of the remaining metal. The profiles were specifically designed to highlight any effect of the sharpness of the blade tip and edge and to admit computational prediction of tip stresses.

In the current experiments, the type 3B knife blade, with a pointed tip and sharpened edges, was chosen to represent the worst-case attack.

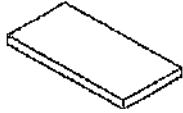





No	Description	Figure
1A	Square-ended blade with blunt edge	
1B	Square-ended blade with sharp edge	
2A	Blunt-tipped blade with blunt edges	
2B	Blunt-tipped blade with sharp edges	
3A	Pointed blade with blunt edges	
3B	Pointed blade with sharp edges	

Figure 2.2 The model knife profile

2.4 The Velocities And Kinetic Energy Of The Crosshead Assembly At Impact

2.4.1 Domestic Video Recording Technique

A ceramic specimen of whatever type was surface mounted on a block of Roma Plastilina. This acts as a backing to support and retain any fragments of the target material. The crosshead assembly was raised to a known height and rested on the movable latch which incorporates a quick release lever.

The fall of the blade from the stationary position until contact with the specimen was recorded by the domestic video camera at the industry standard rate of 25 frames per second. Playback of the video tape in slow motion allowed the number of frames to be counted and so the travel time T simply calculated as:

$$T = N / 25(\text{seconds}) \text{ -----Equation(1)}$$

The results of three separate trials at each height was averaged to give some statistical confidence in the timings. These results are summarised in Table 2.0

Height (m)	Frame 1	Frame 2	Frame 3	Average Frames	Time (s)	Acceleration (m/s ²)
0.05	3	2	3	3	0.12	6.944
0.10	4	3	4	4	0.16	7.813
0.20	6	6	6	6	0.24	6.944
0.40	8	9	8	8	0.32	7.813
0.60	10	10	10	10	0.40	7.500
0.80	12	11	12	12	0.48	6.944
1.00	13	14	14	14	0.56	6.378

Table 2.0 Calculating the time taken and acceleration

In compiling Table 2.0, it was assumed that acceleration of the crosshead was constant within any single trial. From Newton's equation:

$$s = ut + \frac{1}{2} at^2 \text{ -----Equation (2)}$$

where s = initial height, u = initial velocity ($= 0$), and t = time. The acceleration a for the complete set of tests can then be calculated. This was found to be almost constant at about 7m/s^2 , significantly less than the 9.81 m/s^2 expected under free fall. The final velocity v from any initial height is:

$$v^2 = u^2 + 2as \text{ -----Equation (3)}$$

Knowing the final velocity, we can then calculate the kinetic energy of the blade as:

$$\text{Kinetic Energy, } K.E = \frac{1}{2} mv^2 \text{ -----Equation (4)}$$

With m is 4.4 kg , for the total measured mass of the crosshead assembly, a calibration table is obtained for the drop tower (Table 2.1).

Distance (m)	Acceleration (m/s^2)	Velocity (m/s)	Kinetic Energy (J)
0.05	6.944	0.833	1.527
0.1	7.813	1.25	3.438
0.2	6.944	1.667	6.114
0.4	7.813	2.500	13.750
0.6	7.500	3.000	19.800
0.8	6.944	3.333	24.444
1.0	6.378	3.571	28.054

Table 2.1 Calibration table

2.4.1.1 Discussion

Table 2.1 only gives the tower calibration table to a drop-height of 1 m although the maximum drop height of the tower is 2.75m. This was because the specimens used for the immediately following experiments, with polymer and domestic ceramic tiles, were expected to penetrate at 1m or below. Obviously, the calibration can be extended if required.

2.4.2 High Speed Video Camera Technique

An alternative video technique leading to a more accurate measurement of the velocities of the crosshead assembly is a high speed camera. The KODAK MotionCorder Analyzer Model 1000 system was purchased in the later stages of the current work. The MotionCorder camera has a capability of recording up to 600 frames per second and utilises an electronic shutter to minimise motion blur. The Analyzer system can store up to 1,905 full frames and the playback speed can varied from single frames up to 240 frames per second. It also features a unique variable record and display format that can be used to increase the frame rate or extend the number of the images that can be stored in the digital memory.

The OPTIMAS Image Analysis and OPTIMAS-MA Motion Analysis software, incorporated with a video- enhanced (4 MB Video RAM graphics and 64MB RAM) computer, was also used. This has powerful image processing and measurement functions, automatic data output to ASCII files or Excel worksheets.

The MotionCorder camera comes with two lens: 12mm f1.2 and 25mm f1.4. In this experiment, the 12mm lens was used to capture the close-up images of the crosshead assembly. The short focal distance to the target results in a restricted field of view and data could be captured only just before and after the impact. A 50 watt Halogen narrow beam lamp was attached on the camera to allow a faster shutter speed to minimise blur and to admit the maximum frame speed.

The video enhanced computer and the MotionCorder camera were connected to the MotionCorder Analyzer system. Prefocusing of the camera can be done by adjusting the lens and viewing the sharpness of the image on the online computer monitor. A calibration scale is required by OPTIMAS to establishing the absolute size of objects in the image frame and so a ruler was placed vertically along the crosshead assembly before and after the impact. A prominent mark was made on the knife blade as in Fig 2.3 to act as a reference point during motion analysis. This mark can be selected on the screen in every frame, allowing the software to gauge the distance travelled between frames. Knowing the frame rate, the velocity history can be generated by the software.

As before, the drop height commences from 0.1m with an increment of 0.1m up to a maximum height of 1.0m. Again, each test was carried out with three repetitions and the velocities plotted.

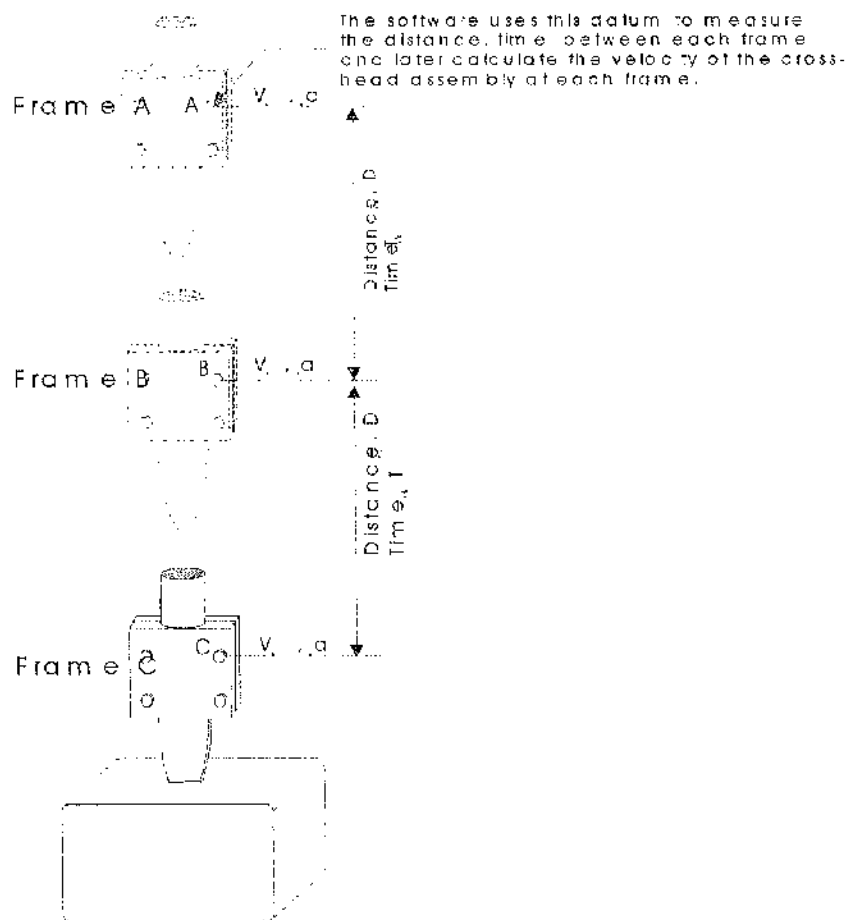


Fig 2.3 *Measuring the velocity of the crosshead assembly at each frame*

Some samples of the frames are shown in Fig 2.4.

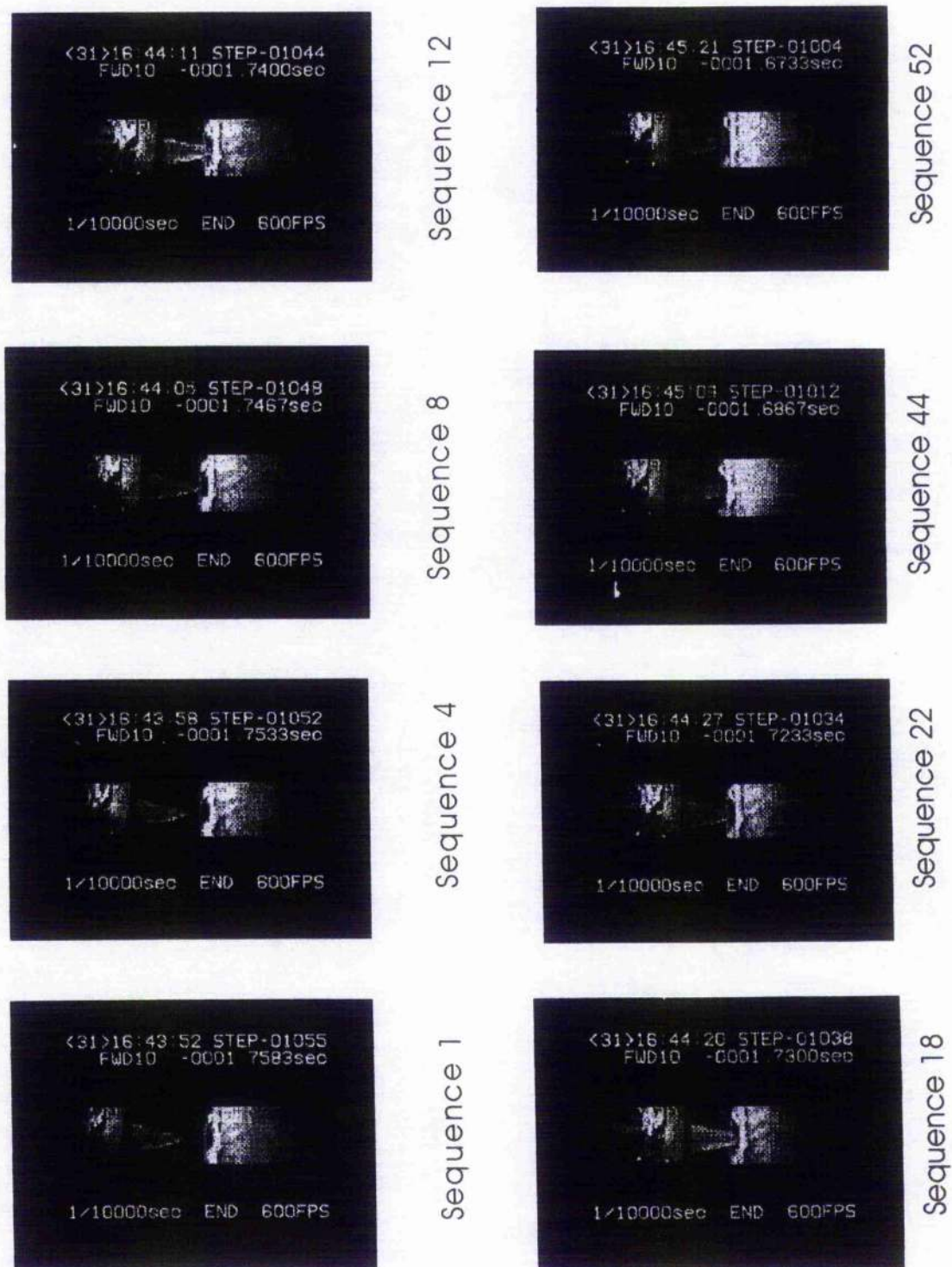


Fig 2.4 Samples of the frames

2.4.2.2 Results And Discussion:

From equation 4, with $m= 4.4\text{kg}$, the kinetic energy was calculated and tabulated as shown:

Drop Height (m)	Final Velocity (m/s)	Kinetic Energy (J)
0	0	0
0.1	1.150333	2.71
0.2	1.598	5.23
0.3	1.952667	7.82
0.4	2.240333	10.29
0.5	2.519667	13.0
0.6	2.803	16.11
0.7	3.024	18.75
0.8	3.240333	21.52
0.9	3.380667	23.42
1	3.469	24.67

Table 2.2 Results of calculated Kinetic Energy

The results obtained from the motion analysis shows an unusual increment of velocity just before and at the point of impact on the Roma Plastina. This is due to the highly sensitivity of the motion analysis software, and any slight offset while marking the reference point (white spot on the knife blade) on every frame increment causes small fluctuation of the results. This technique of achieving the results is quite tedious as time has to be spent on the setting up the apparatus, adjusting the lighting and focusing as well as marking the reference point manually in every single increment on the monitor. However, it allows more direct measurement of final velocity than the domestic video method.

Two graphs have been plotted comparing the domestic video recording and high speed camera technique (Fig 2.5(a) & (b)). The differences in value are not significant here probably due to the limited drop height as well as the light weight of the crosshead assembly, but may be important in other cases.

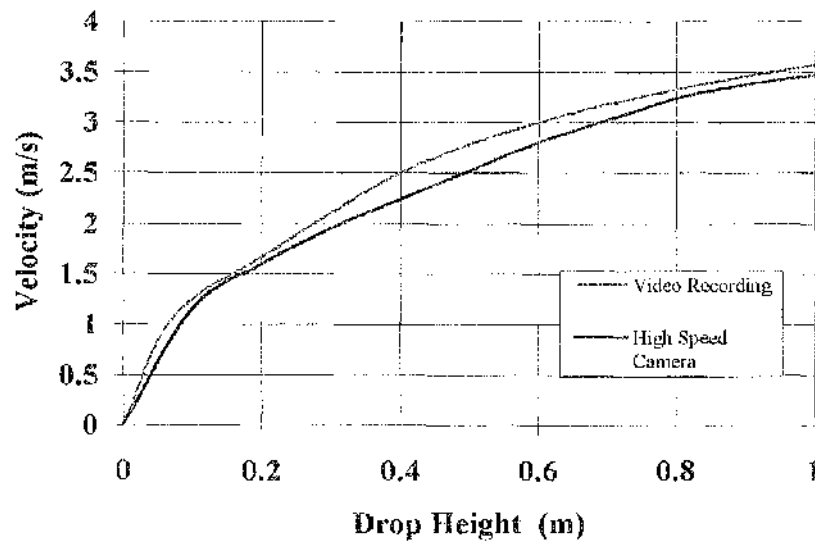


Fig 2.5 (a) Drop Height-Velocity Curves

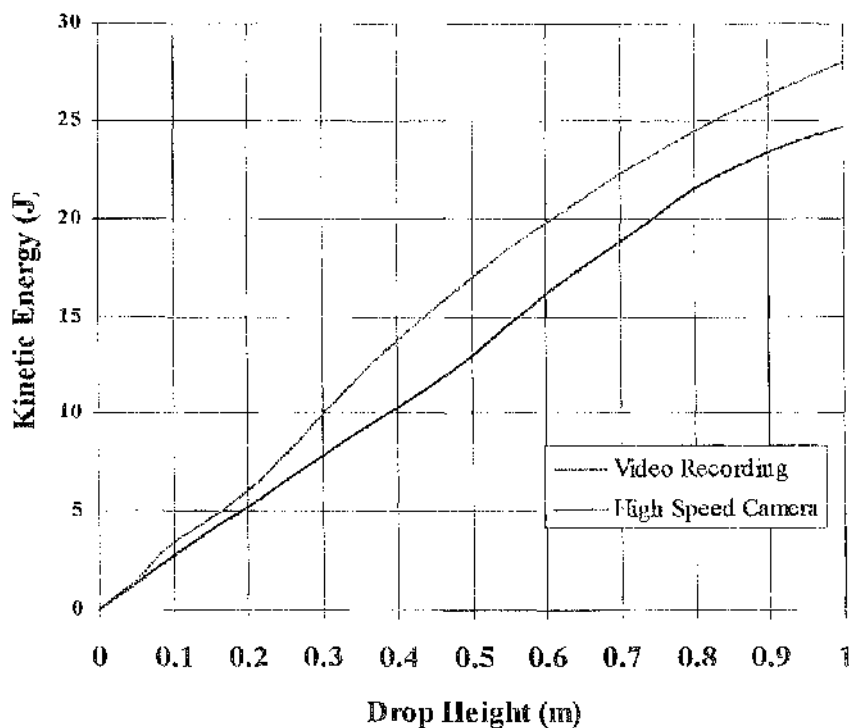


Fig 2.5(b) Drop Height-Kinetic Energy Curves

Other, the major advantages of the high speed camera over the video recording technique are:

- higher accuracy (600 frames/sec compared to the video playback technique at 25 frames/sec.)
- computerised results of the initial and final velocities
- data and image storage which can be easily recall and transfer to spreadsheets or image printout.
- can record and instantly play back video

2.5. Impact Tests

2.5.1 Test On Domestic Tiles

Domestic tile is a clay-based fired ceramic. It is very cheap, commercially available and easy to cut with a commercial tile cutter. These features make it a good candidate for a model material for human bone.

2.5.1.1 Protocol And Results

Slabs of tile 70 x 70 x 3 mm were cut with a tile cutter, taking care not to prematurely fracture what was found to be a very weak, brittle material. An initial test was carried out with the crosshead dropped from a modest height of 10 mm. The knife blade penetrated the sample. The drop height was progressively reduced but even at a height of 1mm the blade cracked the tile. Further drop tests were carried on a double thickness of tile.

These repetitions were carried out with a decrement of 0.005m for every test. Only when the drop height was 0.0065m and above, was a significant result achieved, in which the top and bottom tiles were fractured.

No. Of Tiles	Drop Height (m)	Remarks
2	0.0050	Upper piece cracks, lower piece unaffected
2	0.0055	Upper piece cracks, lower piece unaffected
2	0.0060	Upper piece cracks, lower piece unaffected
2	0.0065	Upper and lower piece cracks
2	0.0070	Upper and lower piece cracks
2	0.0075	Upper and lower piece cracks

Table 2.3 Impact tests on domestic tiles

2.5.1.2 Discussion And Conclusions

Domestic tiles are easily fractured under very modest impact loads. They may then have some use where the aim is to study the fracture patterns in brittle materials but the energy required to cause fracture is too low to admit any quantitative analysis. Domestic tile is thus unsuitable as a model material for human bone.

2.5.2 Tests on Aluminium Nitride Machinable Ceramic

Aluminium nitride (AlN) is a commercially available machinable ceramic. It is an engineering ceramic and so is considerably stronger than domestic tile but is not a high-strength material. This makes it an attractive candidate for a model for human bone since it can be machined to a shape representative of a particular anatomical feature but may still may be damaged by a knife impact at reasonable energies. It is however an expensive material and only one specimen was procured for these initial investigations.

2.5.2.1 Protocol And Results

The dimension of the specimen was 50 x 50 x 6.5 mm. An initial test was carried out with the crosshead dropped from a height of 0.005m. No crack was found on the specimen. The drop height was increased to 0.010m and a small fragment of the test piece was chipped off. Additional small fragments of the test piece were chipped off with every height increment of 0.010m until it has reached a height of 0.05m.

When the drop height was raised to 0.075m, the machinable ceramic was "hammered" into the Roma Plastilina backing. At a drop height of 0.1m, the machinable ceramic was finally fractured by the impact of the blade. The results are summarised in Table 2.4.

Test No.	Drop Height (m)	Remarks
1	0.005	No crack was found
2	0.010	A small fragment was chipped off
3	0.020	Deeper, bigger fragment was chipped off
4	0.030	Deeper, bigger fragment was chipped off
5	0.040	Deeper, bigger fragment was chipped off
6	0.050	Deeper, bigger fragment was chipped off
6	0.075	Specimen was "hammered" into the Plastilina backing
7	0.100	Specimen was fractured

Table 2.4 Impact test on machinable ceramic

From equation (1) to (4), the energy need to cause fracture can be calculated, as in Table 2.5 results were calculated and tabulated:

	Results
Time Taken	0.16 seconds
Acceleration	7.813 m/s ²
Velocity	1.25 m/s
Kinetic Energy	3.438 J

Table 2.5 Calculated result of Kinetic Energy

2.5.2.2 Discussion And Conclusions

The machinable ceramic specimen has proven a more tougher and reliable material than the domestic tiles. The kinetic energy for the blade to fracture the specimen is 3.438 J at a drop height of 0.1m. However, this result is not statically reliable since only one machinable ceramic specimen was available and, although each impact was made on a different location of the specimen, it might pre-crack before the next test was carried out. Having to change a new location for each test also changes the details of the stress field tile. This may also affect the distribution of the load on the Plastilina backing.

2.5.3 Alumina Ceramic

Alumina (Al_2O_3) is a commercially available high-strength engineering ceramic frequently used in ballistic armours. It is considerably stronger than human bone but is included in the test programme to give some indication as to whether high strength is accompanied by impact resistance to a sharp implement.

This question is of particular interest to police officers who have expressed specific concern to the author that ballistic armour may shatter and provide inadequate protection under relatively low intensity knife attack.

2.5.3.1 Protocol And Results

The dimension of the test specimen is 0.05 x 0.05 x 0.006 m. The experiment setup was similar to that of domestic tiles and machinable ceramic. The material was tested at a drop height of 0.05m to 0.80m. No cracking or chipping was found. However, at a drop height of 0.90m the alumina was fractured into three pieces. The results are summarised in Table 2.6.

Test No.	Drop Height (m)	Remarks
1.	0.05	No chipping or mark
2.	0.10	No chipping or mark
3.	0.20	No chipping or mark
4.	0.30	No chipping or mark
5.	0.40	No chipping or mark
6.	0.50	No chipping or mark
7.	0.60	Spark caused by the friction between the blade & ceramic
8.	0.70	No chipping or mark
9.	0.80	No chipping or mark
10.	0.90	Alumina fractured into 3 pieces

Table 2.6 Impact test on alumina

Again, from equation (1) to (4), the energy to cause fracture can be tabulated, as in Table 2.7.

	Results
Time Taken	0.52 seconds
Acceleration	6,657 m/s ²
Velocity	3.462m/s
Kinetic Energy	26.368 J

Table 2.7 Calculated result of Kinetic Energy

2.5.3.2 Discussion And Conclusions

Alumina ceramic was found to be the toughest among the three materials. It requires a kinetic energy of 26.368 J, at a drop height of 0.9m in order for the blade to penetrate the specimen. This took place without any sign of warning e.g chipping or cracks. As mentioned earlier, the results obtained are not statistically reliable since there was only one specimen available for each series of tests. Thus, the kinetic energy required to fracture the alumina specimen might be higher than calculated.

The results do however show the order of magnitude of the impact energies and so indicate the ranking of the materials, and hence whether any is likely to be a suitable candidate as a bone simulant. Due to the toughness of the alumina ceramic and the misalignment of the centre of specimen with respect to the blade, the material was pressed into the Plastilina backing almost on every impact test, resulting in breaking the knife blade on one occasion (Fig.2.6).

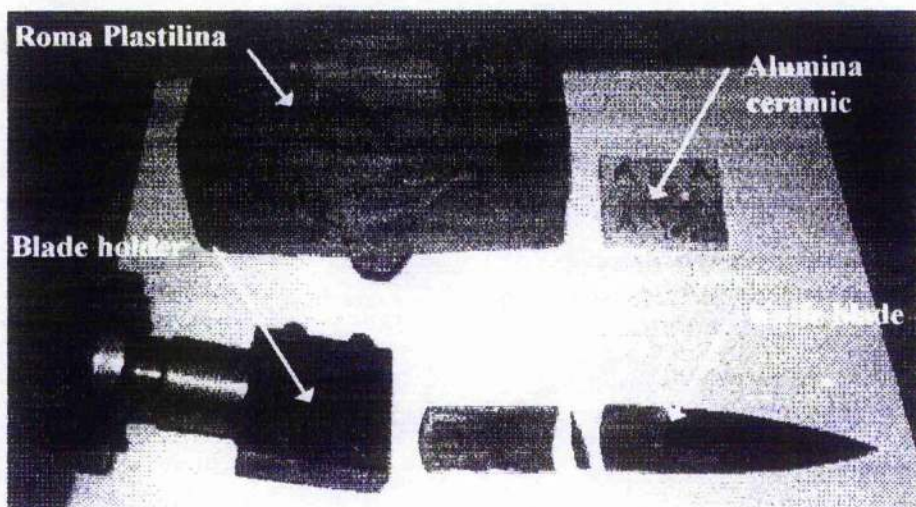


Fig 2.6 Impact test on alumina. (Note that the Plastilina has been deformed slightly due to pressing)

2.6 The Role Of Momentum Vs KE In Impact Resistance

The previous tests have emphasised the role of kinetic energy as a measure of the impact resistance of target materials. This view is implicit in the PSDB standard for stab-resistant body armour, which is based upon the US NIJ work and requires that the armour resist a knife attack of 42 J. Hetherington (1995) has expressed doubts over the use of KE as a one-parameter measure of the penetration resistant of ballistic armours and has suggested that momentum absorption, P , given by:

$$P = m \times v \text{ -----Equation (5)}$$

is better correlated with experimental results. Ankersen et al (1996) have expressed similar doubts in the case of stab-resistance and questioned whether KE, momentum, force or indeed any single parameter can adequately characterise the severity of a stabbing attack.

It might also be mentioned in passing that even the alumina fails at an energy considerably below the PSDB body armour standard. This is not directly relevant here but indicates a need for further study.

Drop tower experiments are a good means of investigating the KE v P question for the crosshead accelerates under gravity at a rate which is independent of its mass. By attaching additional masses to the crosshead it is then possible to conduct experiments in which the KE is held constant but the momentum is varied in a systematic manner and, conversely, experiments in which the momentum is held constant but the KE is systematically varied.

Now the ceramic model materials used so far either show minimal damage under the impact or they fail completely. They are therefore unsuitable for tests in which a range of damage, such as is expected with impacts on real bones, is required. Further tests were therefore carried out on polymer (PVC) coupons. Being ductile, these represent the other extreme to the ceramics. The two extremes then bracket the behaviour of real bone.

2.6.1. Protocol And Results

The test protocol was similar to before, but with a type 3A knife blade (sharp tip, blunt edges) dropped onto the polymeric test specimens from a range of different heights. A slightly different knife mount was used, reducing the mass of the crosshead assembly to 4.1 kg. Additional laboratory-type masses could be fixed to this basic assembly to give a range of impact masses.

For this particular choice of knife profile, the impact produces a rectangular slot whose length W depends on the depth of penetration D and hence the severity of the impact. For the current purposes, a simple ranking of the extent of damage to the target is sufficient. This was measured as the length of the slot (Fig. 2.7).

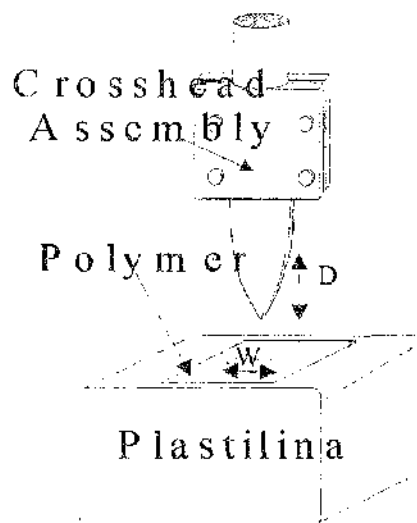


Fig.2.7 Measuring the damage

The basic 4.1 kg crosshead was dropped from a range of heights from 0.05 m to 1 m and the damage was measured and shown in Table 2.8.

Test No.	Time (s)	Velocity (m/s)	Height (m)	Kinetic Energy (J)	Momentum P (Ns)	Damage D (m)
1	0.12	0.833	0.05	1.422	3.415	0.001
2	0.16	1.250	0.10	3.203	5.125	0.002
3	0.24	1.667	0.20	5.697	6.835	0.003
4	0.32	2.500	0.40	12.813	10.250	0.012
5	0.40	3.000	0.60	18.450	12.300	0.018
6	0.48	3.333	0.80	22.773	13.665	0.026
7	0.56	3.571	1.00	26.142	14.641	0.030

Table 2.8 Measurement of damage

From Table 2.8, a time-velocity graph was plotted as in Fig 2.7.

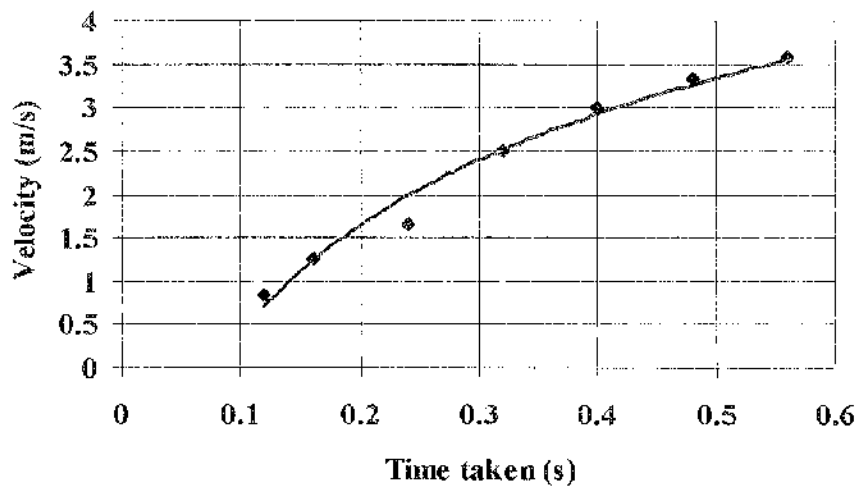


Fig 2.8 Time-velocity graph

Tests 1 to 3 show insignificant damage arising from the small values of kinetic energy and momentum. Thus, results from tests 4 to 7 have been used as a basis for calculation of the additional masses and the drop height needed to admit tests at constant momentum but variable KE and, vice versa, at constant kinetic energy but variable momentum. A sample calculation is shown below for the constant momentum case, with $P=10.25 \text{ Ns}$:

Constant momentum with variable KE

For constant momentum, $P_1 (4.1\text{kg}) = P_2 (5.1\text{kg}) = P_3 (6.1\text{kg})$ etc

$$m_1 \times v_1 (4.1\text{kg}) = m_2 \times v_2 (5.1\text{kg}) = 10.25\text{Ns}$$

From table 2.7, $v_1 = 2.5\text{m/s}$, $m_1 = 4.1\text{kg}$ and $m_2 = 5.1\text{kg}$, $v_2 = 2.01\text{m/s}$

The corresponding *Kinetic Energy* is:

$$KE_2(5.1kg) = \frac{1}{2} \times m \times v^2$$

$$= 10.3 J$$

From Fig 2.8 , time taken for a velocity of 2.01m/s is 0.269s

and if Acceleration, $a_2 = 7.47\text{m/s}^2$

Then the drop height = 0.27 m

Results from the constant momentum tests were tabulated in Table 2.9(a) to (d).

Constant Momentum, $P = 10.25\text{Ns}$

Test No.	Mass	Velocity	Height	Kinetic Energy	Damage
	m, (kg)	v (m/s)	H (m)	KE (J)	D (m)
1	4.1	2.500	0.400	12.813	0.012
2	5.1	2.010	0.270	10.300	0.010
3	6.1	1.680	0.200	8.611	0.006
4	7.1	1.444	0.149	7.402	0.007
5	8.1	1.266	0.103	6.485	0.006
6	9.1	1.126	0.086	5.773	0.005

Table 2.9(a)

Constant Momentum, $P = 12.3\text{Ns}$

Test No.	Mass	Velocity	Height	Kinetic Energy	Damage
	$m, (\text{kg})$	$v (\text{m/s})$	$H (\text{m})$	$KE (\text{J})$	$D (\text{m})$
1	4.1	3.000	0.600	18.450	0.018
2	5.1	2.412	0.383	14.832	0.015
3	6.1	2.016	0.275	12.400	0.011
4	7.1	1.732	0.216	10.649	0.011
5	8.1	1.519	0.171	9.339	0.010
6	9.1	1.352	0.119	8.313	0.009

Table 2.9(b)

Constant Momentum, $P = 13.665\text{Ns}$

Test	Mass	Velocity	Height	Kinetic Energy	Damage
No.	$m, (\text{kg})$	$v (\text{m/s})$	$H (\text{m})$	$KE (\text{J})$	$D (\text{m})$
1	4.1	3.333	0.800	22.773	0.026
2	5.1	2.679	0.481	18.308	0.022
3	6.1	2.240	0.330	15.306	0.019
4	7.1	1.925	0.252	13.155	0.016
5	8.1	1.687	0.208	11.527	0.014
6	9.1	1.502	0.164	10.261	0.012

Table 2.9(c)

Constant Momentum, $P = 14.641\text{Ns}$

Test	Mass	Velocity	Height	Kinetic Energy	Damage
No.	m, (kg)	v (m/s)	H (m)	KE (J)	D (m)
1	4.1	3.571	1.000	26.142	0.030
2	5.1	2.871	0.557	21.016	0.026
3	6.1	2.400	0.369	17.568	0.022
4	7.1	2.062	0.271	15.094	0.020
5	8.1	1.808	0.233	13.232	0.017
6	9.1	1.609	0.181	11.778	0.015

Table 2.9(d)

From Table 2.9(a) to (d), a graph of Kinetic Energy against Damage can be plotted as in Fig 2.9.

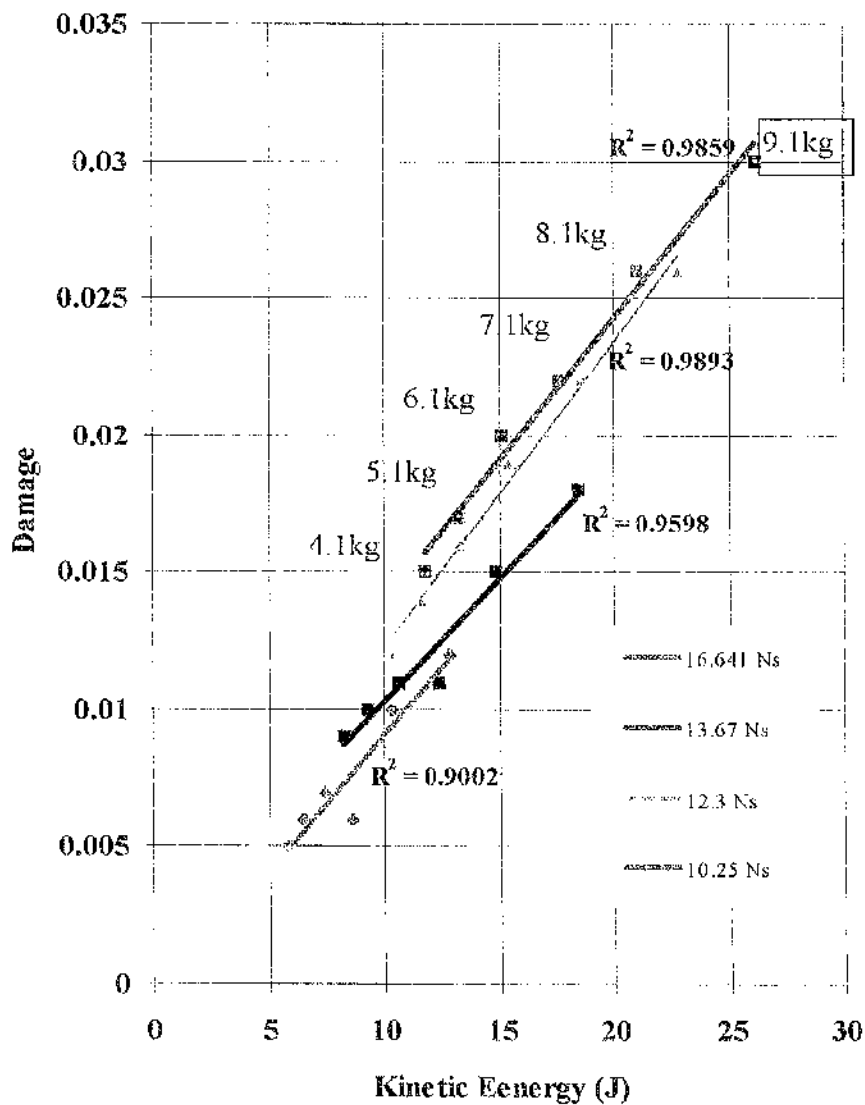


Fig 2.9 Kinetic Energy-Damage graph. (where R^2 is the linear correlation)

Constant K.E with variable momentum

A sample calculation is shown below for the constant kinetic energy case, with KE = 12.813J:

For constant kinetic energy, KE_1 (4.1kg) = KE_2 (5.1kg) = KE_3 (6.1kg) etc

$$m_1 \times v_1^2 = m_2 \times v_2^2 = 12.813 \text{ J}$$

Since $m_1=4.1 \text{ kg}$, $v_1=2.5\text{m/s}$ (table 2.7) and $m_2 = 5.1\text{kg}$, $v_2 = 2.242\text{m/s}$

The corresponding *Momentum* is:

$$\begin{aligned} P_2 &= m_2 \times v_2 \\ &= 11.434 \text{ Ns} \end{aligned}$$

From Fig 2.8, time taken for a velocity of 2.242m/s is 0.296s.

$$\text{Acceleration, } a_2 = 7.5\text{m/s}^2$$

$$\text{Then the drop height } H_2 = 0.33\text{m}$$

Results based on the constant kinetic energy tests were tabulated in Table 2.10 (a) to (d). This also shows the damage measured after each test.

Constant Kinetic Energy, KE = 12.813 J

Test No.	Mass	Velocity	Height	Momentum	Damage
	m , (kg)	v (m/s)	H (m)	P (Ns)	D (m)
1	4.1	2.500	0.400	10.250	0.012
2	5.1	2.242	0.332	11.432	0.012
3	6.1	2.050	0.281	12.502	0.012
4	7.1	1.900	0.254	13.490	0.012
5	8.1	1.779	0.225	14.407	0.014
6	9.1	1.678	0.207	15.270	0.014

Table 2.10(a)

Constant Kinetic Energy, $KE = 18.45 \text{ J}$

Test No.	Mass	Velocity	Height	Momentum	Damage
	m, (kg)	v (m/s)	H (m)	P (Ns)	D (m)
1	4.1	3.000	0.600	12.300	0.018
2	5.1	2.690	0.495	13.718	0.021
3	6.1	2.460	0.386	15.003	0.021
4	7.1	2.280	0.340	16.188	0.021
5	8.1	2.134	0.309	17.288	0.021
6	9.1	2.014	0.271	18.325	0.025

Table 2.10(b)

Constant Kinetic Energy, $KE = 22.773 \text{ J}$

Test No.	Mass	Velocity	Height	Momentum	Damage
	m, (kg)	v (m/s)	H (m)	P (Ns)	D (m)
1	4.1	3.333	0.800	13.665	0.026
2	5.1	3.202	0.586	15.241	0.026
3	6.1	2.928	0.475	16.668	0.026
4	7.1	2.714	0.409	17.984	0.026
5	8.1	2.5411	0.377	19.208	0.026
6	9.1	2.397	0.329	20.359	0.029

Table 2.10(c)

Constant Kinetic Energy, $KE = 26.142 \text{ J}$

Test No.	Mass	Velocity	Height	Momentum	Damage
	m, (kg)	v (m/s)	H (m)	P (Ns)	D (m)
1	4.1	3.571	1.000	14.641	0.030
2	5.1	3.202	0.729	16.329	0.031
3	6.1	2.928	0.561	17.859	0.030
4	7.1	2.714	0.469	19.269	0.030
5	8.1	2.541	0.410	20.579	0.030
6	9.1	2.397	0.367	21.812	0.033

Table 2.10(d)

From the results of Table 2.10(a) to (d), a Damage - Momentum graph can be plotted, as in Fig 2.10.

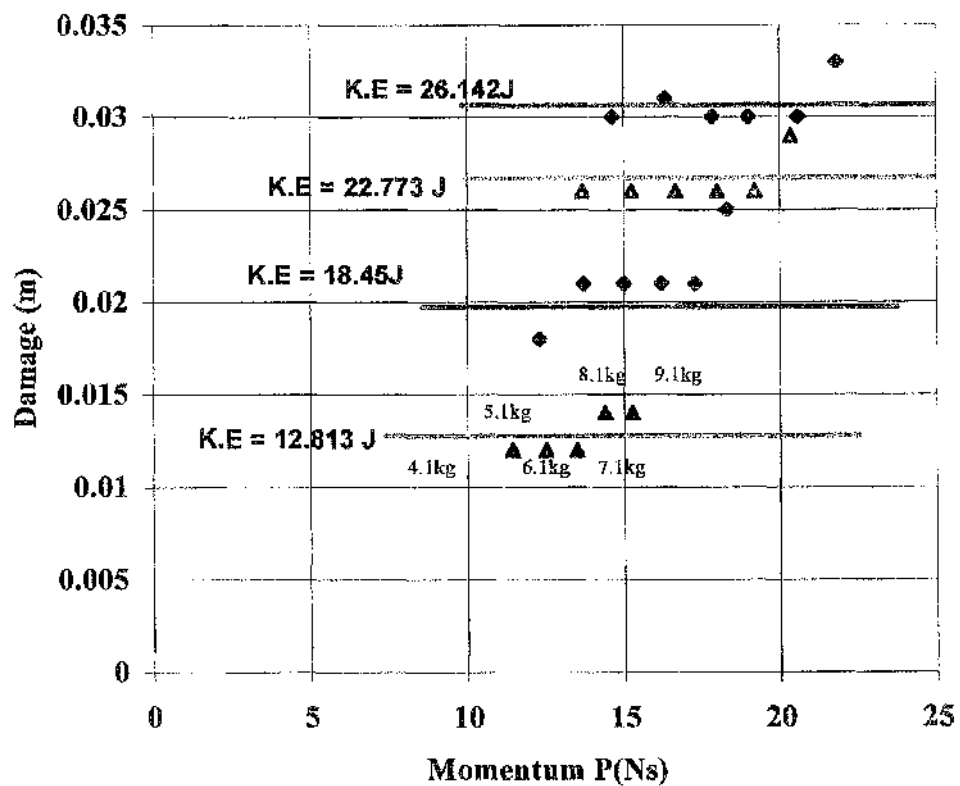


Fig 2.10 Momentum-Damage Curve

2.6.2 Discussion and Conclusions

While the simple damage measure used in this test does not admit any meaningful functional link to the kinetic energy, the results clearly show that damage increases with impact energy. This is not surprising. What is surprising is that there seems to be a tendency, admittedly slight, for the damage to increase with momentum even when the impact energy is constant. There is no obvious physical reason why this should be so and it may simply be an error in the calibration of the drop-tower. Clearly, further work is needed in this area but lack of time prevented this line of investigation to be pursued by the current author.

In particular, this work should involve higher impact energies than were used here, particularly to approach the 42 J specified by the PSDB. There is limited scope for increasing the impact energy and momentum by adding to the mass of the crosshead assembly but increased velocity could be readily achieved by power assisting the crosshead using shock-cord. At such higher velocities, it would be advisable and perhaps necessary to use high-speed video for the motion analysis.

In retrospect, it was realised that there is no need to perform the tests with either the energy held constant or with the momentum held constant. The only requirement is for data points to generate the surface in the 3-D plot (damage v KE v momentum) shown in Figure 2.11. This gives the experimenter considerably more freedom to select the test parameters.

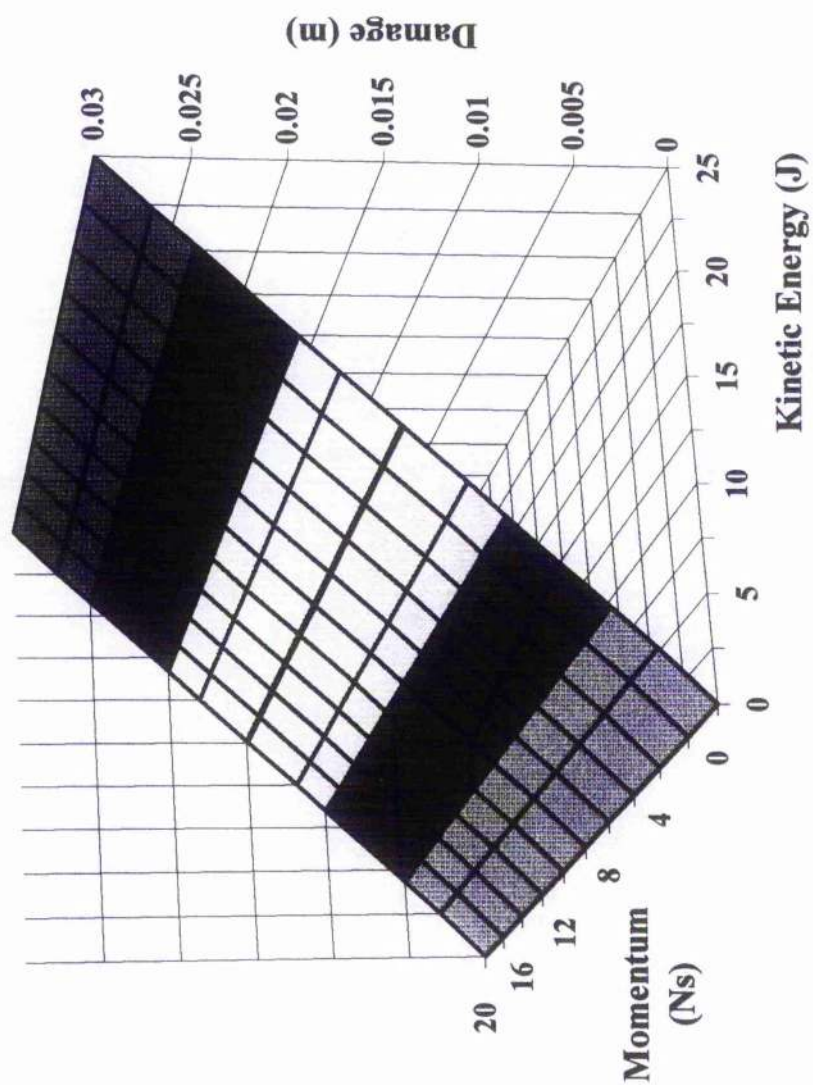


Fig 2.11 3-D plot (damage v KE v momentum)

DAMAGE PROPAGATION IN A TOUGHENED CERAMIC

3.1. Introduction

Human bone is not completely brittle but retains a degree of toughness which depends on, for example, the age of the individual. To develop a computational model which admits this toughness, it is necessary to obtain experimental data for a suitable model material. Data on damage propagation in a toughened ceramic has been published by McCafferty and Hancock (1994) and by Gibson and Thomson (1995). The experiments conducted by Gibson are of particular use here.

Gibson's aim was to develop a design methodology for ceramics and ceramic composites to be used in severe thermomechanical environments such as exist in aero-engines, etc. As part of this study he tested specimens containing geometric features typical of real structural components. These included beams (to assess the damage from point loading and determine basic properties such as elastic modulus), T-sections (for investigating of damage such as mode-1 tensile delamination) and wedge-sections (for investigating of damage such as mode-2 shear delamination) etc made from a variety of "real" and model materials manufactured both in-house and by commercial companies such as DuPont Lanxide Corporation (DLC) and Atlantic Research Corporation (Amercom).

Here, we are particularly interested in the results of the DuPont Lanxide bend bar (or beam) and T-section. This is because the geometrical features of these materials enable a simpler computational model of the damage propagation. Also, the DLC materials exhibit better strength and stiffness compared with the Amercon composites.

3.2 DuPont Lanxide Corporation Composite

3.2.1 Composite Manufacture

DuPont Lanxide composite was developed under the joint venture of Lanxide Corporation and DuPont. The ceramic composite was manufactured using a new process called DIMOX, an acronym for Direct Metal Oxidation Process.

The reinforcing fibres from DuPont Lanxide consists of 500 fibre tows of Nicalon (SiC) fibres woven into 8 Harness Satin Weave (8 HSW) and 12 HSW cloth. In an 8HSW, one warp yarn runs over seven and under one fill yarn as shown in Fig 3.1. Although Satin weaves are much more complicated than a plain weave in which one warp yarn runs over and under one fill yarn, it offers more flexibility and the material can conform better to complex and compound contours.

The 12HSW cloth has a higher fabric count which increases the composite strength. The fibres were plied and layed up to form multiple layers with a 0/90 degree orientation and the weave then infiltrated with alumina (Fig 3.2).

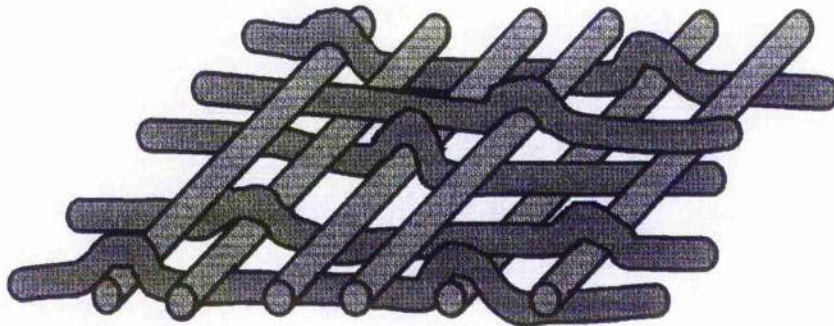


Fig 3.1 An example of a Harness Satin Weave pattern

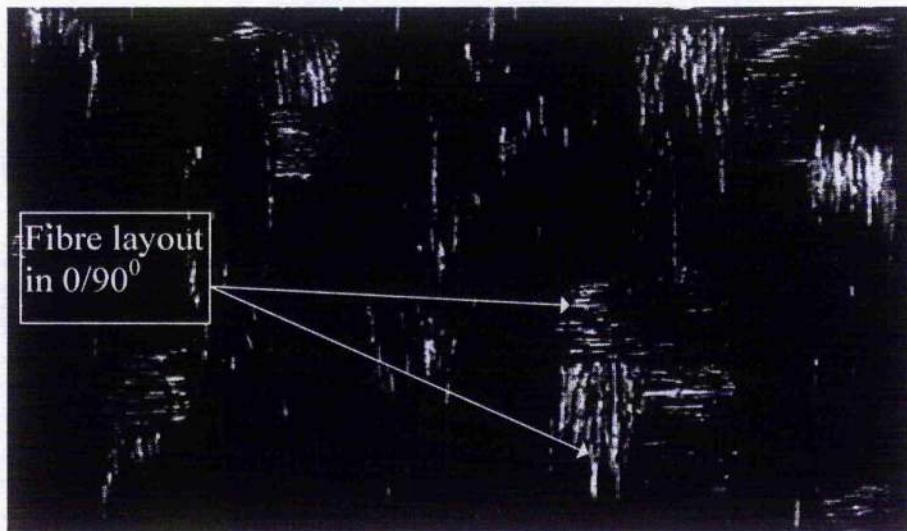


Fig 3.2 Fibre layout of Dupont Lanxide Magnification x 15

The bend bars were produced in a $0/90^0$ orientation, beginning with an 8HSW ply, followed by 6 plies of 12 HSW, and finally followed by a 8HSW in the alternate sequence of orientation. The T-section is fabricated by layout 4 plies around a round-cornered mandrel, followed by a 4-ply layout of flat plies and finally, followed by another 4 plies in the shape of a C, applied on two ends. The central region of the T-section may not be filled with the repositioned fibres during the forming process and hence, require the laying in of a 1-D tow to fill the gap.

3.2.2 Three-Point Bend On DuPont Lanxide Composite

Ceramic composites, unlike monolithic ceramics, exhibit anisotropic mechanical properties. The stiffness and brittleness of the material also pose several problems to mechanical testing. One such problem is the gripping of the test-piece in a uniaxial tensile test and so three-point bend tests seem more appropriate for determining the basic material properties. Simple beam specimens are widely used in such testing because of their uniform cross-sectional area, which simplifies fabrication and calculations.

For an accurate measurement of the stiffness, we have to use a $\frac{S}{D}$ (outer span of rig / depth of beam) ratio which is large enough to avoid significant shear deformation (Jackson 1992). It is also unwise to use excessively thin sections as buckling would occur (Derby, Hill and Ruiz (1992)). A short beam test is usually used for the measurement of the ultimate interlaminar shear stress while a high span/depth ratio is used for measuring ultimate tensile (flexural) or compressive stresses.

Using simple bending theory:

$$\frac{M}{I} = \frac{\sigma}{y} = \frac{E}{R}$$

where $I = \frac{B \times D^3}{12}$ for rectangular section (Fig 3.3),

and $M = \frac{P \times d}{4}$ (for central concentrated loading)

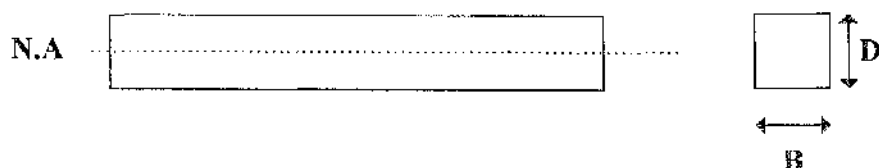


Fig 3.3 Rectangular beam

The maximum flexural stress occurring at the mid-span in the top and bottom fibres is:

$$\sigma_{\max} = \frac{3 \times P \times L}{2 \times b \times d^2}$$

Using the general rule of mixtures approach, we can also calculate the Young's modulus in the direction parallel to the fibres by:

$$E_c = E_f \times V_f \times B + E_m(1 - V_f) \quad \text{where } B = \frac{1}{2} \text{ for unidirection}$$

Experiments were therefore carried out by Gibson (1996) on 3-point bend specimens in a specially adapted jig fitted to a Lloyd LR30K test system. The system used interchangeable load cells and displacement control, to induce controlled damage in the material. The setup of the three point bending is shown in Fig 3.4.

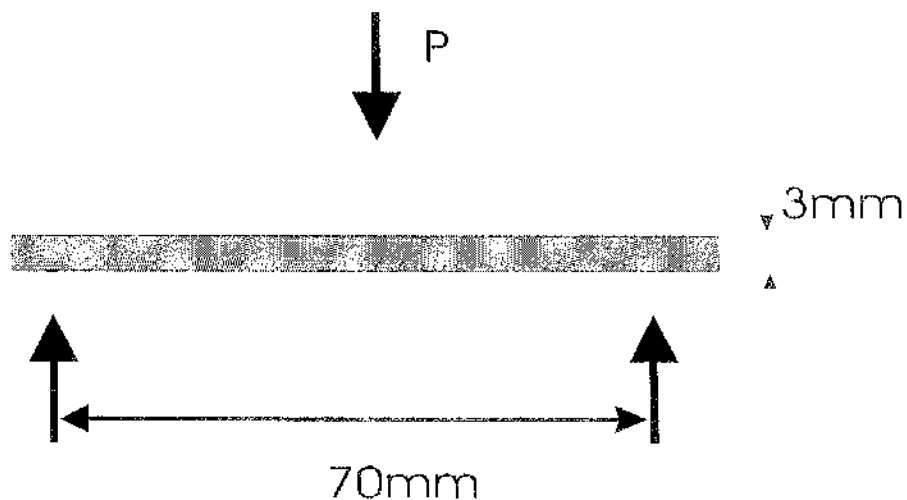


Fig 3.4 Experimental setup of three point bending on bend bar

3.3 Experimental Results

From a number of monotonic and cyclic 3-point bend tests on beams of active length 60mm, depth 3mm and width 10 mm, Gibson determined the basic physical and mechanical properties of the DuPont Lanxide.

The average density was found to be 2700 kg/m^3 , Poisson's ratio was assumed to be 0.29 and, from tabulated data such as Table 3.0, the average elastic modulus was found to be 132 GPa. The material exhibited a linear elastic curve up to the initiation of matrix micro-cracking, which occurred at an average stress of 156 MPa (which corresponds to a load of 132 N) and a strain of $1.07\text{E}-3$. From the non-linear response with increasing cracking at the fibre-matrix interface, the averaged maximum flexure stress, σ_u was found to be 380MPa.

However, the DLC manufacturer's data sheet (Sept 1989) has claimed an elastic modulus of 200MPa and flexure strength of 500MPa.

Test No.	E1 (GPa)	K1 (N/mm)	E2 (GPa)	K2 (N/mm)	OMF (MPa)	No. of cycles
RSB 001	110	346	-	-	164	1
	101	318				2
RSB 002	102	321	101	318	173	1
	100	314	84	265		2
	97	305	81	256		3
RSB 003	145	456	109	344	165	1
	115	363	92	288		2
	113	355	87	275		3
	98	308	71	224		4
	79	248	-	-		-
RSB 004	132	416	111	350	156	1
	101	318	95	301		2
	95	298	89	282		3
	91	286	74	233		4
	72	226	-	233		5
RSB 005	140	440	137	431	143	1
	127	400	114	358		2
	110	346	99	311		3
	95	299	92	289		4
	88	277	81	256		5
RSB 006	142	460	134	420	136	1
	132	419	109	344		2
	107	342	98	307		3
	95	318	85	266		4
	89	311	59	187		5
	70	243	27	92		6
RSB 007	140	450	135	424	151	1
	133	421	108	341		2
	111	358	77	243		3
	108	368	63	198		4
	100	355	60	188		5
RSB 008	141	430	109	342	157	1

Table 3.0 Cyclic loading data

From the cyclic loading graphs plotted by Gibson (1995), the (x, y) coordinates were measured and tabulated as in Table 3.1.

U (mm)	RSB 002	RSB 004	RSB 005	RSB 006	RSB 007	RSB 008	Average P(N)
0.0	0	0	0	0	0	0	0
0.2	75	95	90	100	130	90	97
0.4	140	165	170	175	200	150	167
0.6	200	225	225	240	220	225	223
0.8	260	245	265	290	265	275	267
1.0	315	315	320	335	310	315	318
1.2	350	330	350	360	350	355	349
1.4	330	315	345	365	345	-	340
1.6	300	310	330	350	350	-	328
1.8	285	290	340	360	340	-	323
2.0	-	175	-	355	340	-	290
2.2	-	-	-	265	250	-	258
2.4	-	-	-	145	225	-	185
2.6	-	-	-	150	220	-	185
2.8	-	-	-	160	180	-	170
3.0	-	-	-	165	130	-	148
3.2	-	-	-	170	105	-	138
3.4	-	-	-	110	100	-	105
3.6	-	-	-	-	85	-	85
3.8	-	-	-	-	80	-	80
4.0	-	-	-	-	70	-	70

Table 3.1 Average results of the load (P) and deflection (U)

The average graph plotted from the tabulated results is shown in Fig 3.5:

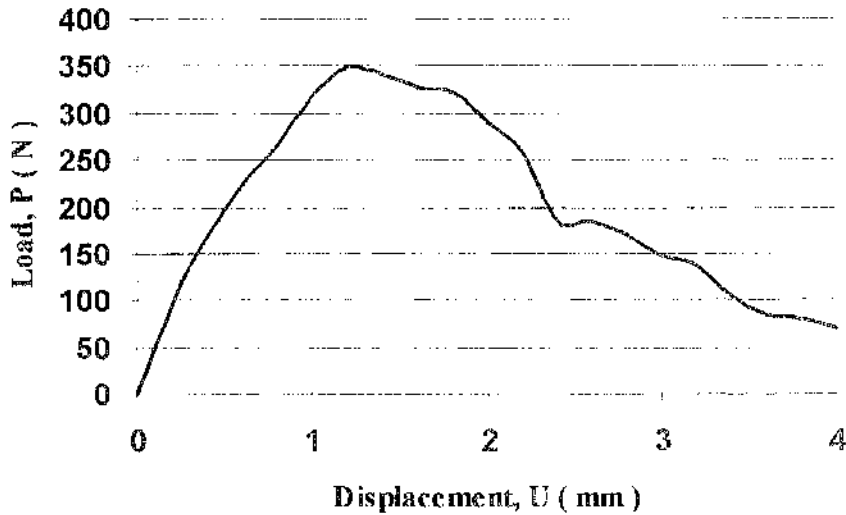


Fig 3.5 Average Load-Displacement Curve for Bend Bar

3.4 Damage Propagation In Three-Point Bend

3.4.1 Continuum Damage Mechanics

A general introduction to damage mechanics is given in Chapter 1. Here we consider the special case of a near-brittle ceramic material subject to 3-point bending. This loading system is of direct practical interest, since it arises in bone subject to knife impact, but it is also a particularly simple system to model computationally. This is so because the principal directions for the material on the centreline, the main area of interest, do not rotate. In addition, as a first approximation, the only active stress is the bending stress σ_{11} and so damage occurs only in the 11-direction on the outermost tensile side of the neutral axis.

Recapping from chapter 1, Figure 3.6 (a) and (b) shows two of graphs for the flexure loading and unloading of a simple beam. In Fig.3.6(a), the loading and unloading lines are initially parallel. This shows that the material has not been damaged. In Fig 3.6(b), the elastic modulus from the loading/unloading cycle shows a decrease in gradient. This indicates that the material has undergone matrix microcracking and the elastic modulus decreases as the material was loaded to a predetermined displacement (Kachanov, 1986).

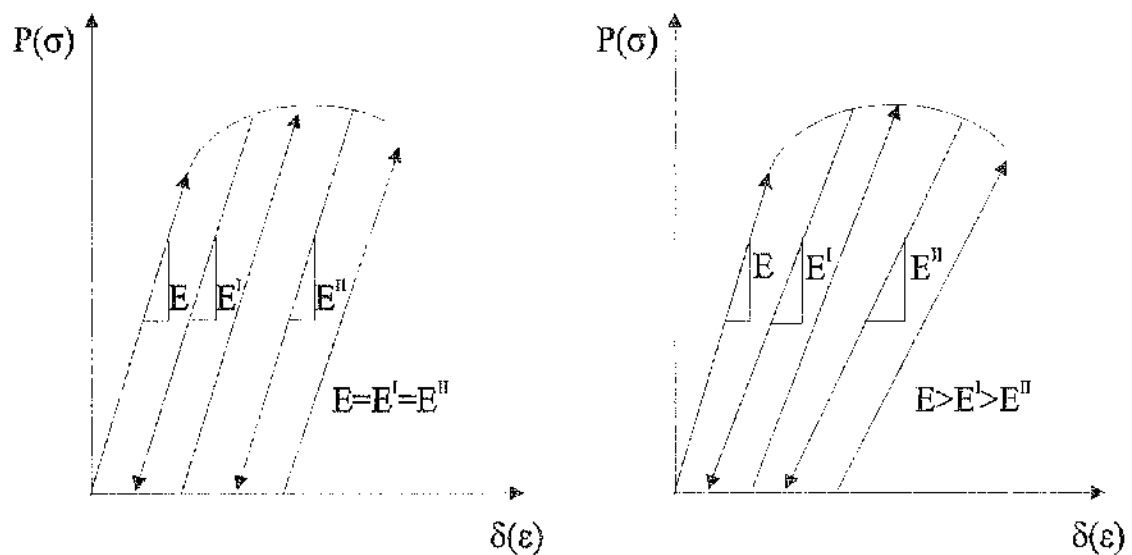


Fig 3.6 (a) & (b) Inelastic deformation graph

From Fig 3.6(b), the damage D can be measured as :

$$D = 1 - \frac{E}{^0E}$$

where E is the current elastic modulus of the (damaged) material and 0E is the initial elastic modulus of the (undamaged) material. On this basis Gibson derived a damage evolution curve for DuPont Lanxide as shown in Figure 3.7.

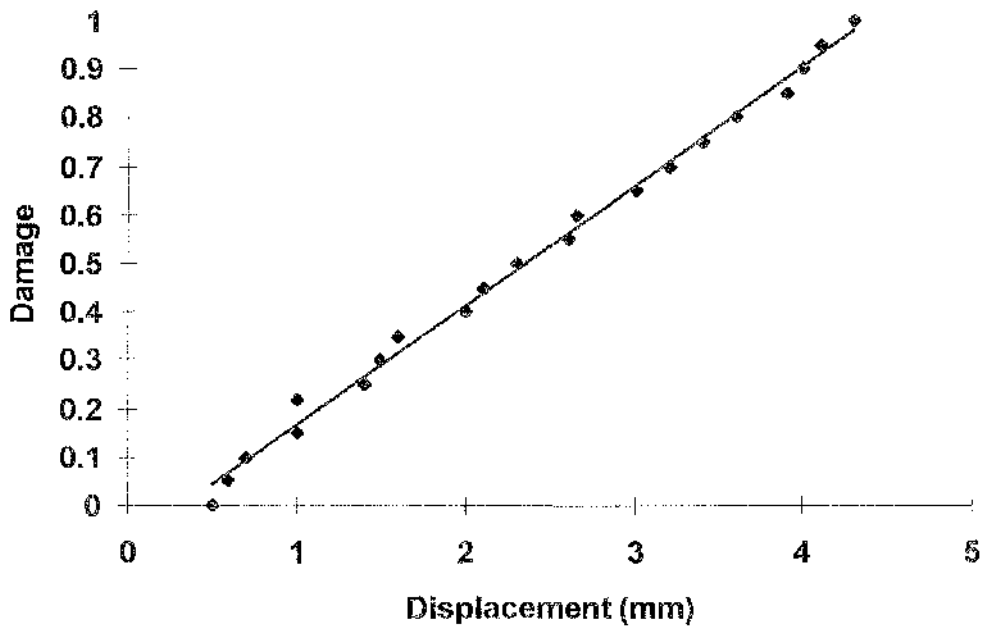


Fig 3.7 Damage-Displacement Curve

This calculation however assumed that the bending stress could be calculated from simple bending theory:

$$\frac{M}{I} = \frac{\sigma}{y} = \frac{E}{R} \quad \text{where } \sigma = \frac{3 \times P \times L}{2 \times b \times d^2}$$

which in turn assumes that the material is homogeneous and that there is no shift in the neutral axis. In reality, as damage propagates from the outer tensile fibres, the neutral axis shifts upwards and the load-bearing capacity of the specimen drops until all the remaining load is carried by a thin strip of the fibres on the initially compressive top surface. Under displacement controlled loading, this gives total but non-catastrophic failure. In short, Gibson's damage evolution law is not valid and the benchmark against which any computational modelling must be compared is his load-displacement curve for the bend specimen.

3.5 Finite Element Analysis

3.5.1 Introduction

Hibbitt, Karlsson & Sorensen, Inc has produced a finite element analysis system, Abaqus, which includes:

- Abaqus/Standard, a general purpose finite element programme
- Abaqus/Explicit, an explicit dynamics finite element programme that is fully vectorised for use on supercomputers
- Abaqus/Pre, an interactive preprocessor used to create finite element models for Abaqus
- Abaqus/Post, an interactive post-processing programme which provides displays and output lists from restart and results files written by Abaqus/Standard and Abaqus/Explicit.

Abaqus /Standard and /Explicit run as batch applications which assemble an input file for analysis. The input file, typically shown in Fig 3.8, contains model data and history data. The first is defined as a finite element model e.g nodes, elements, element properties while the latter defines a sequence of events or loadings for which the model's response is sought.

In Abaqus, this history is divided into a sequence of steps. Each step is a period of response of a particular type e.g static loading, a dynamic response etc. The definition of a step includes the procedure type, control parameters for time integration or, for the nonlinear solution procedures, the loading, and output requests.

There is also a clear distinction between steps involving nonlinear analysis and linear perturbation steps. Nonlinear analysis steps define a sequence of events that follow one another, in the sense that the state of the model at the end of the step provides the initial conditions for the start of the next step.

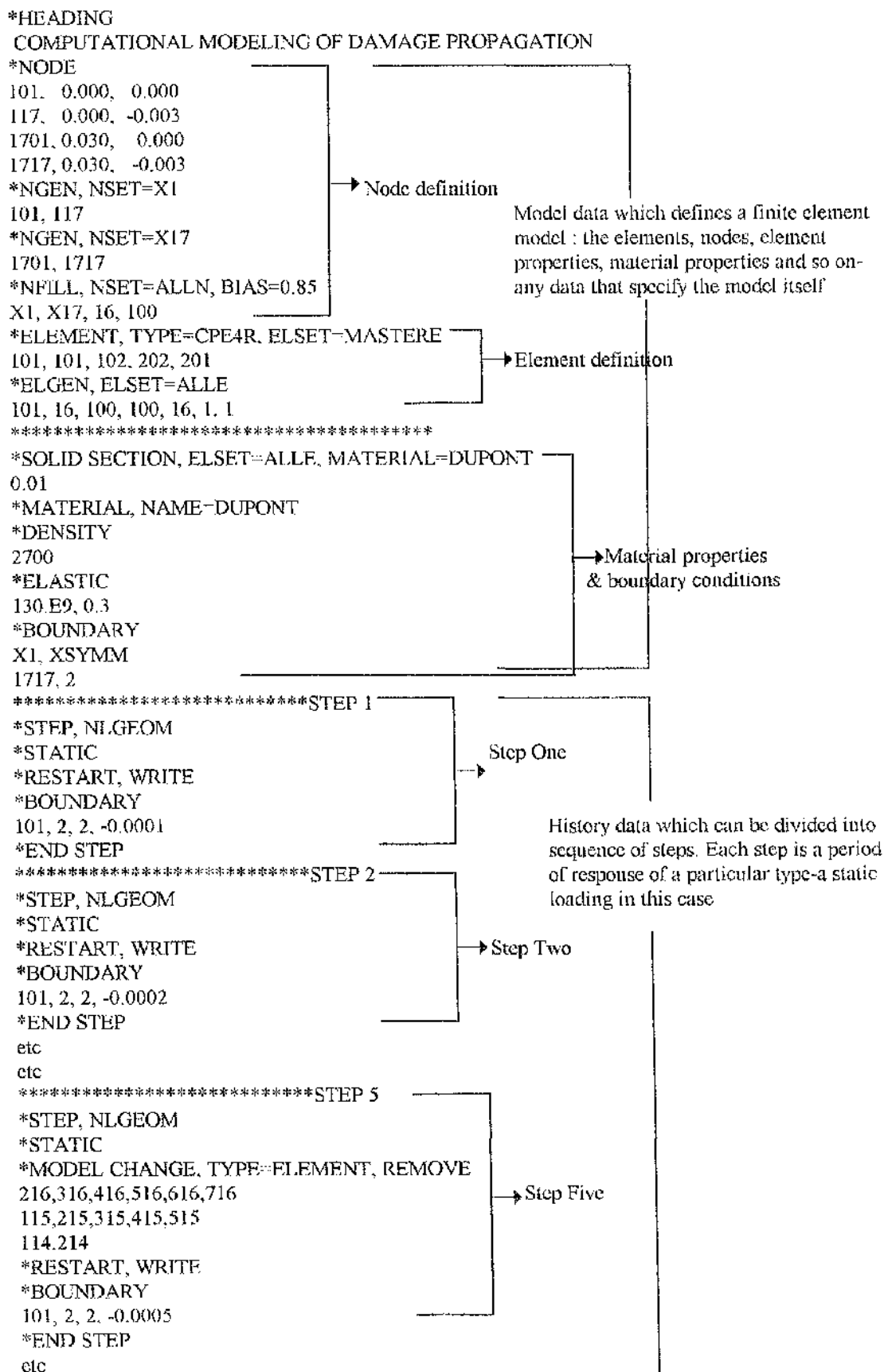


Fig 3.8 Input File

A linear perturbation analysis step provides the linear response of the system about the state at the end of the base state: the state at the end of the last nonlinear analysis step prior to the linear perturbation analysis. Abaqus/Post provides deformed configuration, contour, vector and X-Y plots, as well as animation of results. It is included with the Abaqus analysis modules. It can also be obtained separately for use on additional workstations or other display devices.

3.5.2 Computational Modelling Of Damage Propagation

A simple method of modelling damage propagation through a component is to manually delete elements in which the stress exceeds the known capacity of the material. Figure 3.9 shows a simple mesh of 256 4-noded plane-strain quadrilateral elements subject to 3-point bending. For this symmetric system, only a half-model (30mm instead of 60mm) need be analysed and to ensure that the correct stresses are returned, the plane-strain elements are given a depth of 10mm corresponding to the breadth of the beam.

This model was subjected to an increasing quasi-static displacement load using the Abaqus/Standard finite element system, until the matrix microcracking stress was reached in at least one element. The analysis was then stopped and the "failed" element was manually deleted from the mesh. The model was then reanalysed and any additional elements which had failed as a result of the redistribution arising from the previous element deletion were also removed. This iterative process was continued until all of the remaining mesh was below the matrix microcracking stress. The loading was then increased. Fig3.10(a) shows the initial loading of the model without reaching the matrix microcracking stress at step 1 while Fig3.10(b) and (c) shows the deletion of the elements at step 4 and 7.

This process of manual inspection and deletion of elements was continued until only a thin ligament, one element deep, remained on the upper side of the mesh as shown on Fig3.10(d). The beam had then, in effect, totally failed.

ABAQUS

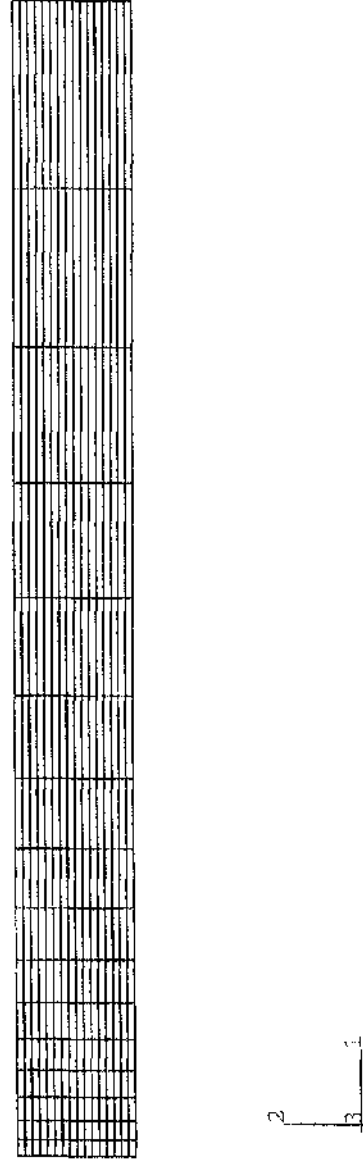


Fig 3.9 Simple mesh of 256 4-noded element

ABAQUS

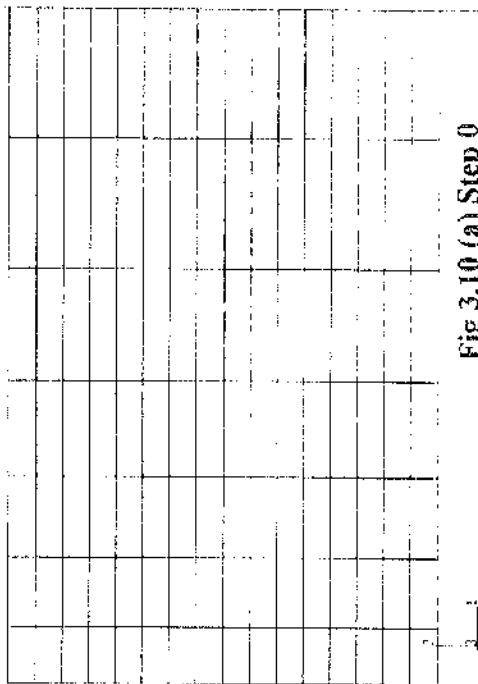


Fig 3.10 (a) Step 0

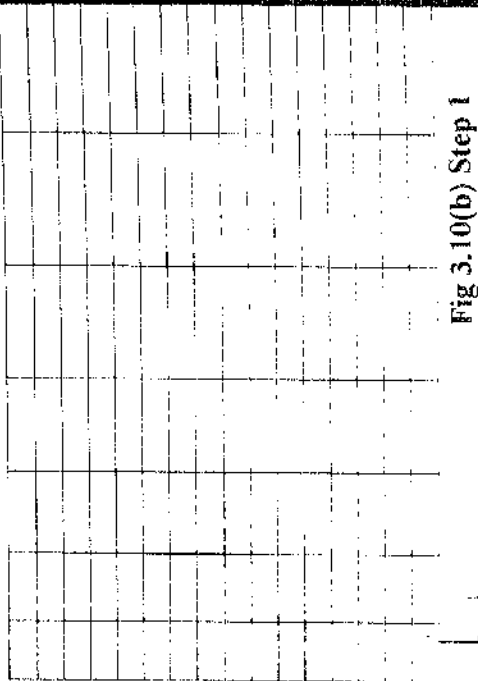


Fig 3.10(b) Step 1

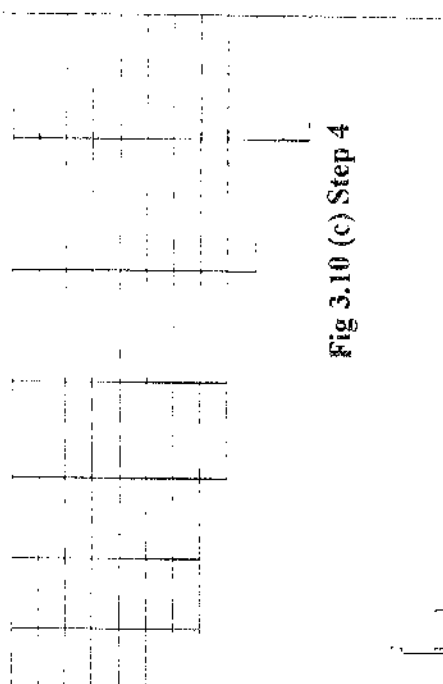


Fig 3.10 (c) Step 4

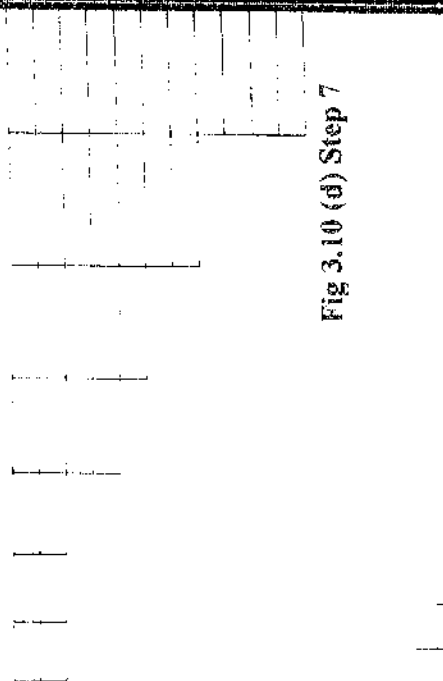
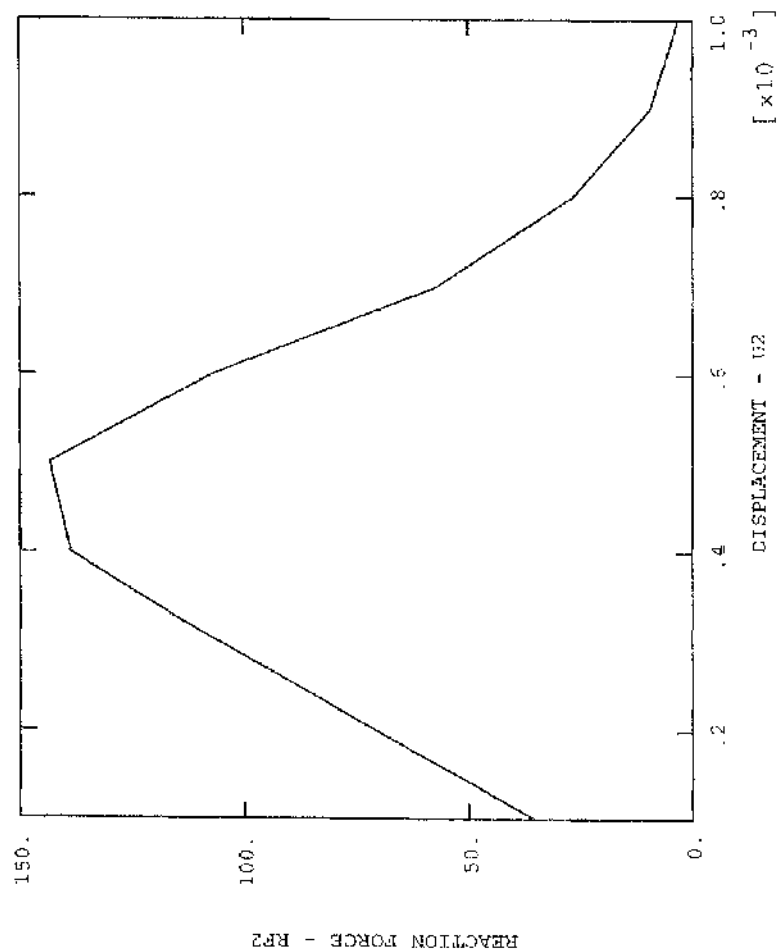


Fig 3.10 (d) Step 7

ABAQUS



NEW2_101

XMIN 1.000E-04
XMAX 1.000E-02
YMIN 3.090E+00
YMAX 1.434E+02

Fig 3.11 Load - displacement curve

The key result to be extracted from this analysis and compared with Gibson's results is the force-displacement plot at the load point. This is available for the Abaqus system as a graph of reaction force against displacement (Fig.3.11) at the appropriate node 101.

3.5.3 Conclusions

This simple method of modelling damage propagation has proved to be a technical success and provides benchmark deformation for future work. However it is in practise too tedious to manually intervene each step. What is required is a constitutive model of the damage propagation which automatically allows the degradation of the elastic modulus and the load-bearing capacity of the structure with increasing load.

Chapter 4

CONSTITUTIVE MODELLING OF A DAMAGING ALMOST-BRITTLE CERAMIC

4.1 Introduction

While the simple computational model of damage propagation described in Chapter 3 is useful, it requires too much manual intervention to be worth developing. Rather, it is necessary to build a constitutive model of the material which automatically allows degradation of the elastic modulus and the loadbearing capacity of the structure with increasing load. Abaqus/Standard contains two such models. The first is a continuum damage model of reinforced concrete, a ceramic composite which damages by microcracking of the matrix. This has been successfully used by McCafferty and Hancock (1992) to model toughened ceramics but it allows too little user control to be of general utility. The second model is of a ductile material which models damage by void growth in a ductile metal. This model admits modulus degradation and a loss of loadbearing capacity but it is only stable when the plastic work is significantly larger than the elastic strain energy. Neither model was then well suited for the present work.

The eventual aim is to model impact on a sample of bone. This is necessarily a three-dimensional contact problem which is not readily modelled in Abaqus/Standard. Attention was therefore switched to Abaqus/Explicit, that part of the Abaqus finite element suite specifically designed to analyse contact and impact problems. Although part of the Abaqus suite, Explicit is, for all practical purposes, a separate program which happens to have a similar input data format to Abaqus/Standard. The name comes from the "explicit" numerical integration method used. Explicit methods are more robust than the implicit methods used in Standard but they take a much larger number of much smaller increments to get to what might be the same result. They were thus unpopular until the advent of powerful workstations.

Explicit uses much the same input deck as does Abaqus/Standard but there are some differences and indeed drawbacks to Explicit, for example:

- it does not (yet) have as rich an element library as does Standard and contains only first-order (linear) interpolation elements such as 8-noded bricks
- it does not (yet) have such an extensive range of material options, eg there is no concrete model
- it does not have such extensive fracture mechanics features.

4.2 Finite Element Analysis

4.2.1 Mesh Generation and Boundary Conditions

A simple model of the bend bar was generated using Patran, an interactive preprocessor which provides complete geometry creation and mapping meshing tools. Since the physical specimen is symmetric, only a half model need be generated and appropriate boundary conditions imposed to enforce symmetry about the centreline. Because the model can be idealised as a long beam and the cross-sections are expected to have the same deformations, a 4-node (2-D) bilinear plane strain element, CPE4R, was chosen from the solid element library. Thus, the normal strain in the Z-direction, ϵ_{zz} and the shear strain, ϵ_{xz} and ϵ_{yz} may be assumed to be zero.

In Abaqus Explicit, the computer time involved in running a quasi-static analysis is very large (average time of at least 90 min per run) since the time increment cannot be longer than the time required to propagate a stress wave across an element. The mesh size also plays an important role in determining the analysis cost whereby:

$$\text{Analysis Cost} \propto N \frac{T}{\Delta t}$$

where N is the total number of elements in a mesh

T is the time period of the event being simulated

and Δt is the stable time increment:

$$\Delta t \approx \frac{L_{\min}}{C_d} \quad \text{and} \quad C_d = \sqrt{\frac{\lambda + 2\mu}{\rho}}$$

where L_{\min} is the smallest element in the mesh

C_d is the dilatational wave speed of the material

λ and μ are the effective Lamé's constants

and ρ is the material density

In order to avoid excessive analysis cost, the initial model was meshed with only 25 elements. However, this method of solving the computational analysis is inaccurate because if the mesh is too coarse, the inherent element approximations will not allow a correct solution to be obtained (NAFEMS, 1991). The mesh was later increased to 100 for a more accurate analysis, to be discussed in Section 4.3.1.

A velocity of 0.04 m/s was applied for a simulated time of 0.1sec to the centreline node on the upper face of the bar. This gives a total displacement of 4 mm, to correspond to Gibson's quasi-static three-point bend test on Lanxide. Fifty snapshots of the intermediate state of the models were written to the restart file (.RES), to be viewed later by Abaqus/Post.

Gibson has reported the density of the Lanxide to be 2740 kg/m³ and Poisson's ratio of 0.29. The initial elastic modulus calculated from a series of nondamaging flexure tests is 132 GPa. Under displacement controlled loading, the material exhibited a linear elastic response up to the initiation of matrix microcracking, at an average stress (σ_m) of 156 MPa (= 132N) and a strain (ϵ_m) of 1.07E-3. Until the initiation of microcracking, the material can be modelled by the linear elastic constitutive option in Abaqus/Explicit. Beyond microcracking to the maximum flexure strength (σ_u) of 380MPa (= 350N), the material damages and the response is nonlinear.

This can only be modelled by a user-defined constitutive model which, in Explicit, is entered via the VUMAT feature.

VUMAT is a Fortran 90 subroutine shell provided within the Abaqus/Explicit package which contains tools to allow the subroutine to be compiled and linked to the main program. The user is provided with an argument list which matches that in the calling routine in the main program. This list contains variables, such as strain increments, which are passed from the main program and variables, such as stress, which must be updated within VUMAT and passed back to the main program. The user is free to encode any constitutive model which expresses the stresses in terms of the strain increments.

VUMAT is a powerful feature but is not trivial to use and requires considerable care to write and considerable testing. Encoding a full 3-D continuum damage model would be a formidable task but, as noted in Section 3.3 and 3.4, fortunately the deformation undergone by the material in the specimens tested by Gibson is subject to simplifications which make the problem more tractable. Firstly, the material may be modelled in plane strain, which reduces the order of the deformation tensors, leaving only four active components.

Secondly, as a first approximation, the only active stress is the bending stress σ_{11} and damage occurs only in the 11-direction on the tensile side of the neutral axis. Thirdly, the loading is proportional and monotonic and the principal directions for the material on the centreline, the main area of interest, do not rotate. There is then no need to rotate the principal directions of the damage tensor.

These would be severe restrictions on a general damage theory but such conditions would apply to the common practical case of a knife impact on rib or long bones. The linear elastic constitutive equation for a non-damaging material in plane strain is:

$$\begin{bmatrix} \sigma_{11} \\ \sigma_{22} \\ \sigma_{12} \end{bmatrix} = \begin{bmatrix} \lambda+2*G & \lambda & 0 \\ \lambda & \lambda+2*G & 0 \\ 0 & 0 & G \end{bmatrix} * \begin{bmatrix} \epsilon_{11} \\ \epsilon_{22} \\ \epsilon_{12} \end{bmatrix}$$

where λ , G are Lamé's constants (the second of which is also the shear modulus).

For use in VUMAT, the direct stress components are more neatly expressed in the form:

$$\begin{aligned} \sigma_{11} &= 2*G*\epsilon_{11} + \lambda * (\epsilon_{11} + \epsilon_{22}) \\ \Rightarrow \sigma_{11} &= 2*G*\epsilon_{11} + \lambda * \epsilon_{ii} \text{-----Equation (1)} \end{aligned}$$

and similarly for σ_{22} . Here ϵ_{ii} is the trace of the strain tensor but $\epsilon_{33} = 0$ in plane strain. Equation (1) expresses the total stress in terms of the total strains. However VUMAT does not store the total strain directly and so these must be defined as internal state variables within the subroutine and passed back to the main program for storage between calls to VUMAT.

The above expressions can be applied to a damaging material once the matrix microcracking stress is exceeded provided Lamé's constants are calculated from the current secant modulus ES . However since the damage is assumed to occur only in the 11-direction it is also necessary to store the original value oES of the secant modulus and use this in the expressions for the other stress components. Rearranging:

$$D = 1 - \frac{E}{{}^oE}$$

gives

$$E = {}^oE*(1-D)$$

for the damaging direction and the main requirement is now for a damage evolution law to allow the secant modulus to be updated.

Damage evolution can be expressed as a function of any history parameter and the natural choice is probably the total strain in the direction of interest. It is known (Krajcinovic, 1996) that such a strain based damage evolution law produced mesh sensitivity in the results, with a fine mesh being less stiff than a coarse mesh.

Gibson has suggested a damage evolution law (Bend bar) in the form:

$$D = -0.0017U^2 + 0.26U - 0.076$$

$$\Rightarrow D = 52\varepsilon - 0.076 \quad \text{where } \varepsilon = \frac{6 \times U \times d}{L^2}$$

but, as noted previously, this is based on the erroneous assumption that the neutral axis does not move and that the stresses can be calculated from simple bending theory whereby the elastic limit of the material is not exceeded, and consequently the modulus of elasticity remains elastic.

Krajcinovic (1979) and Ouchterlony (1983) had worked out analytical solution for a perfectly brittle beam whereby the neutral axis can be determined by the equation:

$$(9 - 2m) * y_o^3 + 3(9 + 2m) * h * y_o^2 + 6(2 - m)h^2 * y_o + 2 * m * h^3 = 0$$

where $m = 3 * M / (2 * h^2 * B)$

B = parameter determined by curve fitting

M = bending moment

h = height of the rectangular cross-section

y_o = neutral axis

Since perfect brittleness is not the case here, the damage evolution law must be found by trial and error (curve-fitting method) by attempting to match the computed force-deflection response of the beam with Gibson's experimental results. This is done so by modifying ε in Gibson's equation with an empirical damage rate. Faneila and Krajcinovic (1986) used a similar method to determine the damage law in fibre reinforced concrete.

4.2.2 Vumat Subroutine File

The material properties; Undamaged modulus E_0 , Poisson's ratio ν , and matrix microcracking stress σ_{mm} , are programmed in the subroutine file as follows:

$$E_0 = \text{PROPS (1)}$$

$$\nu = \text{PROPS (2)}$$

$$\sigma_{mm} = \text{PROPS (3)}$$

where PROPS means the user-supplied material properties defined using the *USER MATERIAL option in the Abaqus Explicit input file. The initial shear modulus G_0 and Lamé constant λ were written:

$$2G_0 = \frac{E_0}{1.0 + \nu}$$

$$\lambda = \frac{\nu \times 2G_0}{1.0 - 2 \times \nu}$$

Before estimating the damage law, a state variable must be specified to store the constantly updated total strain tensors, based on the increment of the material deflection. A suitable update equation is:

$$\text{stateNew}(i,1) = \text{stateOld}(i,1) + \text{strainInc}(i,1)$$

This equation implies that the new strain ($\text{stateNew}(i,1)$) at each material point at the end of the increment is updated by adding the old strain ($\text{stateOld}(i,1)$) at each material point at the beginning of the increment and the strain increment tensor at each material point. With the constant update of the strain values, the damage parameter of the material can be updated and eventually model the non-linearity of the force-deflection curve.

Damage only increases when the linear elasticity reaches a point of initial matrix stress (σ_m) of 150MPa. This condition can be satisfied by an equation of the form:

$$\text{IF } \text{stateNew}(i,1) < \frac{\sigma_m}{\text{ElasticModulus}} \text{ then}$$

$$D = 0.0$$

ELSE

$$D = 52 * \text{stateNew}(i,1) - 0.076$$

The damaged modulus will be updated by the following equations:

$$E = E_o * (1.0 - D) \text{ where } E_o \text{ is the original modulus}$$

$$2G = \frac{E}{1.0 + \nu} \text{ where } \nu \text{ is Poisson's ratio}$$

$$\alpha = \frac{\nu \times 2G}{1.0 - 2 \times \nu} \text{ where } \alpha \text{ is the current Lamé's constant}$$

and the stress tensors:

$$\begin{aligned}\text{Trace} &= \text{stateNew}(i,1) + \text{stateNew}(i,2) + \text{stateNew}(i,3) \\ \text{stressNew}(i,1) &= 2G * \text{stateNew}(i,1) + \text{ala} * \text{Trace} \\ \text{stressNew}(i,2) &= 2G0 * \text{stateNew}(i,2) + \text{alao} * \text{Trace} \\ \text{stressNew}(i,3) &= 2G0 * \text{stateNew}(i,3) + \text{alao} * \text{Trace} \\ \text{stressNew}(i,4) &= 2G0 * \text{stateNew}(i,4)\end{aligned}$$

used to admit damage to σ_{11} only.

The damage evolution law used here is of course only an initial trial, to be amended until the computed results coincide with Gibson's experimental results.

4.3 Determination Of Damage Evolution Law By FEA

As mentioned previously, it is necessary to use a reasonable large element size in order to minimise computational cost. Conversely, it is necessary to use small elements to give accurate results. It is also necessary to formulate a damage law, triggered at an appropriate matrix-microcracking stress, that can give agreement, in this case, with Gibson's force-deflection results. A series of computational sensitivity analyses are therefore needed before a suitable compromise is reached.

Analyses of the damaging bend bar were carried out on a Sun workstation in a Unix environment. Every analysis typically took 50 increments, normally of the order of $1.E-8$ s, and 90mins CPU time to simulate 0.1 s of real time. This gives a deflection rate of 0.04m/s.

4.3.1. Mesh Size

A coarse mesh will cause inaccuracy in the solution to arise while too fine a mesh will result in expensive analysis cost. To determine a suitable compromise, analyses were done on meshes with 25, 50, 75, 100, 125 and 150 elements (Fig 4.1(a) - (f)) and the results compared in Table 4.0. These meshes were subject to three-point bending at a central deflection rate of 4mm/sec.

4.3.1.1 Results and Discussion

The load-deflection curves (Fig 4.2(a) - (f)) were plotted using the post-processor, Abaqus/Post and the summarised results were tabulated in Table 4.0.

No	Mesh Size (No. of elements)	CPU Time (Min)	Load (N)	Percentage Error (Relative to 150 elements)
1	25	41	412	51%
2	50	75	366	20%
3	75	100	349	9%
4	100	125	339	5%
5	125	143	344	2%
6	150	192	336	-

Table 4.0 Tabulated results of the mesh size

In general and as expected, the coarse meshes are stiffer and return a higher maximum for a given deflection than the finer meshes. This is plotted in Fig 4.3, which shows the maximum load decreasing with an increasing number of elements. The difference between the 25-element and 150-element meshes was calculated to be 20% whereas the error incurred between the 100 to 150-element meshes was only 5%.

ABAQUS



Fig 4.1 (a)

Fig 4.1 (a) 25-Element Model

ABAQUS



Fig 4.1 (b)

Fig 4.1 (b) 50-Element Model

ABAQUS



Fig 4.1 (c)

Fig 4.1 (c) 75-Element Model

ABAQUS



Fig 4.1 (d)

Fig 4.1 (d) 100-Element Model

ABAQUS



1

Fig 4.1 (e) 125-Element Model

ABAQUS



1

Fig 4.1 (f) 150-Element Model

ABAQUS

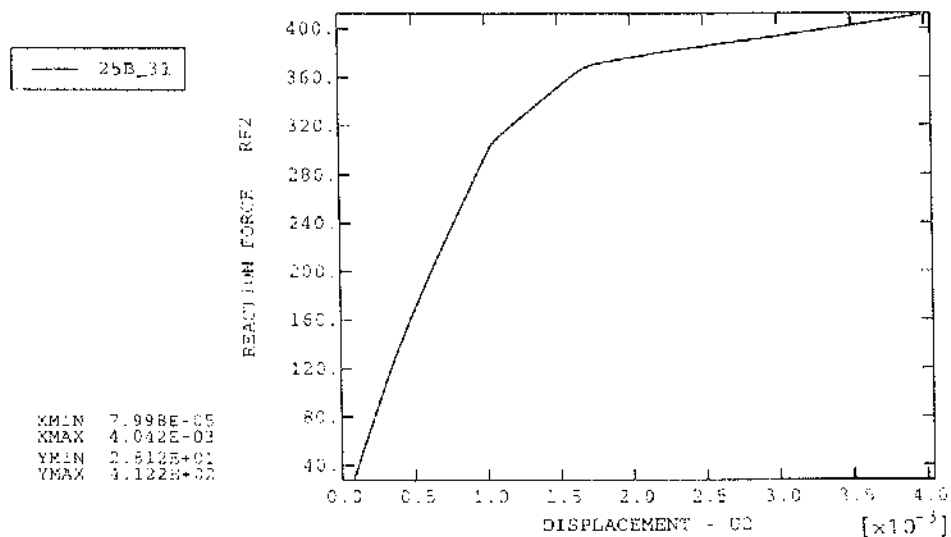


Fig 4.2 (a) 25-Element Model

ABAQUS

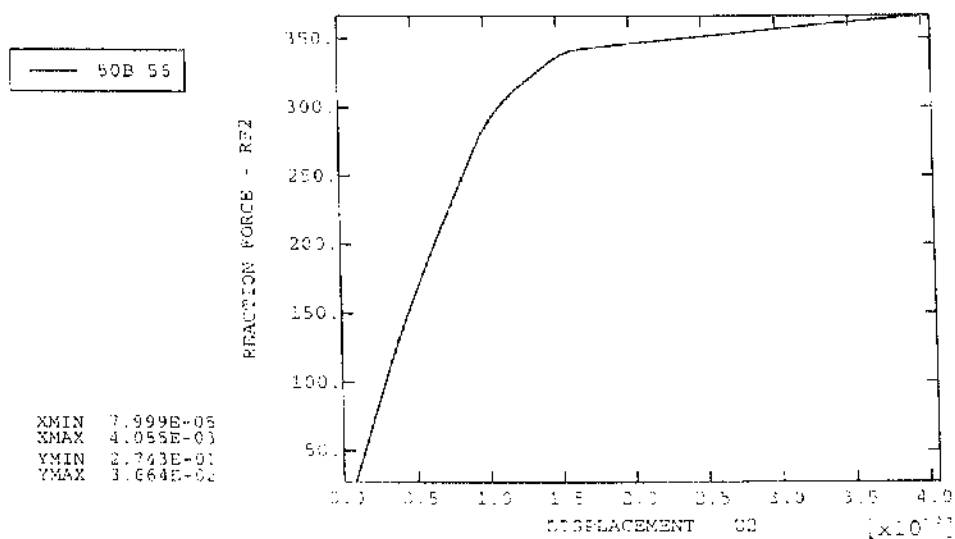


Fig 4.2 (b) 50-Element Model

ABAQUS

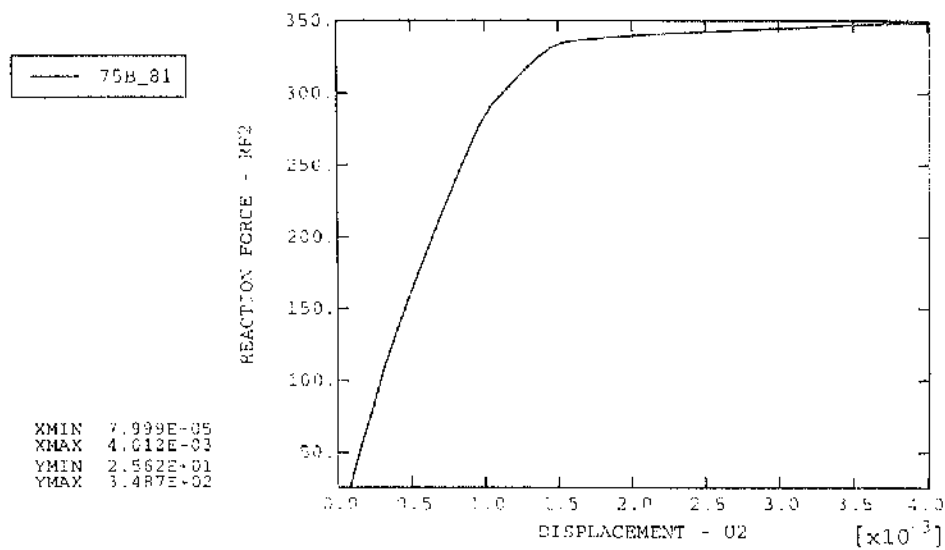


Fig 4.2 (c) 75-Element Model

ABAQUS

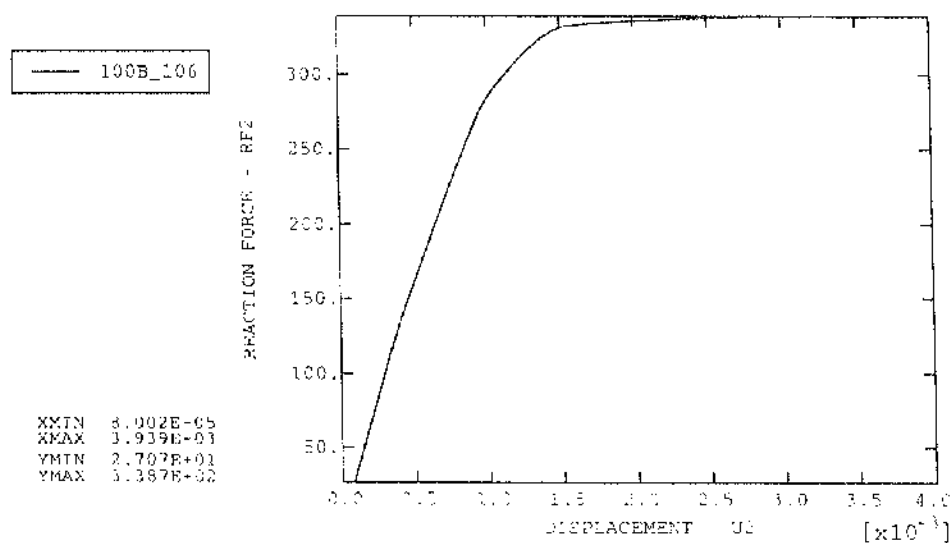


Fig 4.2 (d) 100-Element Model

ABAQUS

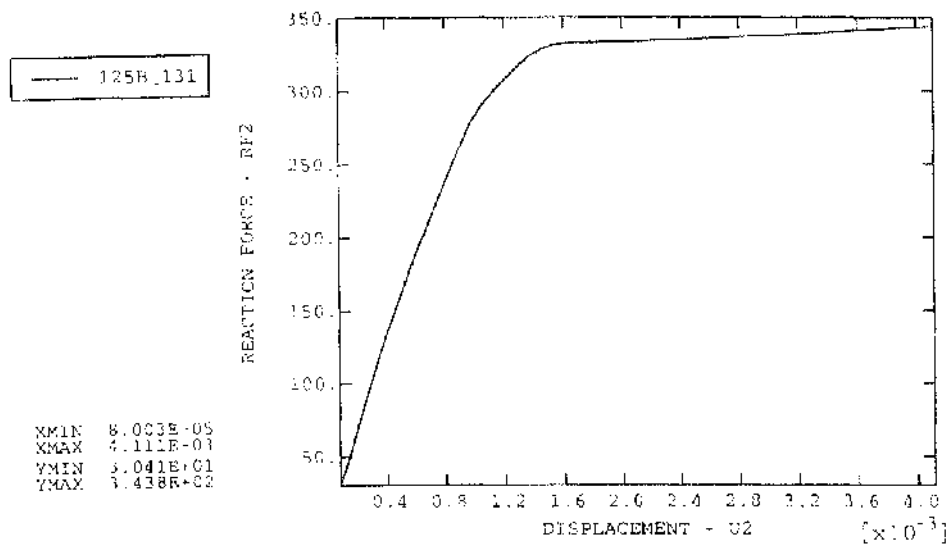


Fig 4.2 (e) 125-Element Model

ABAQUS

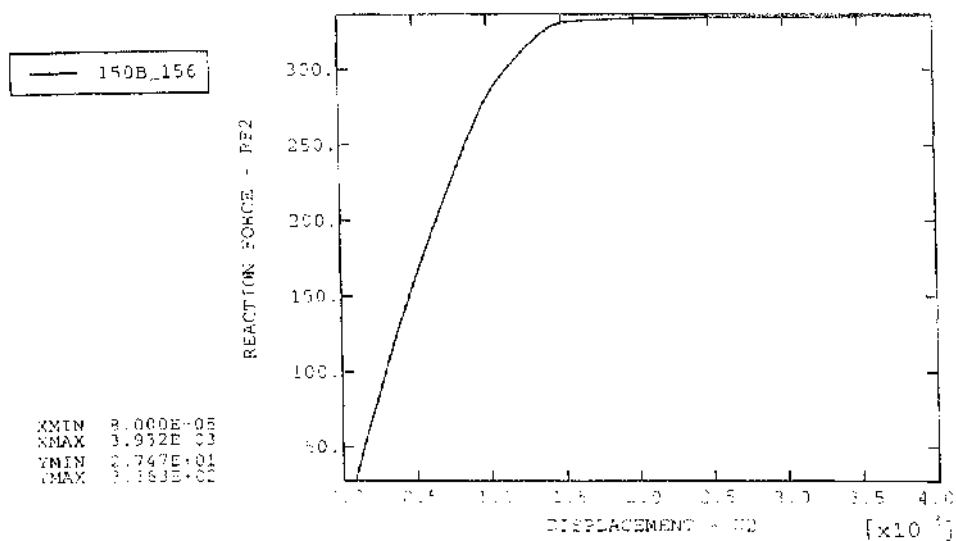


Fig 4.2 (f) 150-Element Model

The 100- element mesh is then a good compromise for future work, offering higher accuracy with lesser analysis cost. A graph of mesh size against CPU time is also plotted, in Fig 4.4. This implies that the analysis cost is proportional to the mesh size.

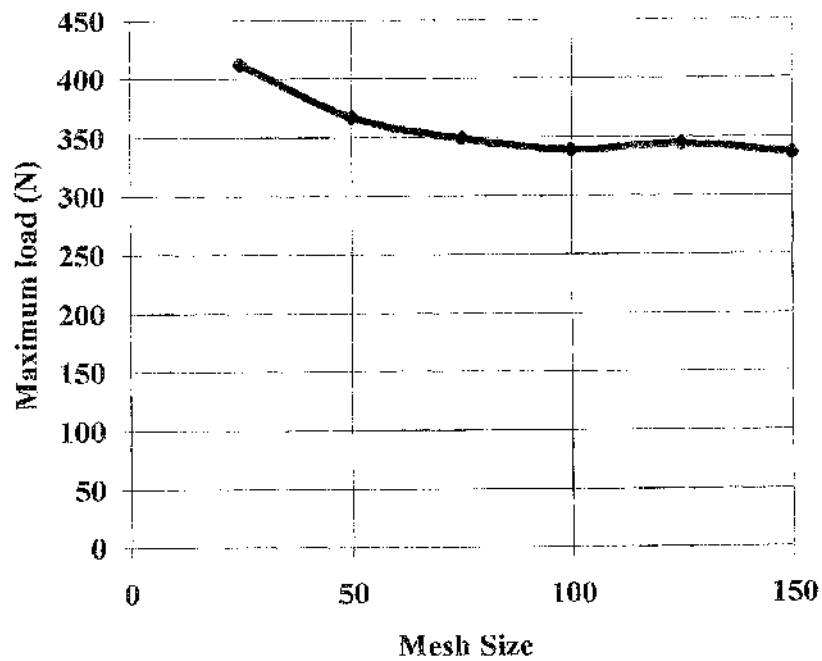


Fig 4.3 Mesh Size-Load Curve

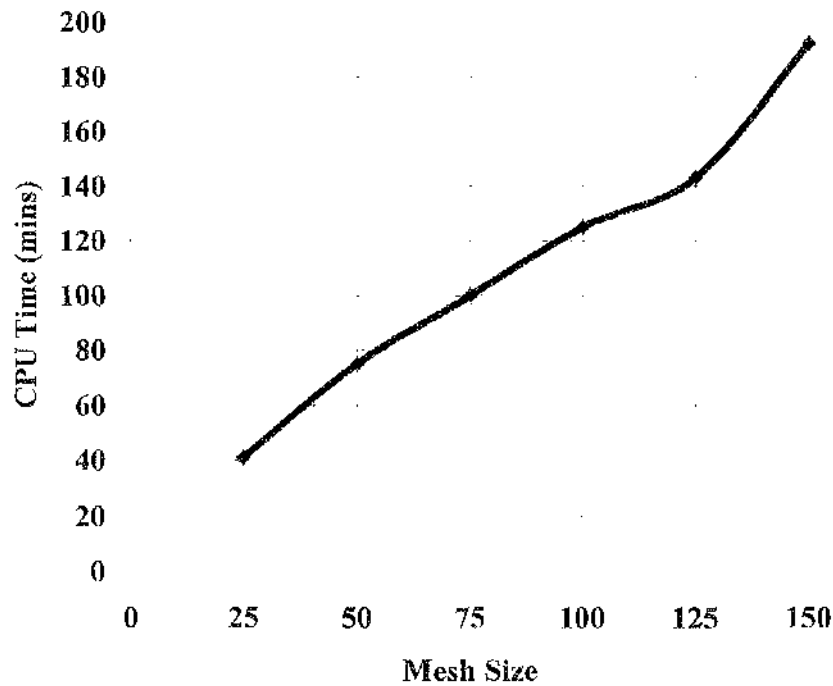


Fig 4.4 Mesh Size-CPU Time Curve

4.3.2 Damage Evolution Rate

Computational analyses were carried out to evaluate the sensitivity of the rate of damage evolution. This is largely determined by the linear term in the damage law. From Gibson's derivation :

$$D = 52 * \epsilon_{11} - 0.076$$

in which the "52" is the "damage evolution rate" or just "damage rate". Gibson experimentally determined the maximum load in the bend specimen to be 350N at a deflection of 1.7mm. A computational test based on this damage law was run but the maximum load obtained was 700N. The damage rate was therefore increased to 25, 75, 100 and 125 with a 100-element model (Fig. 4.5 (a) - (d)). The results are tabulated in Table 4.1.

ABAQUS

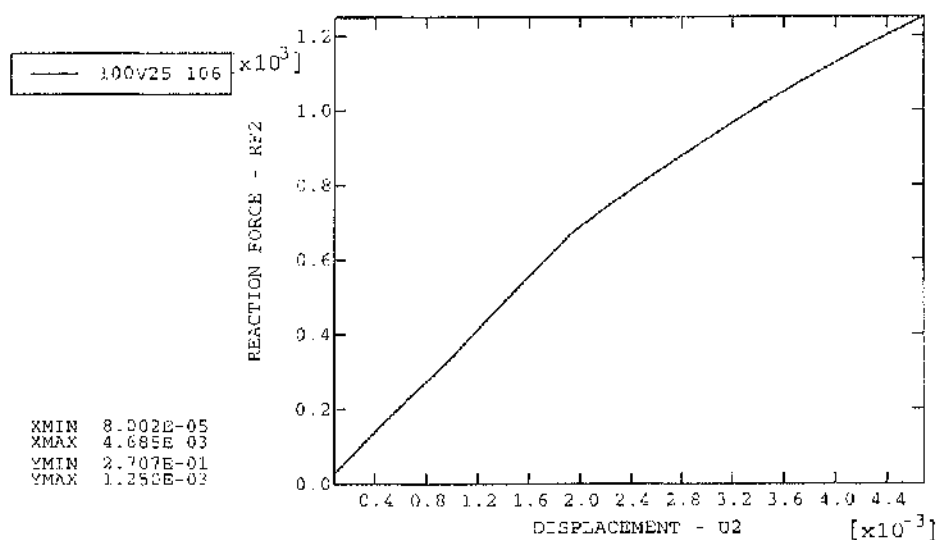


Fig 4.5 (a) Damage rate at 25

ABAQUS

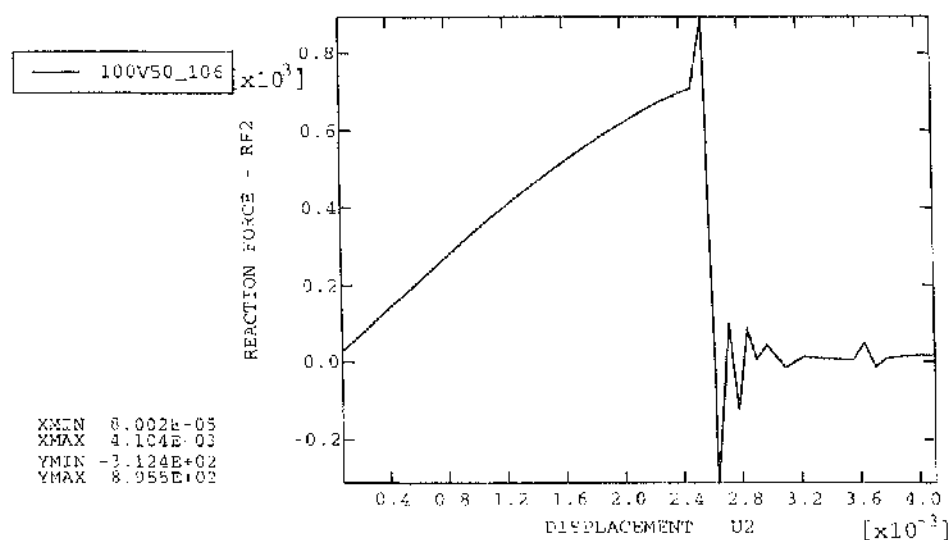


Fig 4.5 (b) Damage rate at 50

ABAQUS

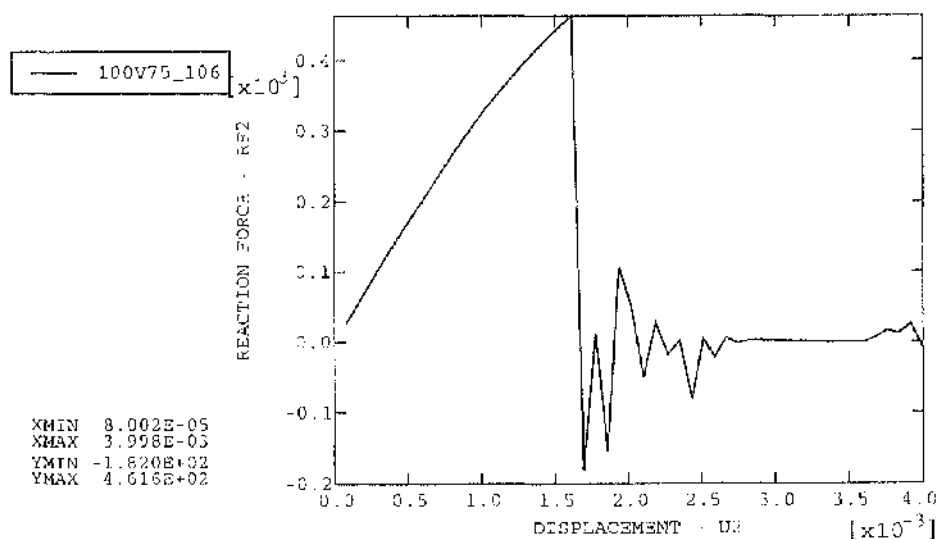


Fig 4.5 (c) Damage rate at 75

ABAQUS

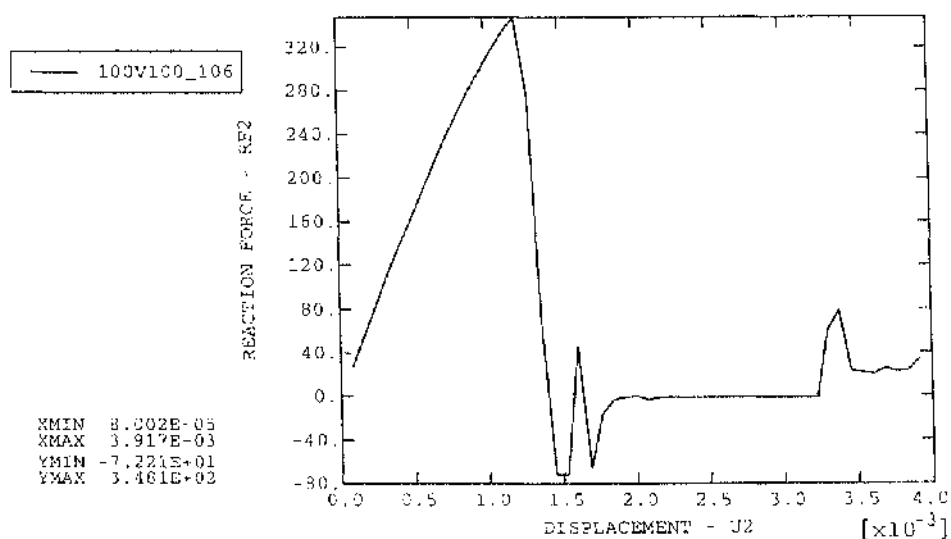


Fig 4.5 (d) Damage rate at 100

4.3.2.1 Discussion And Results

Summarising the results of Fig 4.5 and Table 4.1 gives Fig 4.6(a) and (b).

	Test1	Test 2	Test 3	Test 4
Damage rate	25	50	75	100
Max. load, RF2 (N)	Out of range	700	462	348
Corresponding deflection, U2 (mm)	Out of range	2.6mm	1.6mm	1.5mm

Table 4.1 Results of the 100-element model tested with varying damage rate.

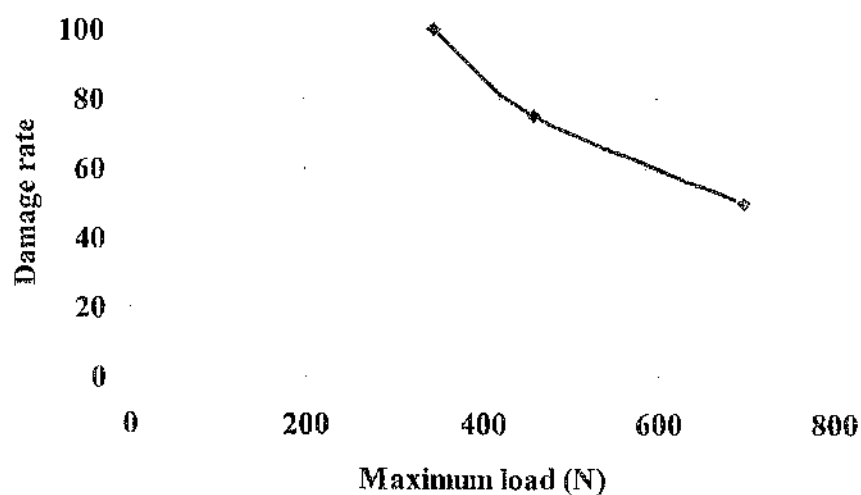


Fig 4.6 (a) Maximum load - Damage rate curve

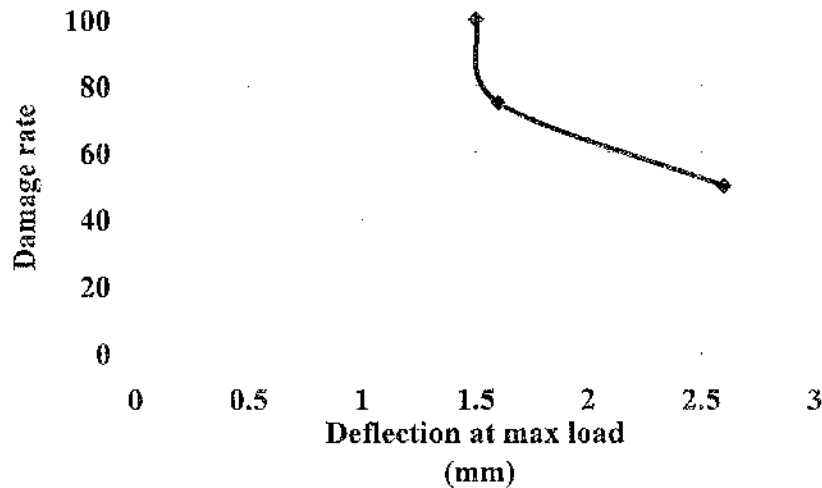


Fig 4.6 (b) Deflection at max load v. Damage rate

A damage rate of 25 gives almost no damaging effect within the range of deformation of the bending model and so the curve plotted on Fig 4.5 (a) is almost linear. As the damage rate increases from 75 to 100, the maximum load decreases dramatically although the corresponding deflection-to-failure stays almost constant in this range. This is shown in Fig 4.6 (a) and Fig 4.6(b).

Using a damage rate of 100 gives reasonable agreement with Gibson's experimental results; the maximum load obtained computationally is 348N compared to Gibson's 350N while the computed deflection at this load is 1.5mm, compared with Gibson's 1.3mm. The difference is only about 0.5% in load and 6% in deflection (Fig 4.7).

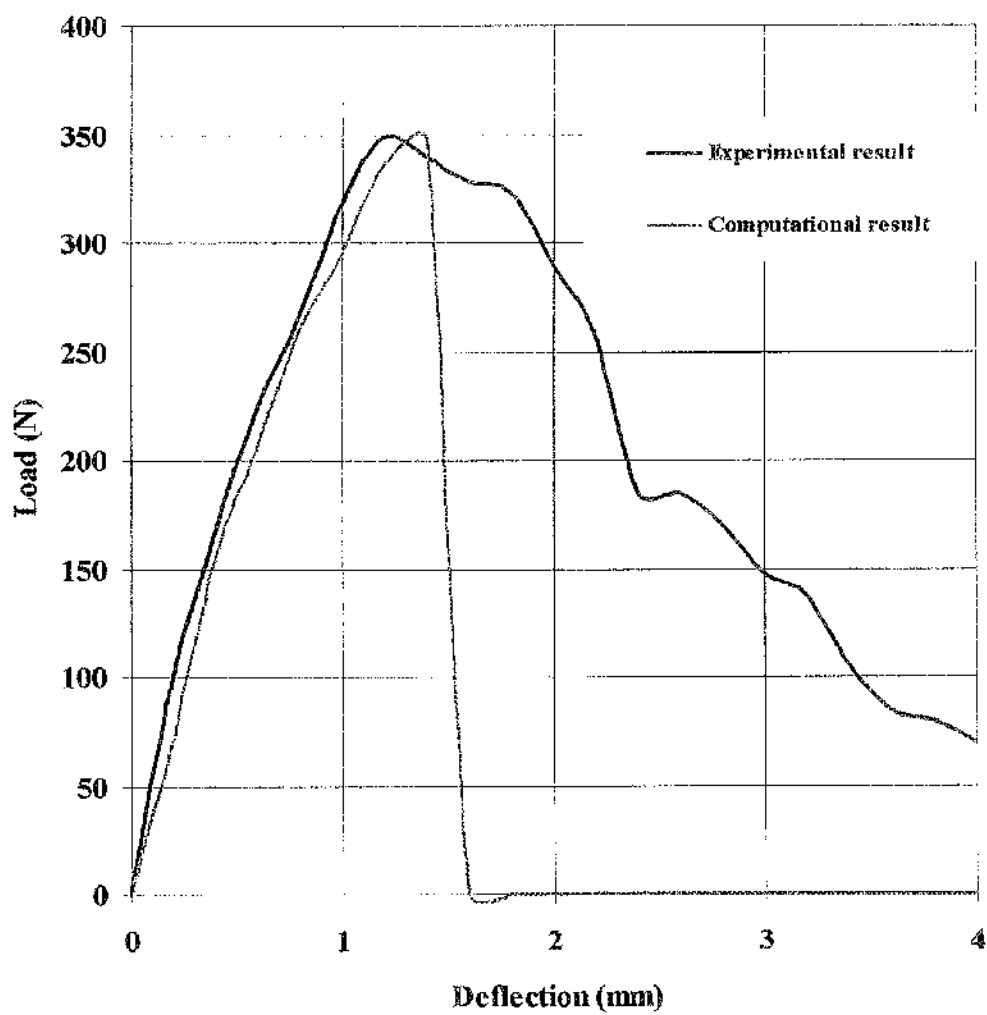


Fig 4.7 Computational and Experimental plots

4.3.3 The Sensitivity Of The Results To Matrix Microcracking Stress

Similar analyses were performed as a computational experiment to determine the sensitivity of the peak force to the matrix microcracking stress, σ_m . A range of σ_m , from 50 to 300MPa was used and the bend bars were subjected to the same displacement of 4mm, ie a velocity of 0.04 m/s for a simulated time of 0.1sec. A 100-element model was accompanied with damage rate of 50 for these experiments. The results are tabulated as in Table 4.2 and plotted on Fig 4.8.

Test No.	Matrix microcracking stress, σ_m (MPa)	Maximum load, RF2 (N)
1.	50	651.7
2.	100	643.8
3.	150	643.6
4.	200	637.5
5.	250	638.7
6.	300	638.4

Table 4.2 Results of the microcracking stress and maximum load

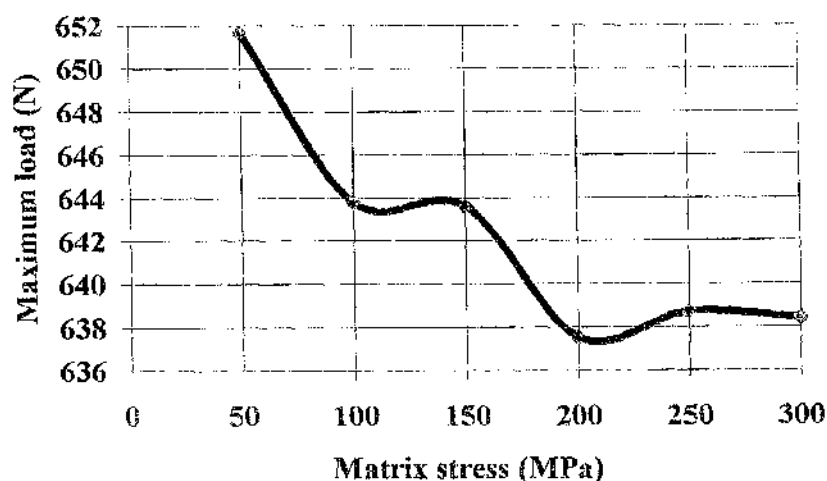


Fig 4.8 Effect of matrix stress on maximum load

4.3.3.1 Results And Discussion

Tests 1 to 4 from Fig 4.8, show a small decrease in the maximum reaction force, RF2, at the load point as σ_m is increased. Test 5 shows a slight increase in reaction force but overall, the changes are insignificant (about 2% difference only). In short, changes in σ_m do not make significant changes to the reaction force and the damage law is then not particularly sensitive to the choice of σ_m .

4.4 Conclusions

Abaqus/Explicit uses an excessive number of tiny increments to reach a solution for this type of problem. This occurs because Abaqus/Explicit chooses a stable time increment based on the time for a stress wave to cross an element. This introduces an absolute scale into the analysis and sets a lower bound on the element size. It also limits the scope for element refinement as a means of removing the expected mesh sensitivity of the damage law.

For the quasi-static analyses performed here, inertia forces and hence material density are not important and, since the elastic wave velocity is proportional to $\sqrt{E/\rho}$, the density can be given an artificially high value (of the order of 1.E8) to reduce the CPU time. Such a stratagem is not open to the dynamic analyses which must eventually be performed to simulate knife impact.

Computational experiments have been carried out on Dupont Lanxide bend bars to determine the type of damage evolution law which might be feasibly written into a computational simulation. When the results were compared with Gibson's experiments, it was found that the force/deflection response is not sensitive to the choice of the matrix microcracking stress σ_m .

This is probably due to the fact that the damage law is fundamentally a strain-based equation and the microcracking strain is small compared to the total strain at the maximum load. This is useful, for it removes the need to have a precise value of σ_m in the damage law.

Significant changes result from modifications to the number of elements but the most important parameter is the damage coefficient. An experimental damage law of:

$$D = 52 * \epsilon_{11} - 0.076$$

was obtained by Gibson from cyclic loading/unloading tests on a 3-point bend specimen. However this is thought to be in error. In the current computational experiments, agreement with the experimental load-deflection curve could only be obtained (with 100 elements loaded to a displacement of 0.004m) by a damage law of the form:

$$D = 100 * \epsilon_{11} - 0.076$$

with the condition:

$$\text{if } (D > 1) \text{ then } D = 1$$

imposed to ensure that the physically impossible condition of "overfailure" with $D > 1$ does not occur.

The computed load-deflection behaviour of the bend bar in 3-point bend superimposed on the experimental result was shown on Fig 4.7. From the graphs, the maximum load plotted from Gibson's results is 350N at a displacement of 1.3mm while the computational results shows 348 at 1.5mm. This is modelled fairly accurately by the computational analysis of the three point bending.

The strain softening part of the loading history is not well represented in the computation but this may be due to the failure of the model to allow a more gentle method of load redistribution than element erosion. The accuracy of the computational results is most sensitive to the damage coefficient but can also be improved by increasing the number of elements in the model.

This damage coefficient has not yet been related, in the current work, to the physics of the process. Such a step is however necessary if a more general expression is to be derived, capable of analysing different geometries of different materials.

Chapter 5

Damage In Multiaxial Stress States

5.1 Introduction

In the computational analysis for the bend bar, attention was focused on the in-plane bending stress σ_{11} only, since this is the dominant stress which initiates the failure. In this section, the computational analysis is extended in an attempt to model a T-section specimen. This was originally designed (Gibson, 1995) to allow assessment of the mode-I (tensile) delamination which propagates due to through-thickness tension in the web of the specimen under 3-point bending.

The objectives of the current analysis are to mimic the stress-strain and load-deflection behaviour of this more complex geometry, based on the principles of the Continuum Damage Mechanics in more than 1-dimension. In an approach to this more general CDM model, it is advisable to gradually include additional stress components. The T-section is particularly useful here since, when it is subjected to increasing stress in three-point bending, cracking initiates in the plane-strain field which exists at the central void and then propagates as a mode-I failure down the web of the section along the fibre bundles as shown in Fig 5.1.

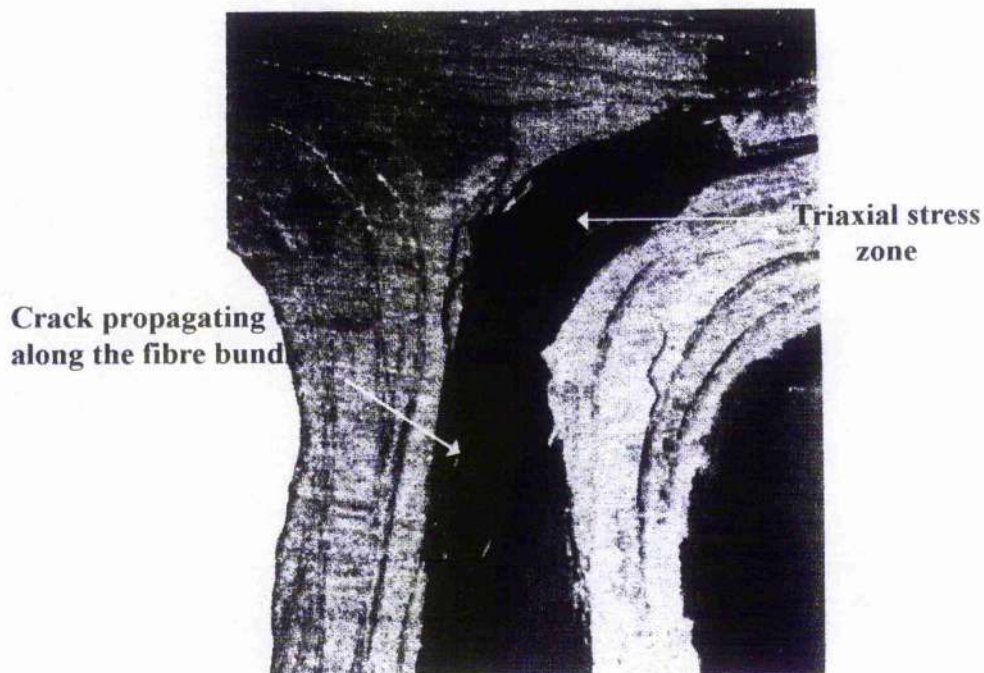


Fig 5.1 Dupont Lanxide T-section (Courtesy of Gibson)

5.2 Three- Point Bending On T-Sections

To complement the simple beam test, Gibson also tested a T-section beam, the so-called RST geometry, the function of which was to assess damage such as mode-I tensile delamination initiating from through thickness tension in the web. In an isotropic material with this geometry, the maximum stress concentration and hence the main damage site would normally occur at the root of the T but the fibres in the ceramic composite are laid in such a way as to produce a manufacturing defect in the centre of the specimen. This region is subjected to a multi-axial stress state, almost plane strain, and so failure propagates from there rather than from the root of the T. The results from the cyclic load/unloading flexure tests are shown in Table 5.0.

Test no.	E1 (GPa)	K1 (N/mm)	E2 (GPa)	K2 (N/mm)	OMF (MPa)	No. Of Cycles
RST001	-	839	-	253	116	1
	-	525	-	175		2
	-	433	-	49		3
	-	95	-	-		4
RST002	-	868	-	462	119	1
	-	664	-	258		2
	-	643	-	179		3
RST003	-	776	-	477	128	1
	-	703	-	262		2
	-	519	-	179		3
	-	433	-	136		4
	-	344	-	90		5

Table 5.0 Cyclic loading/unloading tests

These indicate an average structural stiffness of 828 KN/m. The material exhibited a linear elastic load-displacement response up to the initiation of microcracking which started at an average bending stress σ_m of 30 MPa (121 N) and strain ϵ_m of $2.1E-4$. From the onset of microcracking up to the average maximum flexure strength (σ_u) of 49 MPa, the behaviour was non-linear. Flexural failure for the T-section occurred at a strain of $8.6E-3$. The density of the Lanxide was found to be 2740kg/m^3 and Possion's ratio was taken as 0.3.

From Gibson's graph (1994), the load and deflection of the RST were averaged and tabulated in Table 5.1 where Fig 5.2 shows the averaged load-deflection curve.

P (N)				
U (mm)	RST 001	RST 002	RST 003	Average
0.0	0	0	0	0
0.2	190	150	150	163
0.4	215	210	210	212
0.6	215	220	215	217
0.8	220	225	217	221
1.0	210	220	220	217
1.2	210	210	220	213
1.4	200	-	217	209
1.6	200	-	210	205
1.8	190	-	205	198
2.0	185	-	200	193
2.2	170	-	195	183
2.4	170	-	190	180
2.6	160	-	-	160
2.8	140	-	-	140
3.0	100	-	-	100
3.2	75	-	-	75
3.4	60	-	-	60
3.6	50	-	-	50
3.8	45	-	-	45
4.0	40	-	-	40

Table 5.1 Averaged load and deflection

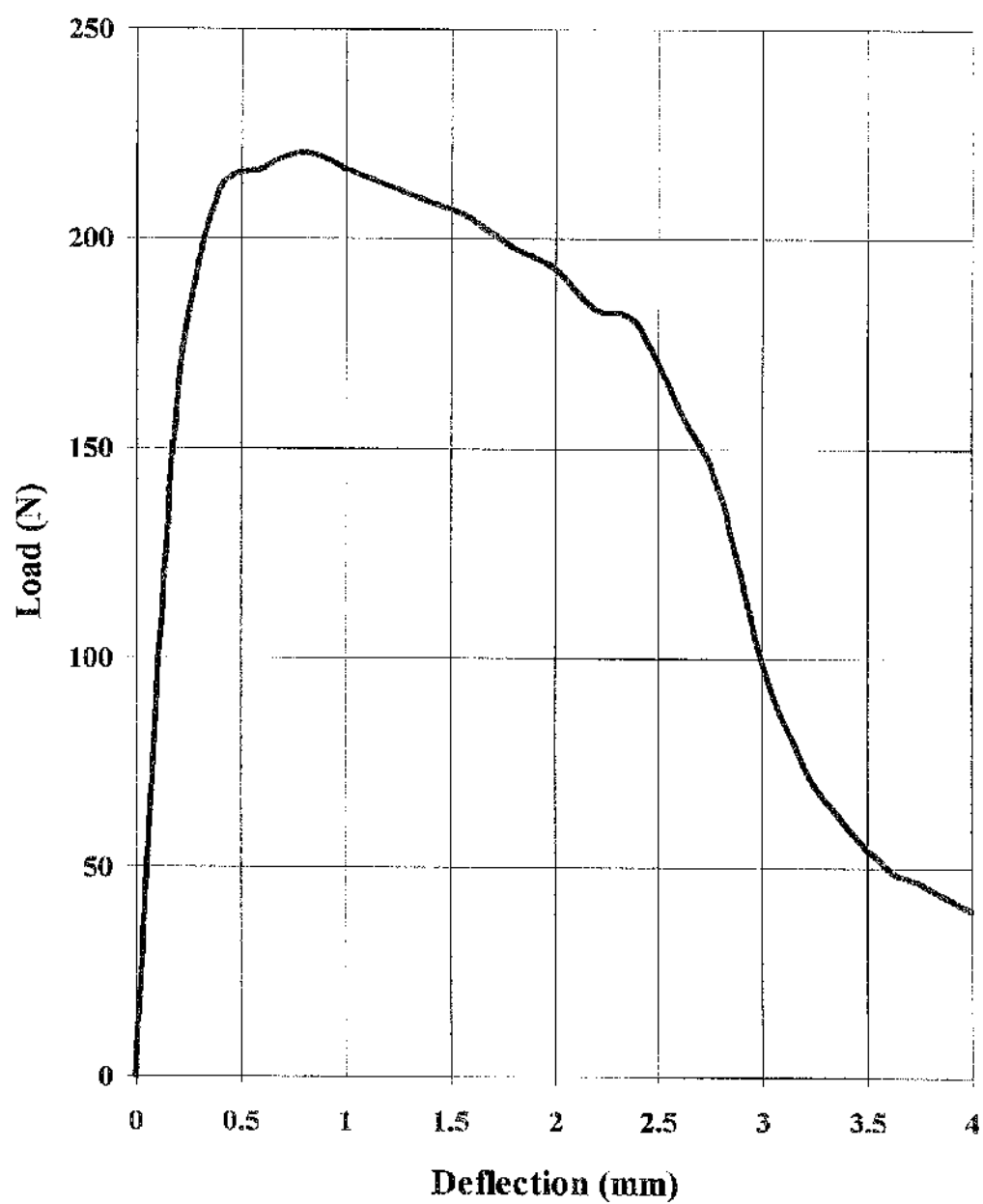


Fig 5.2 Average Load-Deflection curve for RST

5.3 Finite Element Analysis

Two finite element models were generated using Patran, one with 26 elements and the other with 202. Since the physical specimen is symmetric, only a half of the model needs to be generated. The appropriate boundary conditions are imposed to enforce symmetry about the centreline. The mechanical properties for the analysis were provided by Gibson.

Again, since Abaqus/Explicit is a dynamic analysis program but a quasi-static solution is required, an appropriately slow loading rate has to be chosen to eliminate any significant inertia solution. The T-section was then loaded at a velocity of 0.04m/s, for a simulated time of 0.1s, on the centreline of the node on the upper face of the T-section. This gave a total deflection of 4mm at the midspan, which approximately corresponds to Gibson's three point bend test on Lanxide. The simulation was written in Abaqus/Explicit input file accompanied by a Vumat sub-routine file to define the mechanical constitutive behaviour of the material. Fifty restart points, each of which gives a plot to be viewed later by Abaqus/Post were generated. The analysis of the T-section was carried out on a Sun workstation.

For this specimen geometry, Gibson has suggested a damage evolution law in the form of.

$$D = 0.015U^3 - 0.18U^2 + 0.64x + 0.18$$

which again, was based on the assumption that the neutral axis does not move and that the stress can be calculated from simple bending theory. This empirical law is different from that suggested for the bend bar, which cannot be the case if it is an intrinsic feature which models the material rather than structural response. The assumption regarding the neutral axis is also incorrect.

An initial trial was therefore made with a damage law similar to that used for the computational analysis of the bend bar, i.e:

$$D = 100 * \epsilon_{11} - 0.076$$

and an attempt made to match the computed force-deflection response of the T-section with Gibson's experiment results.

An initial run was carried out with the coarse mesh, 26-element model to estimate the stress distribution and the loading force throughout the structure. The accuracy is likely to be less than that using a more refined mesh of 202 elements but it does save on computational time in the initial trials.

5.3.1 Results And Discussion

The maximum loading force obtained from the 26-element mesh, with a damage coefficient of 100, was 410N at a deflection of 2.2mm. Comparing this result with Gibson's maximum loading force of 225N at 0.7mm deflection shows that the computational result was too high. It is not clear whether this is primarily due to the coarseness of the mesh or to an insufficient rate of damage and so the fine mesh was run with the same damage law.

However, analysis on the 202-element model was terminated prematurely and an error message was issued by the program stating that the ratio of the deformation speed to wave speed exceeded 1.0 in at least one element. Abaqus/Explicit checks for large deformation speeds in all the elements to prevent the element deforming or collapsing unrealistically. A warning message is issued if the ratio of deformation speed to dilatational wave speed in an element reaches a "warning ratio" value which defaults to 0.3.

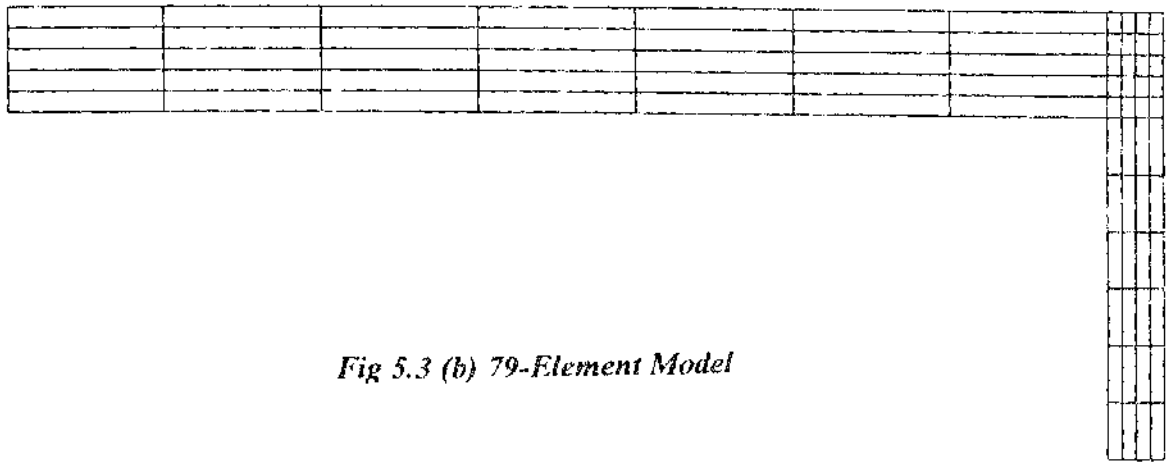
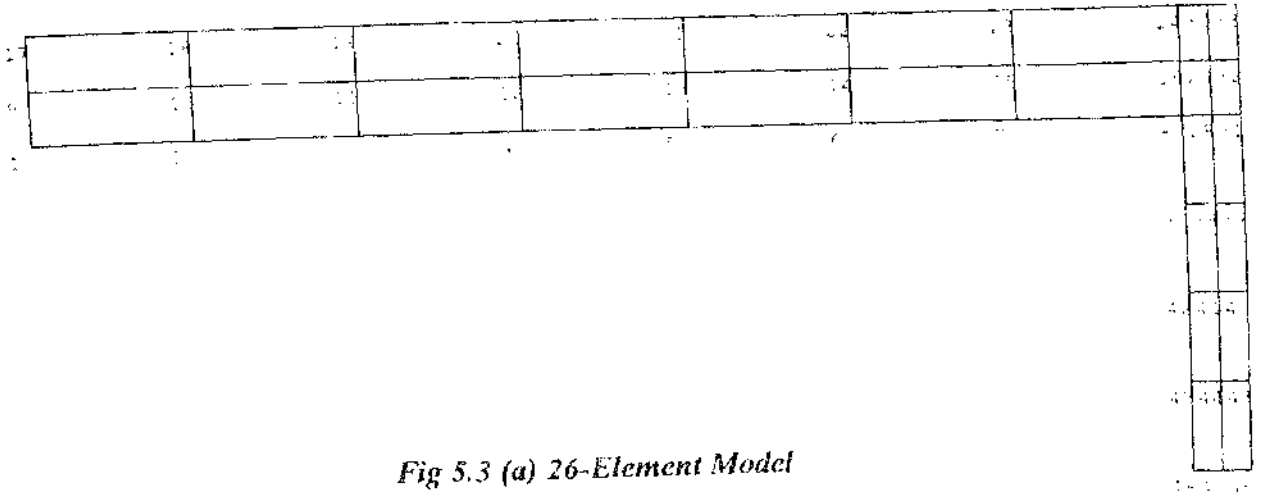
In most cases, when such a ratio is exceeded, a purely mechanical material constitutive relationship is no longer valid and a thermo-mechanical equation of state material is required. The analysis terminates completely when the ratio of the deformation speed to dilatational wave speed for any element is greater than the "cutoff ratio" at 1.0. Abaqus/Explicit allows the "warning ratio" limit to be redefined using the WARNING RATIO parameter and the "cutoff ratio" limit using the CUTOFF RATIO parameter on the *DIAGNOSIS option. However, this user-defined "cutoff ratio" is not applied to any model that has user-defined material behaviour like Vumat.

Since the problem is related to the absolute size of the elements, the mesh size was reduced from 202 elements to 162 but with no success. The mesh was further reduced to 79 elements, for which a maximum loading force of 418N occurs at a midspan deflection of 1.55mm. This is still much greater than Gibson's value. These results are summarised in Table 5.2 and plots of the undeformed and deformed mesh of the 79-element model, load-deflection curves of the 26 and 79 element models are shown in Fig 5.3 (a) to (d) and 5.4 (a) and (b). In these, the graph axis is shown as negative due to mainly compressive loading.

Test No.	No. of elements	RF2 (N)	U2 (mm)	CPU Time	Fig No.
1	26	420	2.2	52 min	5.5 (a)
2	79	418	1.55	267 min	5.5 (b)
3	162	-	-	-	
4	202	-	-	-	

Table 5.2 Summarised results of the computational models

ABAQUS



ABAQUS

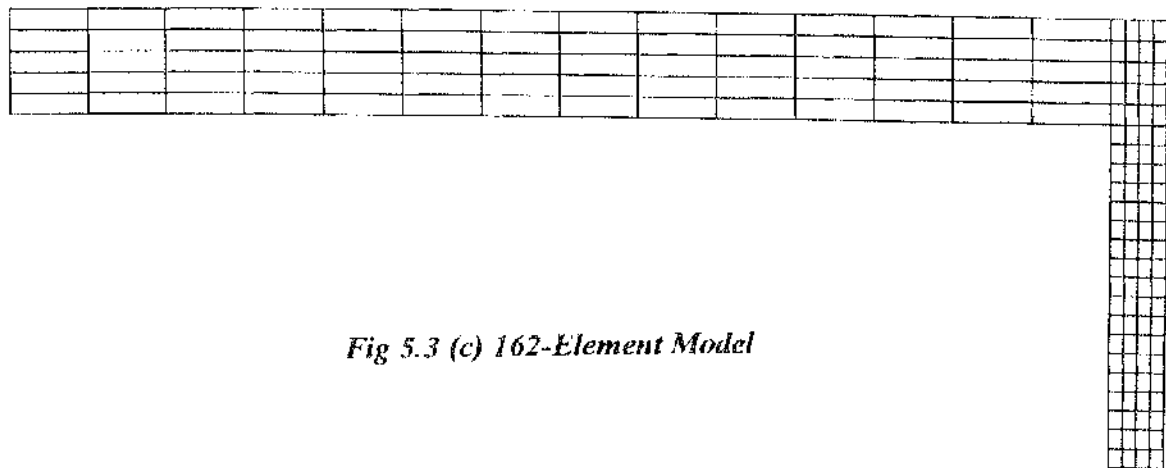


Fig 5.3 (c) 162-Element Model

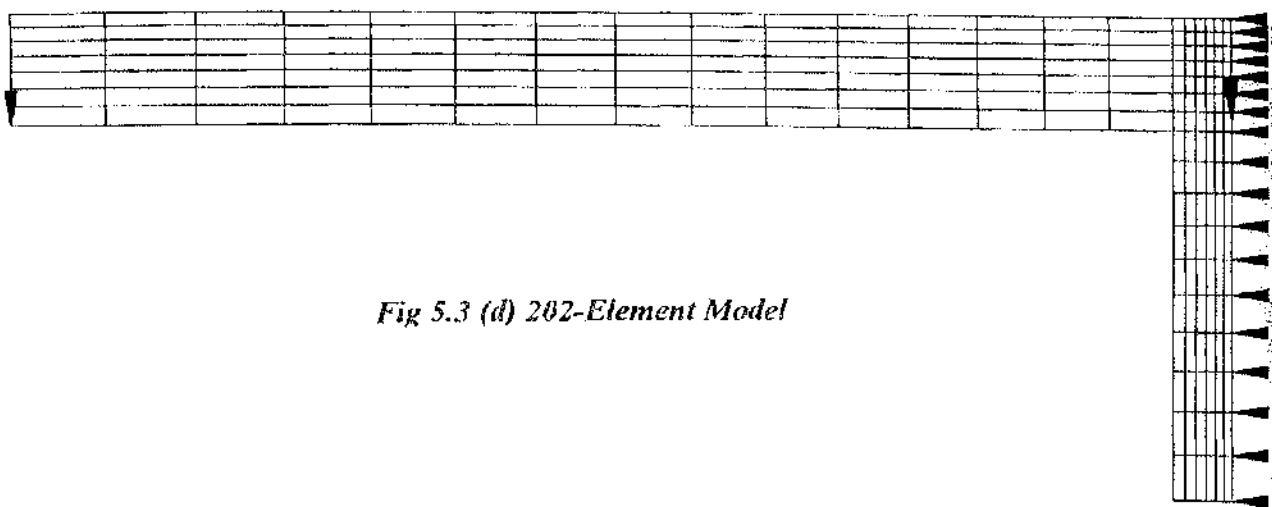


Fig 5.3 (d) 202-Element Model

ABAQUS



Fig 5.4 (a) Undeform T-section

ABAQUS

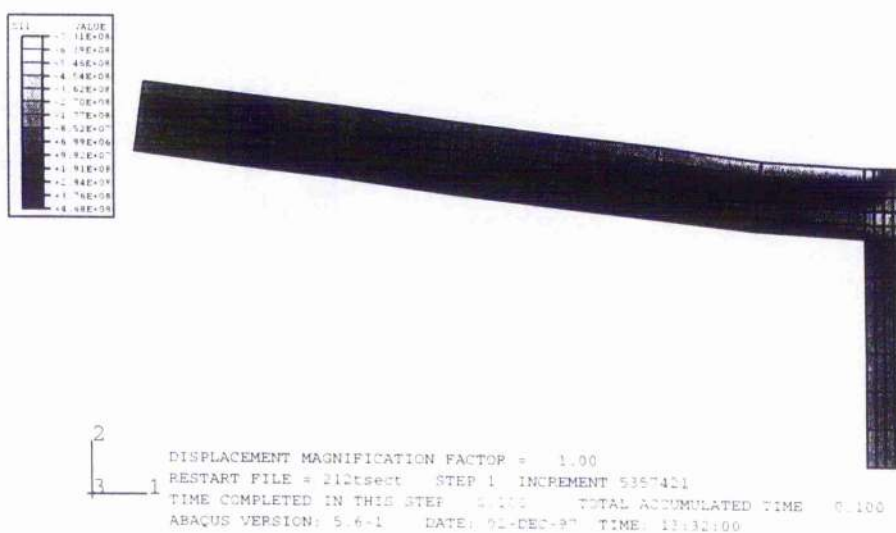


Fig 5.4 (b) Deformed T-Section at midspan deflection of 4mm

Four different sets of damage rate: 50, 100, 120 and 150 were tried out with the 79-element model in order to seek a value coincident with that of Gibson and examine the sensitivity of this maximum load to the damage coefficient.

The results are shown in Table 5.3 and Fig 5.5(a) and (b). The maximum loading force of 850 N obtained for the damage coefficient of 50 was far from that found experimentally. With damage rate of 120 and 150, the ratio of the deformation speed to dilatational wave speed was again exceeding the limit of 1.0.

Test No.	Rate of damage	RF2 (N)	U2 (mm)	Fig No.
1	50	850	3.3	5.6 (a)
2	100	420	1.55	5.6 (b)
3	120	-	-	-

Table 5.3 Tests on 79-element model with different damage rate

Clearly, there are features of the Abaqus/Explicit solution algorithm which were not well understood. The investigation of these features is beyond the scope of the current work and at this point, it seemed that a coarse mesh with a high damage coefficient was the best option to modelling the three point bend on T-section. Therefore the 26-element model, a very coarse mesh, subjected to a damage rate of 150 was chosen as the best compromise. The maximum loading force obtained was quite close to Gibson's experimental result of 300N at a deflection of 2.2mm.

A final computational experiment was made with the damage coefficient increased further to 200. This results in a maximum loading force of 200N at a midspan deflection of 1.0mm. This compares well Gibson's maximum loading force of 225N at 0.7mm, the percentage difference being only 2%. The results are tabulated in Table 5.4 and shown in the Abaqus plots on Fig 5.7(a) to (c).

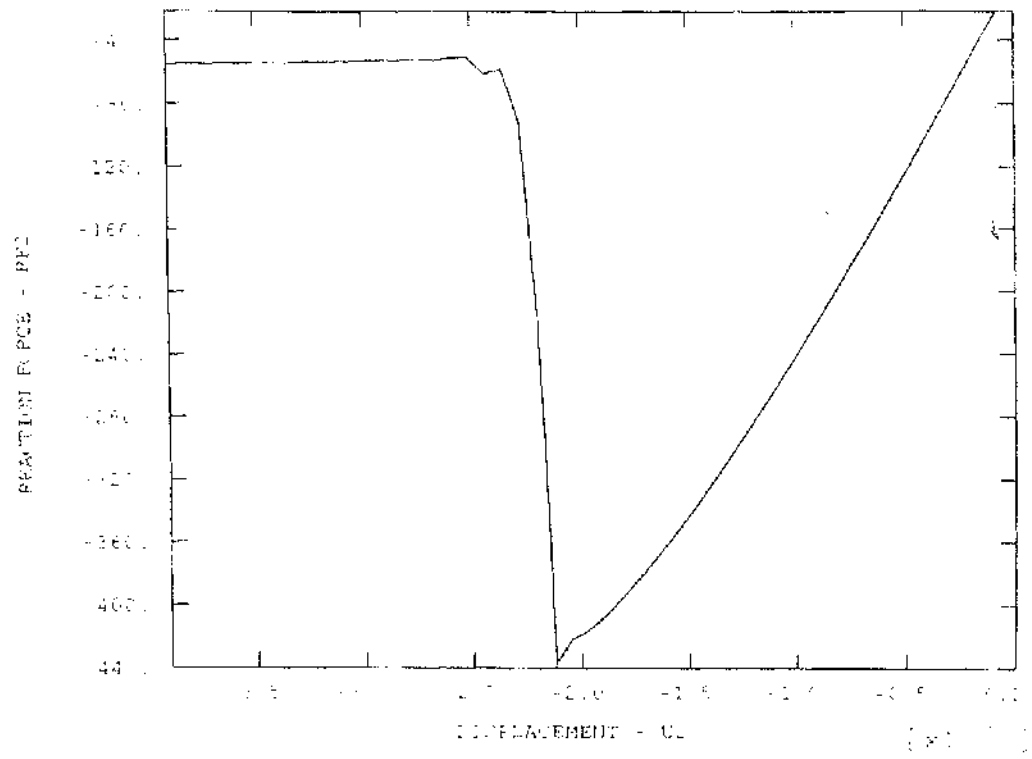


Fig 5.5 (a) Load-Deflection Curve of 26-Element Model

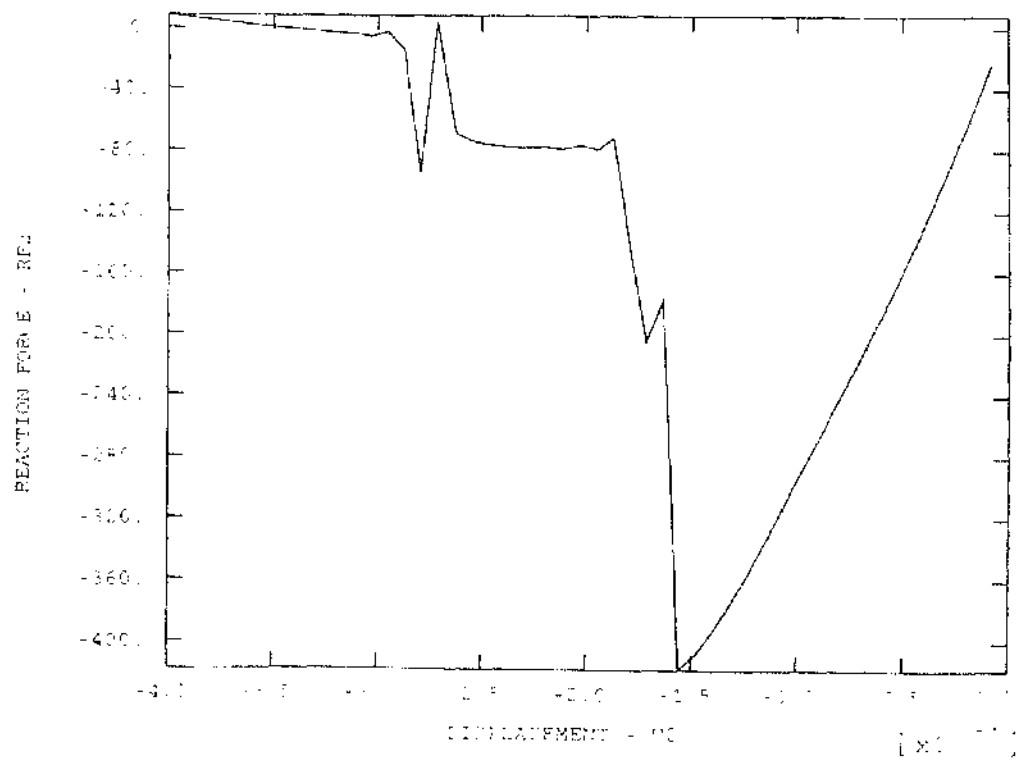


Fig 5.5 (b) Load-Deflection Curve of 79-Element Model

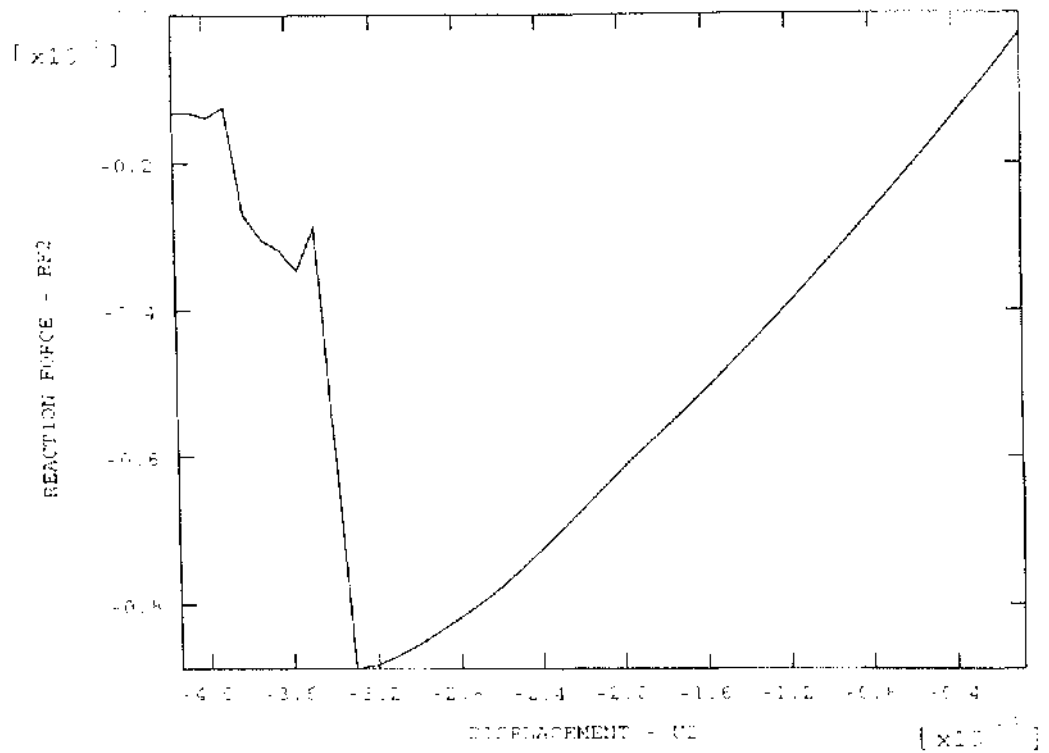


Fig 5.6 (a) Load-Deflection Curve of 79-Element Model with Damage Rate of 50

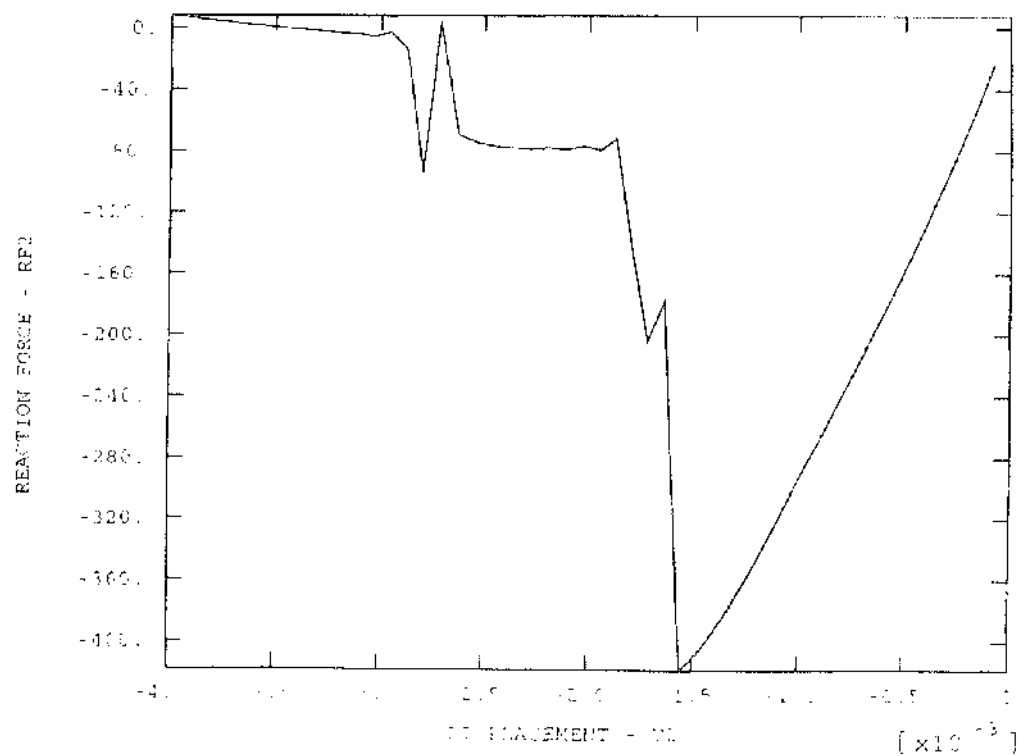


Fig 5.6 (b) Load-Deflection Curve of 79-Element Model with Damage Rate of 100

Test No.	Rate of damage	RF2 (N)	U2 (mm)	Fig No.
1	100	410	2.2	5.7 (a)
2	150	300	1.3	5.7 (b)
3	200	220	1.0	5.7 (c)

Table 5.4 Damage rate from 100 to 200

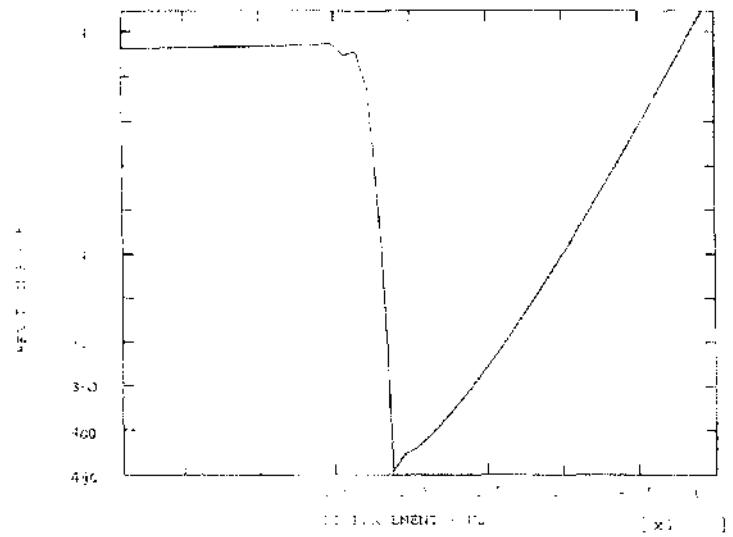


Fig 5.7 (a) Load-Deflection Curve of 26-Element Model with Damage Rate of 100

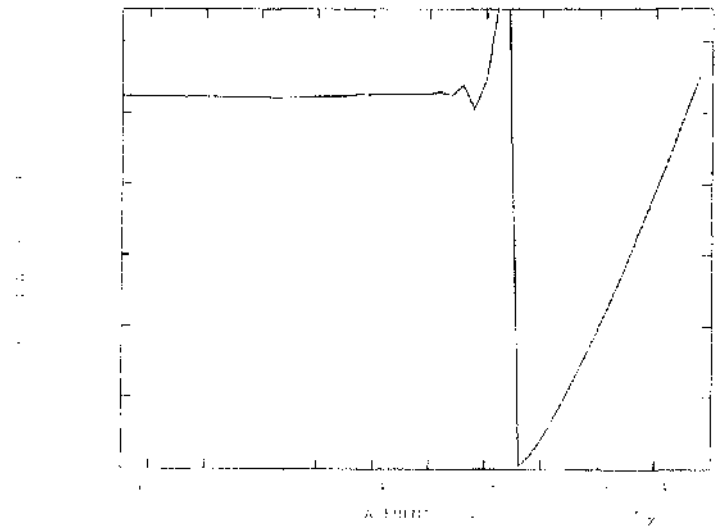


Fig 5.7 (b) Load-Deflection Curve of 26-Element Model with Damage Rate of 150

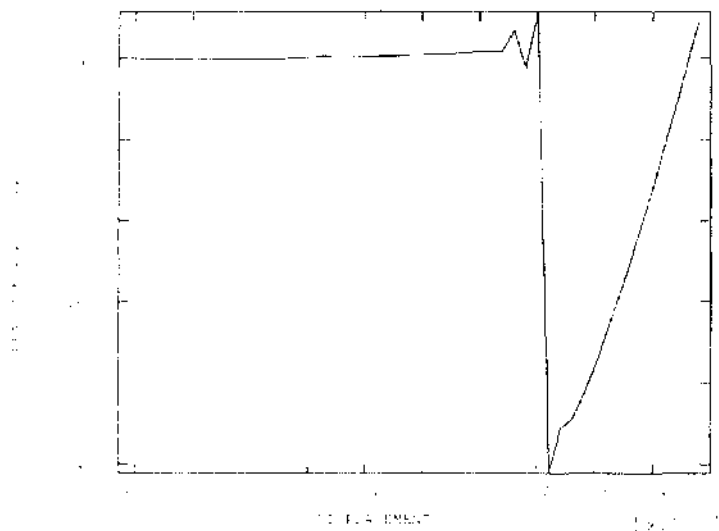


Fig 5.7 (c) Load-Deflection Curve of 26-Element Model with Damage Rate of 200

Fig 5.8 shows the comparison between the experimental and computational analysis.

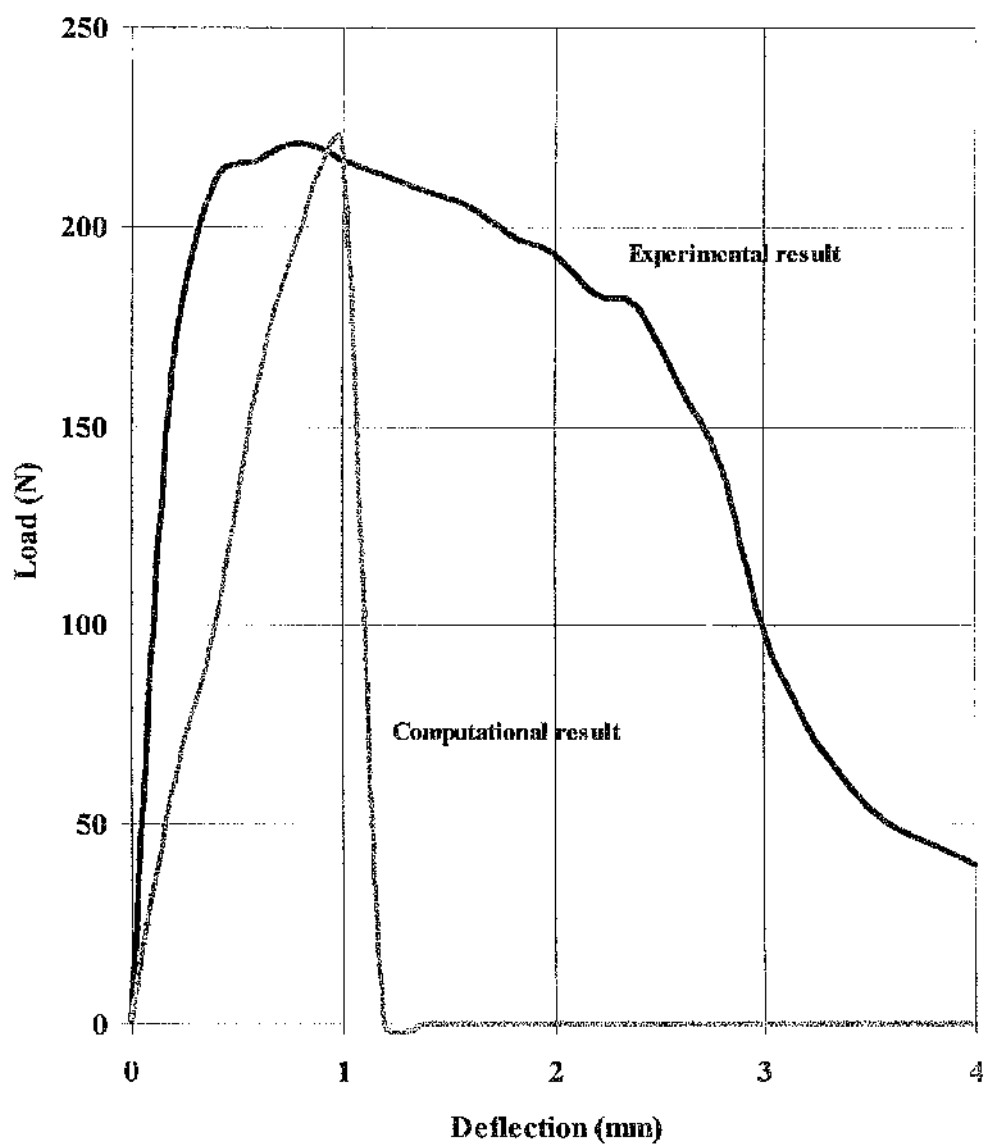


Fig 5.8 Comparison Between Computational & Experimental Results

5.4 Conclusions

As noted previously, there are clearly features of the Abaqus/Explicit solution algorithm which were not well understood but which are beyond the scope of the current work. However an understanding of these is required if future work is to progress and so some pointers might be usefully laid here.

“Deformation speed” is defined as the rate at which deformation occurs under loading and is expressed as the strain rate (ϵ / sec). For a given total strain there is a relation between strain rate and the duration of the straining process (Macaulay, 1987). Thus, high strain rates generally occur over short periods of time and vice versa.

“Wave speed” is defined as the finite rate of wave propagation through a deforming material. However one of the two limiting conditions is normally assumed in stress analysis. In the first of these, the finite rate of wave propagation is simply ignored and deformations are assumed to occur simultaneously throughout the material. In reality for a homogenous isotropic and linear elastic solid, a wave of deformation travels at constant speed which depends on the stiffness and density of the material and the type of deformation involved. The elastic wave speed C is also the speed of sound and given by:

$$C = \sqrt{\frac{E}{\rho}}$$

Typical values of C for some engineering materials are given in Table 5.5.

	Steel	Aluminium	Cast Iron	Lead	Dupont Lanxide	Glass
Tensile & Compressive						
$C = \sqrt{\frac{E}{\rho}}$	5000	5000	3900	1200	6940	5250
Shear						
$C = \sqrt{\frac{G}{\rho}}$	3200	3050	2450	700	4250	3200

Table 5.5 Elastic wave speeds (m/s)

Now there are several ways to increase the wave speed, some of which are not available in physical as opposed to computational experiments, so that the ratio between the deformation speed and wave speed does not exceed 1.0. These include:

1. increasing the elastic modulus
2. decreasing the density
3. decreasing the total time step in the Abaqus solution.

Suggestion (1) would alter even the static material properties and so is not available except in a purely kinematic analysis where stress recovery is not important. Suggestion (2) may give acceptable results for a quasi-static analysis where inertia effects are not important. Suggestion (3) would alter the displacement of the specimen. Therefore, none of these schemes seems inappropriate for the analysis of stabbing.

In T-section analysis was also limited by problems caused by excessive distortion of small elements. This could be avoided using the 26 element mesh.

Although the maximum loading results obtained from the this computational experiment were quite accurate (2% difference compared to Gibson), Fig 5.7 shows that the maximum load in Gibson's case was 220N at a displacement of 0.7mm. A better finite element analysis for the T-section might require a graduated ("biased") mesh size of at least 200 elements with a smooth transition of sizes to admit a smooth stress distribution. One might resort to manual deletion of the elements in highly stressed regions at each step increment but this option is only available in Abaqus/Standard. In spite of all attempts then, and even after considerable discussion through the FE community on the web, no solution was found for the excessive wave speed and element distortion problems.

The Constitutive Modelling Of Bone

6.1 Introduction

Bone is a complex material or, more correctly, it is a composite of what are individually complex materials. It plays an important role in the support and movement of the body, provides protection for vital organs, a mineral reservoir for storing calcium and phosphorus, and is the host for blood cell formation. However, despite its complexity, bone can be categorised either on the basis of its microstructure or its macrostructure.

The microstructure of bone may be classified as woven, lamellar or haversian. Compact (cortical) and cancellous (trabecular) bone are the two main macrostructural classifications. Measures of the physical properties of the tissue may differ in vivo and in vitro and many such measures contribute to the overall mechanical properties of bone. Age also affects the properties of bone, largely through changes in mineralisation and water content each of which can influence the stiffness modulus and the strength of the material (Abendschein and Hyatt (1970), Katz et al.(1984) and Currey (1969)).

Structurally, there are four types of bone, each named historically after their shapes and sizes. They are:

- long bones (e.g femur)
- short bones (e.g phalanx)
- flat bones (scapula)
- irregular bones (vertebra).

Most research has been based on long bones, especially the compact and trabecular bone found in femur, largely due their distinctly uniform cylindrical shape and thickness (Sedlin (1966), Cowin (1979), Bonfield (1980), Hogan (1988) etc.) Nevertheless, in this study, attention is focused on the ribs as much as the femurs since, in most knife attack incidents, stab wounds occur to the upper abdominal area. In some instances, the force of impact is so strong that it fractures all of the victims' ribs.

These simulations of the impact of a knife blade on various type of bone were carried out on a drop tower. There is no standardisation for such stabbing simulation and so the drop tower impact tests were supported by quasi-static 3-point bend tests to determine basic mechanical properties.

6.2 Macrostructure Of Bone

There are two major forms of bone tissues found in the macrostructure of bone:

- compact bone and
- trabecular bone.

These are illustrated in Fig 6.1.

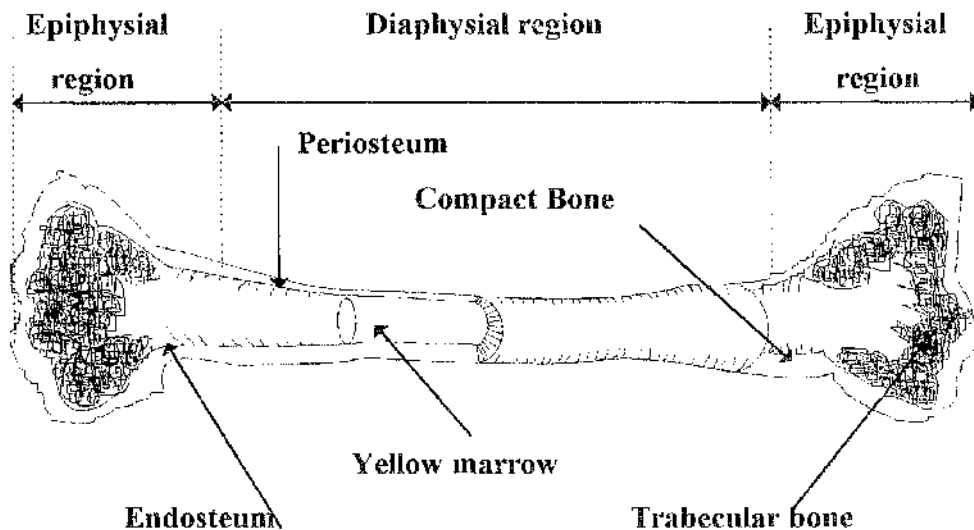


Fig 6.1 Longitudinal section of femur

The external surface of a bone is made of a dense white fibrous membrane called periosteum while the internal surface is called endosteum. The latter consists of a thin epithelial membrane. The ends of the bone have a spongy appearance and are filled with needlelike bony spicules called trabeculae, hence the adjective “trabecular”. The bony spicules tend to be arranged along lines of maximum stress and their orientation will therefore differ between individual bones according to the nature and magnitude of the applied load. This feature greatly enhances a bone’s performance under normal loading. Compact bone is primarily found in the diaphysis of long bones and is much denser than the trabecular bone.

In the medullary cavities of long bones are filled with a soft, diffuse connective tissue called marrow. It serves as a site for producing blood cells. During infancy, the colour of the marrow is red as it is engaged in the production of red blood cells. As an individual ages, the red marrow is gradually replaced by yellow marrow. This is because the marrow cells become saturated with fat and as a result, become inactive in blood cell production.

6.3 Compact Bone

6.3.1 Biological Structure

Compact bone (Fig 6.2) contains many cylindrical-shaped structural units called osteons, or haversian systems. Each osteon surrounds a canal that runs lengthwise through the bone. Living bone cells in these units are literally cemented together to constitute the structural framework of compact bone. Four types of structures make up each osteon:

1. Lamellae: concentric, cylinder-shaped layers of calcified matrix.
2. Lacunae: small spaces containing tissue fluid in which bone cells lie imprisoned between the hard layers of the lamellae.
3. Canaliculi: ultra-small canals radiating in all directions from the lacunae and connecting them to each other and into larger canal, the haversian canal.
4. Haversian canal: extends lengthwise through the centre of each haversian system, containing blood vessels, lymphatic vessels, and nerves from the haversian canal. Lengthwise running haversian canals are connected to each other by transverse Volkmann's canal. These communicating canals contain nerves and vessels that carry blood and lymph from the exterior surface of the bone to the osteons.

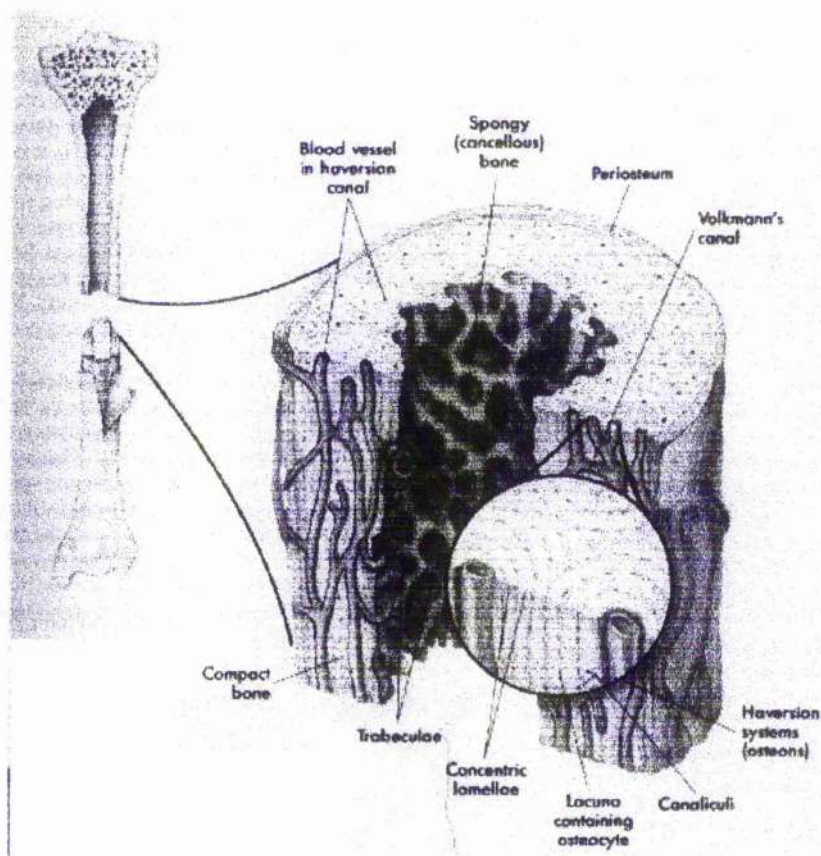


Fig 6.2 Microscopic Of Bone (insert from Anatomy & Physiology)

6.3.2 Mechanical Structure

In mechanical terms, bone can be classified as a composite material. It is made up of connective tissues that consists of cells, fibres and extracellular material. The extracellular material or collagenous matrix is the major organic component which is a composite of collagenous fibers and an mixture of protein and polysaccharides. These components not only add to overall strength but also give bone some degree of plastic-like resilience so that applied stress, within reasonable limits, does not result in frequent crush or fracture injuries.

The extracellular matrix is impregnated with a mineral phase, consisting of chemical crystals of calcium and phosphate, hydroxyapatite ($\text{Ca}_{10}(\text{PO}_4)_6(\text{OH}_2)$).

The needlelike apatite crystals are orientated in the organic matrix of the bone so that they can most effectively resist stress and mechanical deformation. However, the crystals themselves are brittle with little resistance to impact. As a connective tissue, bone is ideally suited to its functions, and the concept that the structure and function are interrelated is apparent in this highly specialised tissue.

The structural components of bone material are organised and interrelated to give maximal strength and minimal weight result, with the orientations of the apatite needles, collagen fibres, lamellae, Haversian systems and blood vessels being along the length of the long bone to best resist the applied service loading. This results in a highly efficient but anisotropic material.

Bone is also a visco-elastic material. This is not usually important because, except in extremis, it is not a function of bone to store or gradually dissipate energy. Nevertheless, it may be important under severe impact, since the modulus of elasticity and the fracture stress are both quite strongly strain-rate dependent (McElheney, 1966). Such effects are ignored in the present work.

6.4 Preparation Of Bone Specimen

Two distinct types of bone tissue were tested, compact bone and ribs. Compact femoral bone was subjected to three-point bending so that the properties of this almost monolithic ceramic could be determined. This is expected to shatter upon excessive loading, making contact with the experiments on engineering monolithic ceramics described in chapter 2.

The ribs were used for impact tests in order to examine the response of whole bone which is expected to be much more resistant to impact, making contact with the experiments on polymers and the computational work on ceramic composite described in chapter 2 and 3.

6.4.1 Compact Bone

The compact bone specimens were obtained from bovine femoral shaft tissue, fresh from the abattoir. The age and sex of the animal were not known but typically animals are slaughtered at about two years of age. The specimens were cleaned of attached muscle tissue and the epiphysial region was sawn away, to leave only the diaphysial region. This was further cut into two sections at middiaphysis and the marrow removed.

Three-point bend specimens were machined, from femoral sections with the fibre axis laying parallel with the length of the specimen (Fig 6.3), into slabs of 125 x 25 x 3mm (Fig 6.4). Only two slabs could usually be obtained from each section of bone, but this depends on the individual geometry. Sedlin and Hirsch (1966) recommended that specimens should be moistened with isotonic Ringer's solution and stored in a sealed bags at -20°C to prevent the mechanical properties of the bone changing significantly. This recommendation was not followed here because one of the concerns of these tests is to determine the extreme characteristics of dry and wet bone, following Curry (1970), who has performed similar research and noted that the properties may be distinctly different between the dry/drying and wet states.

"Dry" bone specimens were thus left to air dry at a room temperature of 20°C for a week to allow ample time for the moisture content to stabilise by evaporation. The weight of the specimens reduces linearly with time during this period and thereafter remains almost constant. This simple method of preparing dry specimens allows uniform mechanical properties to be achieved and obtained from the **SAME** femur.

"Wet" bone specimens were prepared by submerging them in water for 24 hours prior to testing.

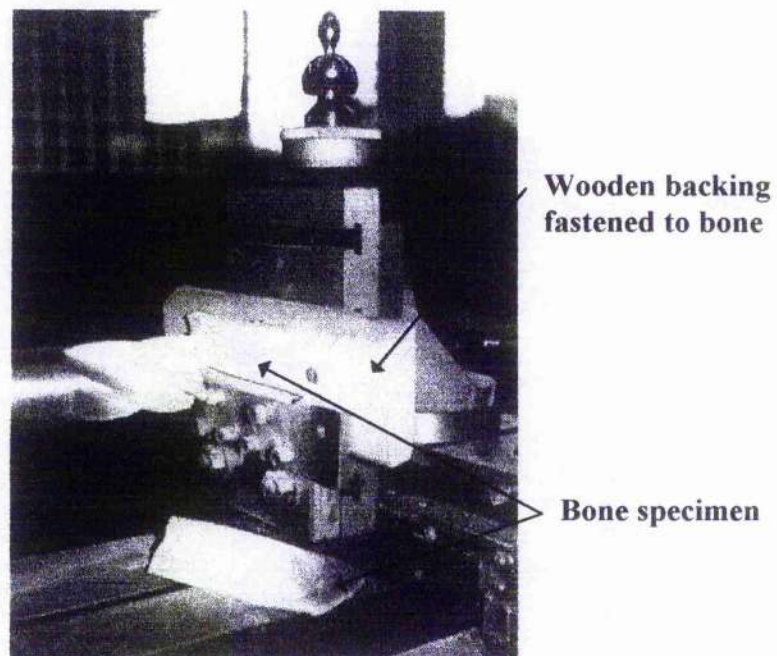


Fig 6.3 Machining of bone specimen

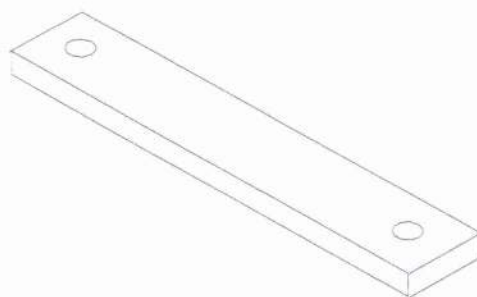


Fig 6.4 Bone specimen, 125 x 25 x 3mm

6.4.2 Ribs

Whole rib specimens were prepared differently from compact bone. These were obtained from pigs and, once detached from all muscles, were moistened with saline and stored in a freezer at -5°C , following Jackson's (1992) recommendation, until they were required for 3-point bend or impact testing. Burstein, et al (1972) showed that keeping the specimen wet with saline drip can enhance the mechanical properties beyond the "fresh-but-dead" values but retaining the moisture content in ribs was considered an important aspect of the simulation of human ribs in vivo.

6.4.3 Conclusions On Specimen Selection And Preparation

Bone, like other ceramics, are stiff and relatively brittle materials which make them difficult to machine into required test-pieces. On the other hand, the biological features of bone pose specific problems in the evaluation of mechanical properties. Hence, the preparation of the bone specimen plays an important role in contributing to the accuracy and reliability of the test results.

There are basically four major factors to consider before preparing the specimen in order to prevent wrong interpretation of results. These are:

- the position of the specimen cut from the whole bone
- the orientation of the specimen, in particular of the microstructural components
- the size of the specimen
- the shape of the specimen

The position of the specimen to be taken need to be exact. For example, if the specimen is extracted from between the epiphysial and diaphysial region from a femur, it would contain a mixed matrix composite of trabecular and compact bone.

Pope and Outwater (1974) have also found that the strength in the axial direction is a maximum at the middiaphysis of a long bone and decreases towards the ends of the bone.

The orientation of the specimen to be cut also affects the material properties. Bone is anisotropic (Currey (1964) and Mack (1964)). The orientation can be confirmed from the observation that the apatite needles, collagen fibres, lamellae, Haversian systems and blood vessels are laid out along the length of the long bone. The advantage of this anisotropic composite material to the animal is that it can be arranged such that the strongest direction lies in the direction of greatest loading. The material is then much stronger and stiffer than an isotropic material of the same average composition.

For 3-point bending tests and cyclic loading tests, the specimen was prepared with the fibres oriented parallel to the long edge. Although the material properties of a homogeneous continuum are theoretically independent of specimen dimensions, with biological materials this is seldom true in practice, at moderate size scales. A minimum specimen size is therefore required to ensure homogeneity. Furthermore, if the span to depth ratio of a beam is small, shear deformation would be significant and nullify the analysis of a simple 3-point bending experiment. The type of test envisaged also determines the shape of the specimen to be fabricated, with dumb-bell specimens for tensile testing and slabs for bending tests.

While preparing such brittle specimens for machining, the material must be clamped with a wooden block to minimise splinter damage. Saline (never oil) may be usefully sprayed on specimen during machining to prevent overheating. A face mask should be worn at all times during the fabrication process to prevent inhaling of dust particles or an unpleasant burnt smell which may be a long-term health hazard. Additional precautions may become necessary in the face of concern over BSE / CJD infection.

6.5 Experiments On Compact Bone

6.5.1 Monotonic Loading

Prior to testing, the “dry” specimens were allowed to dehydrate for a week while the “wet” specimens were submerged in water for 24 hr. Testing of the specimens was performed in three-point bending using a JJ Llyod LR30K Universal testing machine. A loading jig was specially designed and fabricated to provide high accuracy. The load and deformation of the tests was constantly monitored using an on-line computer and closed loop control.

The averaged density of the dry bone was found to be 1740 kg/m^3 while the wet bone was found to be 1938 kg/m^3 . Poisson's ratio was not calculated but Piekarski (1968) and McElhaney (1966), suggest that this is between 0.13 and 0.3 - a larger than ideal range. Here it is assumed that Poisson's ratio is 0.28 for dry bone and 0.3 for wet bone. During three- point bend tests, the specimen was supported on a span of 70mm and the load applied perpendicular to the longitudinal axis at midspan. All the specimens were loaded to failure at a rate of 0.5mm/sec. Fig 6.5 shows the loading system.

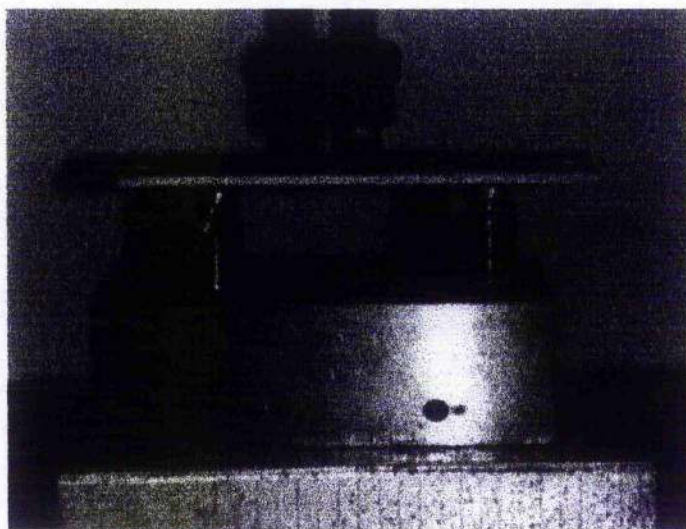


Fig 6.5 Three-point bending on bone

6.5.1.1 Results And Discussions

Dry Bone

A load-deflection curve for dry bone specimen is shown in Figure 6.6.:

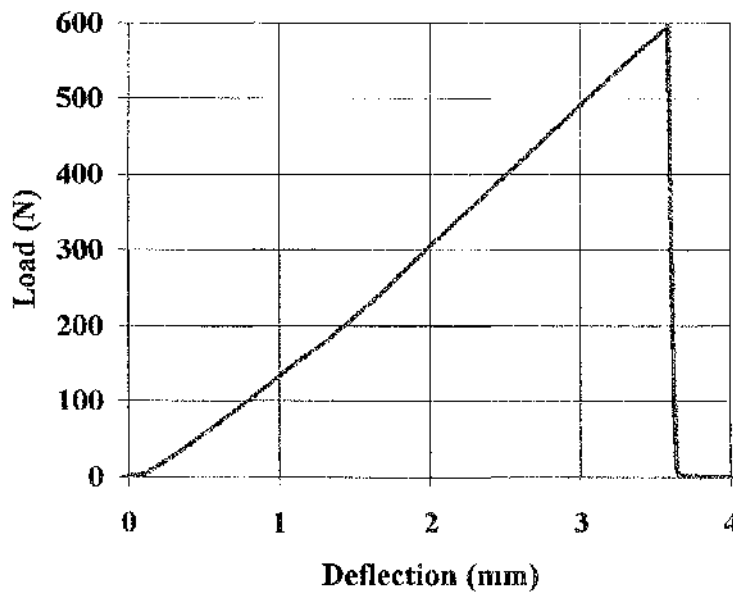


Fig 6.6 Load-deflection curve of dry bone

For a preliminary test to determine the approximate load to cause fracture, the maximum extension of the pushrod was preset to 2 mm with a load limit of 400N. It was found however that even the dry bone was much tougher than expected. Hence, the maximum extension of the pushrod was increased to 8 mm with a load limit of 1000N. From Fig 6.6, it is apparent that the loading curve is almost linear up to the maximum force of 597N and extension of 3.7mm. At this point, the specimen failed with a loud bang, fracturing at the support and load points almost simultaneously. The fracture surfaces were typically brittle with very little sign of plastic flow to give toughness to the material.

This is in contrast to the behaviour of inorganic composites such as glass fibre reinforced plastic which show some toughness as a result of the difficulty in initiating a macrocrack.

Such difficulty might also be expected in bone but this particular specimen is a segment from a whole bone and more akin to the monolithic engineering ceramics tested previously. The behaviour of whole bone will be addressed shortly.

On the basis of simple bending theory, which is reasonable for the aspect ratio of this specimen, the elastic modulus was calculated to be 23 GPa and the ultimate bending stress 279MPa.

Wet Bone

The load-deflection curve of the wet bone is as shown in Figure 6.7.

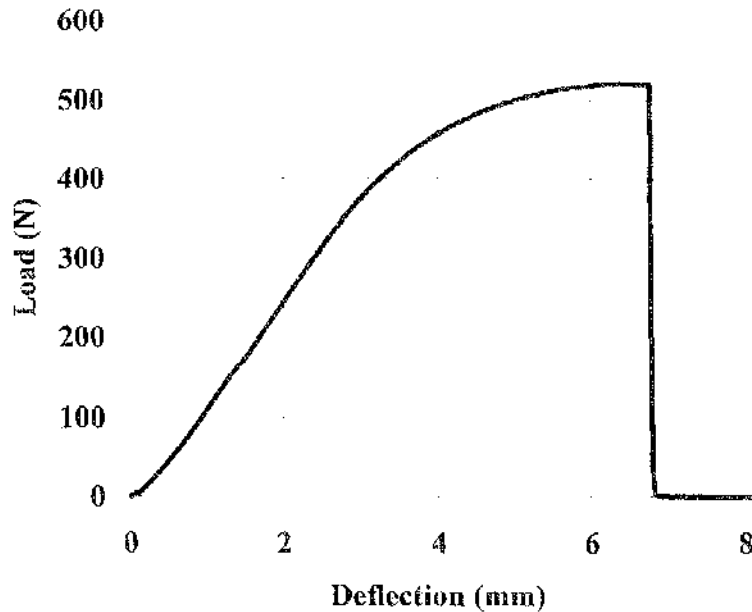


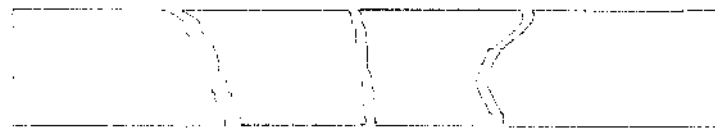
Fig 6.7 Load-deflection curve of wet bone

Fig 6.7 shows the specimen response to be almost linear up to 320N and nonlinear from then until failure at a load of 520N and central deflection of 6.8mm. The elastic modulus was calculated as 15 GPa for the linear elastic portion of the curve. It is not clear from this single test whether the material is nonlinear but perfectly elastic beyond the limit of proportionality or whether it is inelastic or damaging. Further experiments, to be discussed later, are needed to resolve this. In any case, the limit of proportionality occurs at a stress of 149 MPa.

Unlike the dry bone, the wet bone fractured in half at the loading point. Although the ultimate tensile stress is lower than in the dry condition, the wet specimen (more likely to be representative of the *in vivo* behaviour) shows what may be plastic, energy-absorbing behaviour. This would be reasonable for a biological material, most of which have properties which tend to preserve some structural integrity and load carrying capacity even if the material is loaded to near-fracture. In a composite like bone, with a fibrous matrix of low modulus material, such plastic deformation (which has yet to be established) may be due to plastic deformation of the collagen matrix or of the fibrous matrix (Currey, 1975). On the microstructural scale this may be due to delamination of the Haversian systems, laminae and lamellae from their neighbours, allowing the newly formed surfaces shear past each other. The comparison of the results of the dry and wet bone are tabulated in Table 6.1. The schematic view of the ruptured dry and wet bone were shown as in Fig 6.8.

	Elastic Modulus,	Poisson Ratio,	Maximum Loading	Maximum
	E (GPa)	ν	Force, (N)	Deflection, (mm)
Dry Bone	23 GPa	0.2	597	3.7
Wet Bone	15 GPa	0.3	520	6.8

Table 6.1 Comparison between dry and wet bone



(A) Dry bone



(B) Wet bone

Fig 6.8 Schematic view of the ruptured dry and wet bone

6.5.2 Cyclic Loading Test

Results from the monotonic loading tests have shown that dry bone deformed linear elastically to failure while the wet bone is materially nonlinear. It is not possible to determine, from a single monotonic loading response, whether this nonlinearity is due to nonlinear perfect elasticity or to inelastic behaviour or damaging plasticity. To make such distinction requires a cyclic loading/unloading test.

In microscopic terms, elastic deformation is defined as a process during which no new microdefects are nucleated while all existing microdefects, probably due to manufacturing process, without growing in size (Krajcinovic, 1995). However, if the applied load exceeds a particular threshold value, nucleation of new and growth of existing microdefects will influence the deformation. The damage due to a growing microdefect would accumulate progressively and result in the reduction of the elastic modulus. Since the response of wet bone shows features typically found in a damaging material, it was subjected to cyclic loading tests in order to determine any damage accumulation manifested through a progressive reduction of elastic modulus on each cycle, within a framework of Continuum Damage Mechanics.

Five cycles of loading/unloading were applied to a similar “wet” specimen to that used previously, again on the Lloyd LR30 testing machine. The rate of pushrod travel was 0.5mm/sec during both loading and unloading. The deflection was incrementally increased on each cycle until the last, in which it was loaded to failure.

6.5.2.1 Results And Discussions

The load-deflection curve of the cyclic loading is plotted in Figure 6.9:

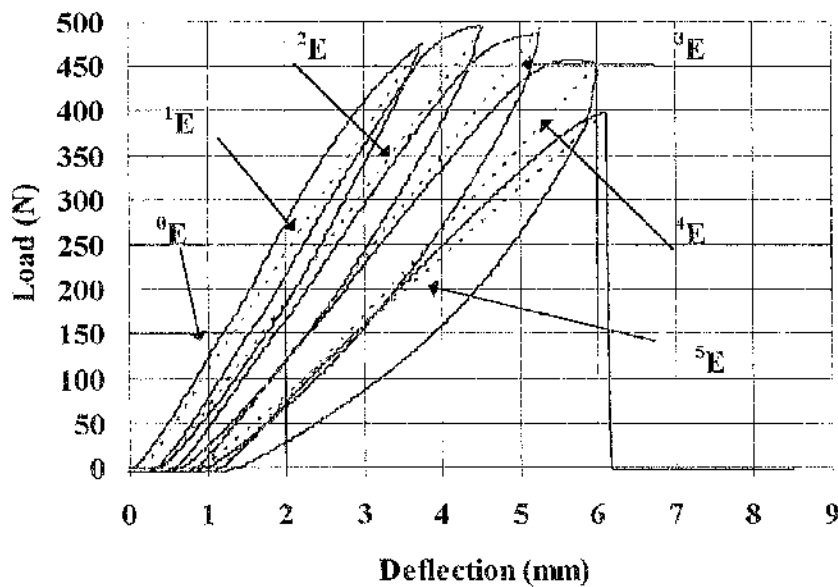


Fig 6.9 Cyclic loading of wet bone

This curve shows several interesting features.

Firstly, the material does not recover the total strain on unloading but shows an inelastic response which increases with each cycle. The wet bone is then proven to have some degree of plasticity-induced toughness, as one might hope.

This is however not as great as in, say, metals and initial constitutive modelling might usefully be done with the assumption that the material is simple elastic.

Figure 6.9 also clearly shows a progressive decay in the elastic modulus when the material is subjected to an increased cyclic loading. The existence of the hysteresis loops implies that the tangent modulus just prior to complete unloading in any cycle is less than the tangent modulus immediately after subsequent loading. This feature is also noted by Gibson (1995) for ceramic composite, further strengthening the constitutive similarities between the materials and justifying the initial use of this material to model bone. For simplicity however, the elastic modulus for each cycle was homogenised by assuming a linear elastic line between the unloaded and maximum load point on each cycle. This is shown as 1E , 2E , 3E etc. A total of 6 elastic moduli were calculated over the five cycles, including the undamaged elastic modulus 0E and in general:

$$^0E > ^1E > ^2E > ^3E > ^4E > ^5E$$

Now “damage” can be defined (Krajcinovic (1996)) as:

$$D = 1 - \frac{^1E}{^0E} \quad , \quad D_1 = 1 - \frac{^2E}{^0E} \quad \text{etc}$$

and with the initial elastic modulus calculated to be 17.8GPa (ie in the linear elastic stage when damage is equal to zero) then the damage evolution can be followed (Table 6.2).

		Deflection (mm)	Elastic Modulus (GPa)	Max. Bending Strength (MPa)	Damage Parameter
Cycle 1	Loading	3.75	16.6	218	0.07
	Unloading	0.00	-	-	-
Cycle 2	Loading	4.50	15.6	229	0.12
	Unloading	0.00	-	-	-
Cycle 3	Loading	5.25	13.7	225	0.23
	Unloading	0.00	-	-	-
Cycle 4	Loading	6.00	11	214	0.38
	Unloading	0.00	-	-	-
Cycle 5	Loading	6.20	9.9	182	0.44
	Unloading	-	-	-	-

Table 6.2 Cyclic loading of wet bone

The results obtained in Table 6.2 allow a damage-deflection curve to be plotted (Fig 6.10). The corresponding damage-strain relationship is more problematic since the neutral axis of the beam shifts during damage evolution. This shift in the neutral axis can be predicted for the case of a perfectly brittle damaging material using the equation developed by Krajcinovic. However this was not considered a useful exercise at this point.

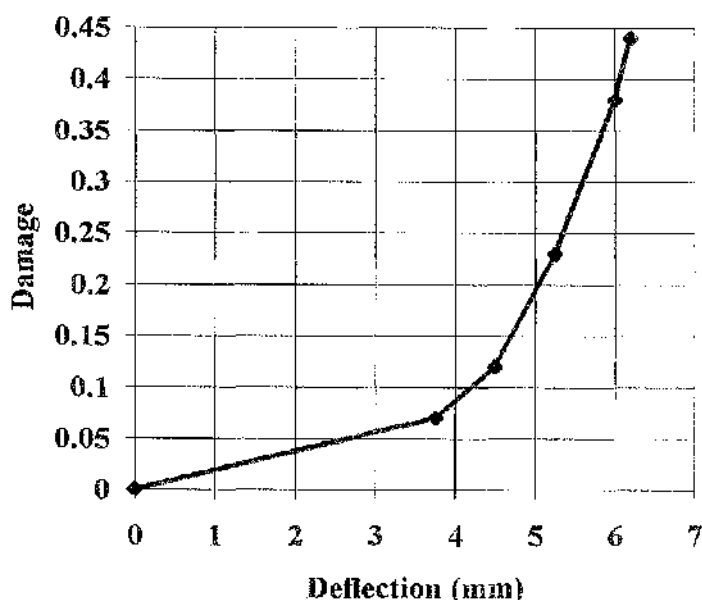


Fig 6.10 Deflection-damage curve

6.6 Experiments On Ribs

There are twelve pairs of ribs in a human. Together with the vertebral column and sternum, they form the bony cage known as thoracic cage or simply the thorax. Each rib lies approximately 2 cm apart from its neighbours and the whole thoracic cage serves as a protection for the vital organs within.

A detailed examination of 34 stabbing homicides was carried out by Ankensen (1996) using data from the Department of Forensic Medicine and Science at the University of Glasgow. Ankensen reported that 53% of the fatal wounds were chest wounds which penetrated the thoracic cage and puncturing underlying vital organs. Previous tests have shown that although compact bone is quite brittle, it still requires a relatively large stress to cause rupture. This does not seem to be the case with ribs. The key difference is that the ribs do not contain compact bone alone but instead seem to trade-off some mechanical strength in order to retain still further ductility than is available even to wet compact bone.

Three-point bending tests on whole ribs were carried out to find out the basic mechanical properties while the drop tower was used to measure the impact resistance of these whole bones.

6.6.1 Monotonic Loading

Curved pork ribs were procured and a reasonably straight gauge length of 100mm cut from the central section. The approximate asymmetric diameter was 15mm and the weight 20g. The volume of the specimen was then $4.5 \times 10^{-6} \text{ m}^3$ and the average density 1003 kg/m^3 . Poisson's ratio was assumed to be 0.3.

During 3-point bend tests, the specimen was supported on a span of 70mm and the load was applied perpendicular to the longitudinal axis at midspan. All the specimens were loaded to failure at a rate of 0.5mm/sec. Fig 6.11 shows the load applied to the bone specimen before taken to failure. Although the specimen was cut from as straight a segment of rib as was possible, it still retained some curvature. The outer curvature of the specimen was consistently placed facing the pushrod, since this is the orientation which better matches that of an actual stabbing attack.

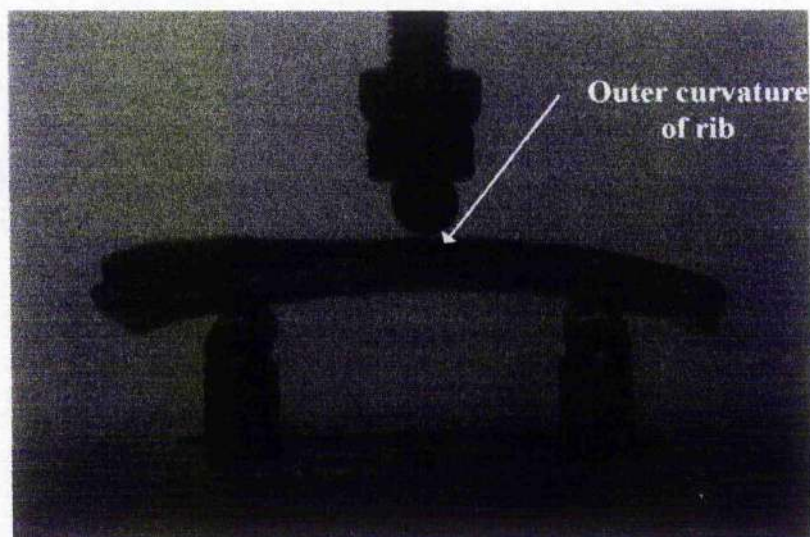


Fig 6.11 Three-point bending of rib specimen

6.6.1.1 Results And Discussions

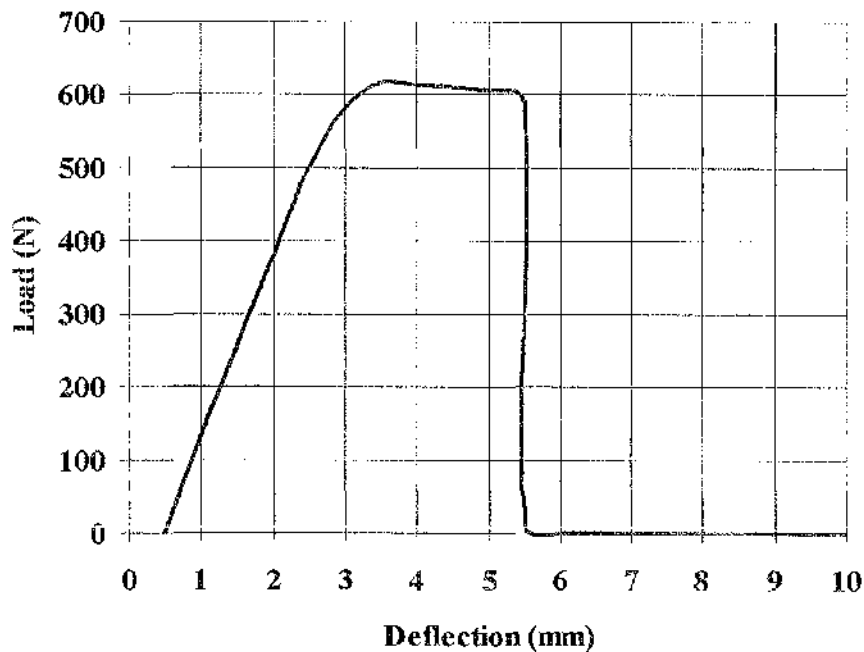


Fig 6.12 Load-deflection curve

A whole rib comprises a sheath of compact bone surrounding the marrow. In its natural state, the rib is not totally symmetric in cross-section but this departure from a circular cross-section is ignored for calculation purposes. The rib also has a slight non-uniform curvature which makes calculation of neutral axis awkward. This is also ignored.

From the load-deflection graph, it appears that the rib departs from linear elasticity at 480N. Yielding occurs beyond this point and the specimen reached a maximum loading force of 617N before rupture took place as in Fig 6.12. The elastic modulus of the rib was calculated to be 0.58 GPa.

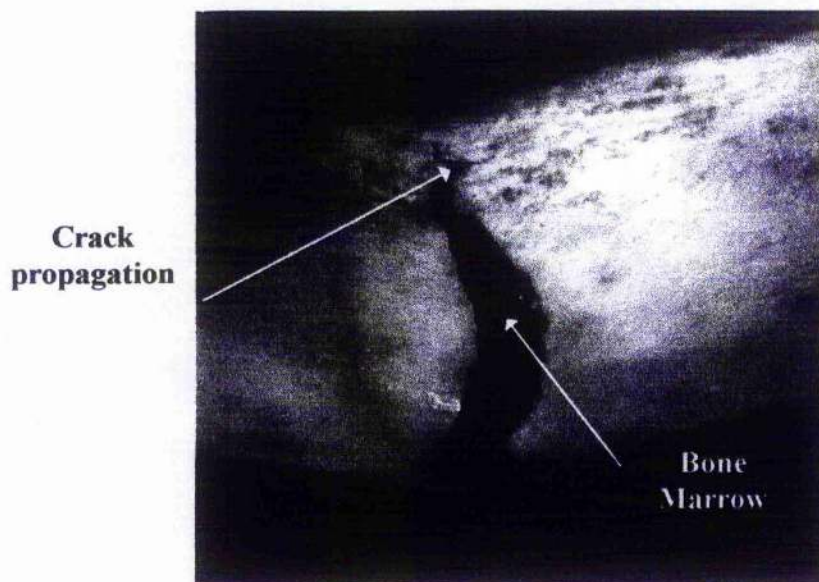


Fig 6.13 Rib loaded to 5.5mm

6.6.2 Cyclic Loading

To confirm that the nonlinearity in Fig 6.12 is due to damage evolution, a cyclic test was carried out. The specimen was supported at an outer span of 70mm and the load was applied perpendicular to the longitudinal axis at midspan. This time, to ensure stability within the supports when the loading is removed, the outer curvature was facing the base. The rate of loading/unloading of the pushrod was 0.5mm/sec. An increment of deflection was added to each cycle until the last cycle, in which the specimen was loaded to failure. 3 cycles were carried out on the rib specimen.

6.6.2.1 Results And Discussions

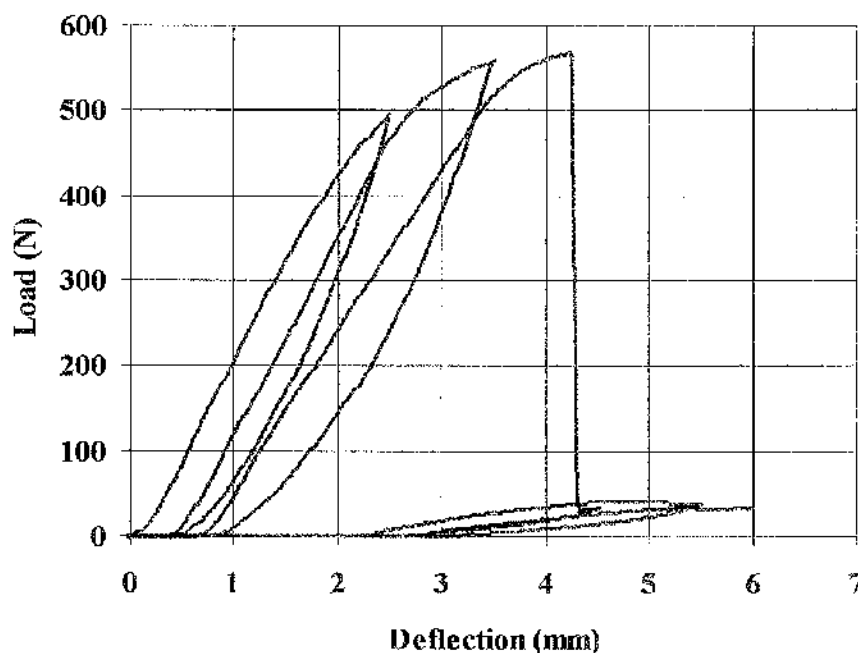


Fig 6.14 Cyclic loading test of rib

The maximum loading force of the rib is 550N at a deflection of 4.3mm (Fig 6.14). This is less than that under monotonic loading, perhaps as a result of the orientation of the specimen on the loading jig. Having the outer curvature upwards may well give some initial deformation stiffening, particularly if there is friction at the support points. The elastic modulus of the rib was calculated to be 0.61GPa.

6.6.3 Impact Test

The ultimate experimental aim of the project was to determine the resistance of whole bone to impact with a sharp object. This was done so using the drop tower. The total mass of the crosshead assembly was 4.1kg and the blade profile used was a type 3A, ie a pointed blade with blunt edges. This was chosen to give a rectangular incision whose length could be readily measured. The specimens averaged 10 cm in length and were supported by a Roma Plastilina backing. This simulates the supportive effect of underlying tissue and reduces the bending moment and hence the likelihood of bending failure. Indeed, it has been argued (Ankersen et al (1996)) that Roma Plastilina is too supportive in this respect but this material is specified by the Home Office for similar tests.

The kinetic energies and velocities at impact were determined using the high speed video camera as described in Chapter 2. In this test, the damage was measured as the length of incision caused by dropping the crosshead from different heights. The averaged damage measure is as shown in Table 6.3.

Height (m)	Rib 1	Rib 2	Rib 3	Rib 4	Rib 5	Rib 6	Average Damage (mm)
0.05	4	6	7	7	4	9	6.2
0.10	9	11	10	10	8	12	10
0.15	10	11	11	11	10	13	11
0.20	10	13	12	12	11	14	12
0.25	11	13	15	15	11	Fail	13
0.30	Fail	Fail	Fail	Fail	Fail	Fail	-

Table 6.3 Average damage measure

Again as in Chapter 2, the velocities and kinetic energies of the rib specimens were calculated, as shown in Table 6.4.

Drop Height (mm)	Averaged Damage (mm)	Velocity (m/s)	Kinetic Energy (J)	Momentum (Ns)
50	6.2	0.65	1	2.7
100	10	1.1	2.5	4.5
150	11	1.45	4.3	6
200	12	1.6	5.2	6.6
250	13	1.75	6.3	7.2

Table 6.4

The minimum drop height required to penetrate the rib is 0.01m. This gave an average damage length of 6mm. Additional tests can be made further along the longitudinal axis of the same specimen since there is no visible damage remote from the immediate area of penetration. This is a feature of whole bone as opposed to compact bone but is shown by the similar drop tests on tough polymer. This justified the use of such a material to mimic real whole bone.

The maximum drop-height that the rib can tolerate without total failure is 30cm. Beyond this height, a long crack would propagate along the fibre axis. A damage-kinetic energy graph, based on the results from Table 6.4, is given in Figure 6.15 while Fig 6.16 shows images of the knife impact on ribs. The damage incurred by different drop heights shows considerable variation in results. The curve is nonlinear but might be well represent as bilinear, with a knee at about 50J.

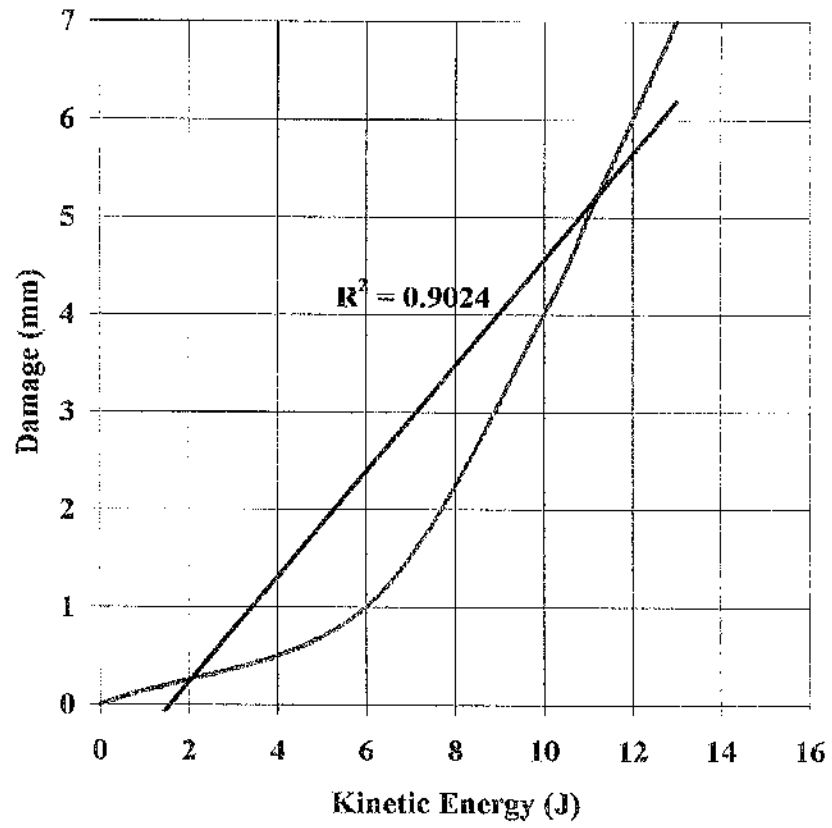


Fig 6.15 Damage-Kinetic Energy Curve

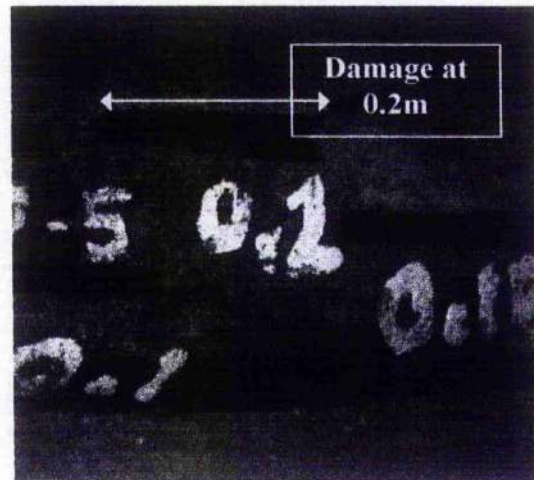
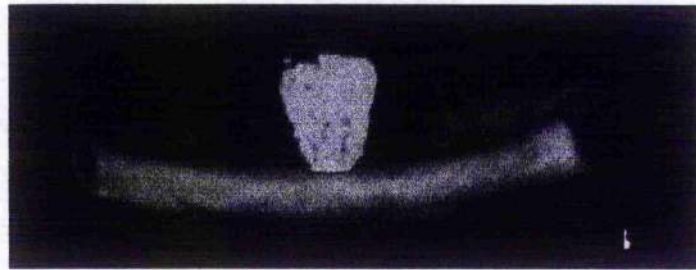
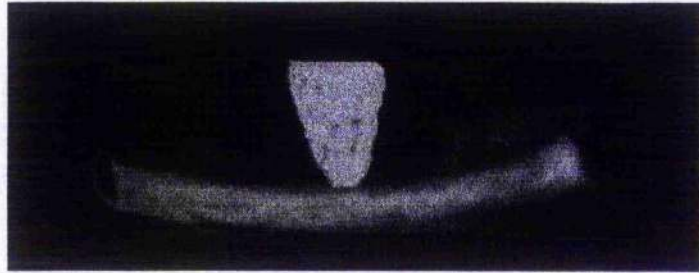
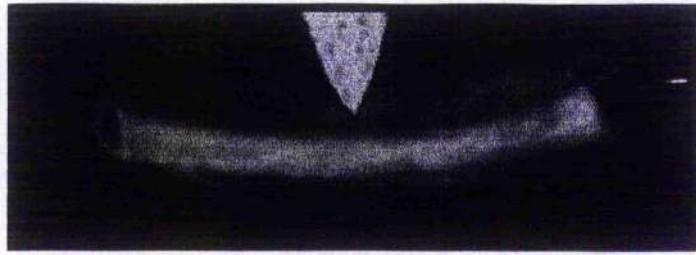


Fig 6.16 Measurement Of Damage

6.7 Conclusions

Bone can be classified as a composite material made up of collagenous fibres and a mixture of protein and polysaccharides. However, hydration and age play an important role in the mechanical properties. Therefore, extreme care has to be taken when preparing the bone specimens.

Three-point bend has been carried on dry and wet compact bone as well as ribs to determine the material properties. The ultimate tensile stress of the "wet" bone is lower than in the dry condition, but demonstrates a plastic, energy-absorbing behaviour. This behaviour is important for its biological function in human bone as it reduces the risk of fracture via overloading. Currey (1975) has suggested that bone fracture involves the delamination of Haversian systems, laminae and lamellae which then shear past each other. Thus, leaving one or more cracks oriented at right angles to the internal faults and surfaces, and then travelled very quickly and producing a brittle fracture.

The impact tests on ribs have shown that a minimal kinetic energy of 1J or momentum of 2.7Ns at 0.65m/s, could cause a damage slit of 50mm. However, in an actual assault, the resistance of skin and clothing have to be taken into consideration. The profile of the knife blade would also affect the penetration force (Ankersen et al ,1996).

Although extensive experimental results have been gathered, computation modelling of the impact test was less successful due to the problems with Abaqus software.

FINAL CONCLUSIONS

The purpose of this research was to quantify the forces involved in the infliction of particular wounds. This will contribute vital information to forensic pathologists and to the Court. Previous research has concentrated on skin since it provides the initial resistance against sharp objects. However, in most instances, further resistance is provided when the knife fractures ribs or other bone.

Since bone is a very complex material, it was prudent to study the impact response of model materials with more consistent engineering properties. The ultimate aim of the current work was to computationally and experimentally model the impact of a sharp object on a near-brittle material. Hence, a number of model materials were proposed including domestic ceramics, machinable ceramic and alumina. The experiments were carried out on a drop tower, which was calibrated to provide a velocity in relation to drop height. It was found that domestic tiles were easily fractured under very modest impact but the energy required to cause fracture was too low to admit any quantitative analysis. Therefore, domestic tile is unsuitable as a model material for bone. Machinable ceramic and alumina show higher impact energies at 3.44J and 26J respectively. These materials can be compared with bone specimens and can be correlated with computational analysis.

The Home office PSDB has conducted impact tests with a gas-gun which is not in the author's opinion a good simulation for knife incidents. This is because many knife attacks involve relatively low kinetic energy but high momentum. It is also of concern whether kinetic energy alone is a good measure of the impact resistance of target materials. The drop tower provides a good means of investigating the controversy between the relationship of kinetic energy and momentum.

Ceramic model materials show either minimal damage or complete failure upon impact, hence polymer (PVC) coupons were used instead. The ductility of the polymer and the brittleness of the ceramic bracket the behaviour of a real bone.

The impact tests of the polymers show that damage increases with kinetic energy. However, there is a slight increase in damage with momentum even if impact energy is constant. Therefore, more tests should be carried out, at higher energies to investigate this phenomenon. A 3-D plot of Damage vs KE vs Momentum is the key result to be generated.

Experiments have been carried out to determine a model material for bone but a computational model also needs to be developed. Bone is not completely brittle but retains a degree of toughness. An appropriate tool for modelling this is continuum damage mechanics which has evolved as a means of analysing diffuse microcracking in ceramic materials. This models the material degradation (damage) as a reduction of the stiffness and strength of the loaded material. Data on damage propagation in a toughened ceramic by three-point bending (Dupont Lanthide composite) has been previously published and hence, computational constitutive relations were generated and compared with the experimental results.

A simple method of modelling damage propagation computationally is to manually delete elements in which the stress exceeds the known capacity of the material, in this case the matrix microcracking stress. The model specimen was subjected to an increasing quasi-static displacement load using the Abaqus/Standard finite element system. This was then reanalysed and any additional elements which failed as a result of the redistribution arising from the previous element deletion were also removed.

This simple method of modelling damage propagation proved to be a technical success and provides benchmark deformation for future work. However, a constitutive model of the damage propagation which automatically allows the degradation of the elastic modulus is preferred.

Abaqus/Explicit, specifically designed to analyse contact and impact problems were adopted to build this constitutive model.

A 4-noded (2-D) bilinear plane strain element was generated simulating three-point bending on bend bar. A Fortran 90 subroutine shell, VUMAT, provided within the Abaqus/Explicit package was used to model the non-linear response of the material damage. Since bone is neither purely brittle nor purely elastic, a suitable damage law has to be derived. This was done by curve fitting with the experimental results. In order to achieve an ideal curve, the mesh size, damage coefficient and the matrix microcracking stress in the VUMAT subroutine programme were adjusted. A coarse mesh results in a stiffer result, as does a low damage coefficient. However, in this current research, the mesh size was kept small to save computational costs. Comparison of the computational and experimental models shows good agreement. However, the strain softening part of the loading history is not well represented in the computation, probably due to the failure of the model to allow load redistribution rather than element erosion.

Attention was later switched to the modelling of a T-section under three-point bending. This is geometrically more complex than the bend bar. The objectives of this analysis was to apply the stress-strain and load-deflection behaviour, based on the same principles of the Continuum Damage Mechanics, but in more than one direction. However, problems arose with excessive stress wave speed when there was an increase in mesh size. Attempts were made to either increase the elastic modulus, decrease the density or decrease the total time step in the Abaqus solution but unfortunately, none of these attempts was a success.

The only model which could be used was a very coarse mesh, which is rather inaccurate. The explicit finite solver also had problems in the computational analysis of complex geometric models.

Experimentally, bone was shown to be a very complex composite whose properties vary with the water and mineral content. Therefore, care has to be taken during the preparation of the specimens. "Dry" and "wet" bones were tested on the three-point bending. It was found that although "wet" bone has a lower ultimate strength compared to "dry" bone, it exhibits a more plastic, energy-absorbing behaviour. The energy required to penetrate a whole rib was found to be 1J. However, although extensive experimental data have been gathered, the computational model of the impact test was less successful largely due to the problems with the finite element software.

REFERENCES

ABAQUS EXPLICIT USER MANUAL VERSION 5.5
Hibbitt, Karlsson & Sorensen, Inc.

ABAQUS POST USER MANUAL, VERSION 5.5
Hibbitt, Karlsson & Sorensen, Inc.

ABAQUS STANDARD USER MANUAL, VERSION 5.5
Hibbitt, Karlsson & Sorensen, Inc.

ABENDSCHEIN W., HYATT G.W. (1970). Ultrasonics and selected physical properties of bone. *Clin. Orthop.*, 69, pp. 294-301

ANKERSEN J., BIRKBECK A., THOMSON R. (1996). Computational modelling of penetration of biomaterials. *Proceedings of the third international confer. On modern practise in stress and vibration analysis*, pp. 347-354

ASHBY M.F., JONES D. (1991). Engineering materials 1. *Pergamon Press, Oxford*

BEHIRI J.C., BONFIELD W. (1980). Crack velocity dependence of longitudinal fracture in bone. *J. Materials Science* 15, pp. 1841-1849

BURSTEIN A.H. et al. (1973). Failure characteristics of bone and bone tissue. *Perspectives In Biomedical Engineering*, edited by Kenedi R.M, University Park Press, pp. 1-4

CALVANO N.J. (1993). A study to determine the most important parameters for evaluating the resistance of soft body armour to penetration by edged weapons. *National Institute of Justice, Washington*

COWIN S.C. (1979). The strength anisotropy of bone. *ASME Applied Mechanics Division*, pp. 183-186

COWIN S.C. (1983). The mechanical and stress adaptive properties of bone. *Annals. Biomedical Engineering*, Vol.11, pp. 263-295

CURREY J.D. (1969a). Mechanical consequences of varying the mineral content of bone. *J. Biomechanics*, No.2, pp. 1-11

CURREY J.D. (1970). The mechanical properties of bone. *Clin. Orthopaed.*, 73, pp. 210-231

CURREY J.D. (1975). Mechanical design in organisms. *Edward Arnold, London*

DERBY B., HILLS D., RUIZ C. (1992). Material for engineering. *Longman Scientific & Technical, England*

GHAI R.C., BHALLA V.V.K., LUNAWAT A.K.(1982). Relations between mechanical properties of human femoral bones. *J. Institution Engineers, India,*

GIBSON R.J. (1995). Experimental investigations of the degradation of ceramic composites in aggressive thermomechanical environments. *Dissertation, University of Glasgow*

GIBSON R.J, THOMSON R.D. (1995). Generation and effect of thermal transient in ceramic composites. *J. Composite Structures*, Vol.32, No.1-4, pp 435-444

GREEN M.A (1978). Stab wound dynamics-A recording technique for use in medico-legal investigations. *J. Forens. Sci. Soc*

GRIFFITH A.A (1920). The phenomena of rupture and flow in solids. *Phil.Trans.Roy.Soc.*, A221, pp. 163-198

GROSSMAN J.D. (1969). The anatomy of the domestic animals. *Fourth Edition, Saunders W.B. Company*

GUO X. E., McMAHON T.A., KEAVENY T.M., HAYES W.C., GIBSON L.J. (1994). Finite element modelling of damage accumulation in trabecular bone under cyclic loading. *J. Biomechanics*, Vol.27, No.2, pp. 145-155

HEATHERINGTON J.G. (1995). Energy and momentum change during ballistic perforation. *Int.J. Impact Eng.*, Vol.18, No.3, pp. 319-337

HOGAN H.A. (1988). Finite element micromechanics of compact bone tissue as a fibre reinforced composite material. *American Mechanical Engineers Division*, pp. 171-174

IRWIN G.R (1973). *Applied Material Res.* 3, pp. 65

JACKSON A.P. (1992). Bone, nacre and other ceramics. *Biomechanics Material, A practical Approach*, edited by Vincent J.F.V, *Oxford University Press*

KACHANOV L.M. (1986). Introduction to continuum damage mechanics. *Martinus Nijhoff Publishers, Dordrecht*

KATZ J.L., YOON H.S. (1984). The structure and anisotropic mechanical properties of bone. *IEEE Trans. Biomedical Engineering*, Vol.31, No.12, pp. 878-834

KELLER T.S., MAO Z., SPENGLER D.M. (1990). Young's modulus, bending strength, and tissue physical properties of human compact bone. *J. Orthopaedic research*, Vol.8, pp. 592-602

KNIGHT B. (1975). The dynamics of stab wounds. *Forensic Science*, 6, pp. 249-255

KRAJCINOVIC D. (1979). Distributed damage theory of beams in pure bending. *Trans. ASME*, Vol.46, pp. 592-596

KRAJCINOVIC D. (1981). The continuous damage theory of brittle materials. *J.Applied Mechanics*, Vol.48, pp. 809-824

KRAJCINOVIC D. (1985). Continuum damage mechanics and its application in biomechanics. *Advances in Bioengineering*, edited by Langrana N.A

KRAJCINOVIC D., FANELLA D. (1986). A micromechanical damage model for concrete. *Eng. Fracture Mech.*, Vol.25, pp. 585-596

KRAJCINOVIC D., MASTILOVIC S. (1995). Some fundamental issues of damage mechanics. *Mechanics Of Materials*, ELSEVIER, 21, pp. 217-230

KRAJCINOVIC D. (1996). Damage mechanics. *Elsevier, Oxford*

LAKES R. (1985). Generalised continuum mechanics of compact bone. *Advances in Bioengineering*, edited by Langrana N.A

MACAULAY M. (1987). Introduction to impact engineering. *Chapman And Hall, New York*

McCAFFERTY J & HANCOCK J (1992). Experimental and computational models of the deformation of ceramic composites by microcracking. *In Pro, 1st Asian-Pacific Conf.*

McELHANEY J.H. (1966). Dynamic response of bone and muscle tissue. *J. appl. Physiol.*, 19, pp. 1231-1236

MECHOLSKY J.J. (1986). Evaluation of mechanical property testing methods for ceramic matrix composites. *Cer Bul* V65, pp. 315-323

NAFEMS (1991). A finite element primer.

OUCHTERLONY F. (1983). A distributed damage approach to combined bending and axial loading of rock beams. *Mechanical Behaviour Of The Materials*, Pergamon Press, London, Vol.27, pp. 943-961

PARKER G. (1993). Stab resistant body armour test procedure. *PSDB*.

PIEKARSKI K. (1968). Studies of the mechanical properties of bone. *Dissertation, University of Cambridge*

POPE M.H., OUTWATER J.O. (1975). Mechanical properties of bone as a function of position and orientation. *J. Biomech.*, pp. 7:61-66

RIETBERGEN B.V., WEINANS H., HUISKES R., ODGAARD A. (1995). A new method to determine trabecular bone elastic properties and loading using micromechanical finite-element models. *J. Biomechanics*, Vol.28, No.1, pp. 69-81

SEDLIN E.D. (1965). Mechanical properties of bone. *Acta Orthoped. Scand.*, Suppl.83, 1

SEDLIN E.D., HIRSCH C. (1966). Factors affecting the determination of the physical properties of femoral cortical bone. *Acta Orthop. Scand.*, pp. 37:29-48

THIBODEAU G.A., PATTON K.T. (1993). Anatomy and physiology. *International Edition, second edition, Mosby*

TURNER C.H., COWIN S.C. (1987). Dependence of elastic constants of an anisotropic porous material upon porosity and fabric. *J. Material Science*, Vol.22, pp. 3178-3184

VINCENT J.F.V (1982). Structural biomaterials. *The Macmillan Press Ltd*

ZYSSET P.K., CURNIER A. (1996). A 3-d damage model for trabecular bone based on fabric tensors. *J. Biomechanics*, Vol.29, pp. 1549-1558

Appendix

AN EXAMPLE OF ELEMENT DELETION INPUT FILE

```

*HEADING
RSB STATIC RUN
*NODE
101, 0.000, 0.000
117, 0.000, -0.003
1701, 0.030, 0.000
1717, 0.030, -0.003
*NGEN, NSET=X1
101, 117
*NGEN, NSET=X17
1701, 1717
*NFill, NSET=ALLN, BIAS=0.85
X1, X17, 16, 100
*ELEMENT, TYPE=CPE4R, ELSET=MASTERE
101, 101, 102, 202, 201
*ELGEN, ELSET=ALLE
101, 16, 100, 100, 16, 1, 1
*****
*SOLID SECTION, ELSET=ALLE, MATERIAL=ELASLANX
0.01
*MATERIAL, NAME=ELASLANX
*DENSITY
2700.
*ELASTIC
130.E9, 0.3
*BOUNDARY
X1, XSYMM
1717, 2
*****
STEP 1 *
*STEP, NLGEOM
*STATIC
*RESTART, WRITE
*BOUNDARY
101, 2, 2, -0.0001
*END STEP
*****
STEP 2 *
*STEP, NLGEOM
*STATIC
*RESTART, WRITE
*BOUNDARY
101, 2, 2, -0.0002
*END STEP
*****
STEP 3 *
*STEP, NLGEOM
*STATIC
*RESTART, WRITE
*BOUNDARY
101, 2, 2, -0.00032
*END STEP
*****
STEP 4 *
*STEP, NLGEOM
*STATIC
*RESTART, WRITE
*MODEL CHANGE, TYPE=ELEMENT, REMOVE
116
*BOUNDARY
101, 2, 2, -0.0004
*END STEP
*****
STEP 5 *
*STEP, NLGEOM
*STATIC
*MODEL CHANGE, TYPE=ELEMENT, REMOVE

```

```

216, 316, 416, 516, 616, 716
115, 215, 315, 415, 515
114, 214
*RESTART, WRITE
*BOUNDARY
101, 2, 2, -0.0005
*END STEP
***** STEP 6 *
*STEP, NLGEOM
*STATIC
*MODEL CHANGE, TYPE=ELEMENT, REMOVE
615, 715
314, 414, 514, 614, 714
113, 213, 313, 413, 513, 613
112, 212, 312, 412, 512
111, 211, 311
*RESTART, WRITE
*BOUNDARY
101, 2, 2, -0.0006
*END STEP
***** STEP 7 *
*STEP, NLGEOM
*STATIC
*MODEL CHANGE, TYPE=ELEMENT, REMOVE
713
612, 712
411, 511, 611
110, 210, 310, 410, 510, 610
109, 209, 309, 409, 509
108, 208, 308
*RESTART, WRITE
*BOUNDARY
101, 2, 2, -0.0007
*END STEP
***** STEP 8 *
*STEP, NLGEOM
*STATIC
*MODEL CHANGE, TYPE=ELEMENT, REMOVE
609
408, 508, 608
107, 207, 307, 407, 507
106, 206, 306, 406
*RESTART, WRITE
*BOUNDARY
101, 2, 2, -0.0008
*END STEP
***** STEP 9 *
*STEP, NLGEOM
*STATIC
*MODEL CHANGE, TYPE=ELEMENT, REMOVE
506
105, 205, 305, 405
104, 204, 304
*RESTART, WRITE
*BOUNDARY
101, 2, 2, -0.0009
*END STEP
***** STEP 10*
*STEP, NLGEOM
*STATIC
*MODEL CHANGE, TYPE=ELEMENT, REMOVE
103, 203, 303
*RESTART, WRITE
*BOUNDARY

```

101, 2, 2, -0.0010

*END STEP

EXAMPLE OF INPUT FILE FOR BEND BAR (MODELLED WITH 100 ELEMENTS)

*HEADING

TESTING ON 100 ELEMENTS BEND BAR

*RESTART,WRITE, NUM=50

*PREPRINT,ECHO=NO,HISTORY=NO,MODEL=NO

*NODE

1,	0.,	0.
2,	0.0015,	0.
3,	0.003,	0.
4,	0.0045,	0.
5,	0.006,	0.
6,	0.0075,	0.
7,	0.009,	0.
8,	0.0105,	0.
9,	0.012,	0.
10,	0.0135,	0.
11,	0.015,	0.
12,	0.0165,	0.
13,	0.018,	0.
14,	0.0195,	0.
15,	0.021,	0.
16,	0.0225,	0.
17,	0.024,	0.
18,	0.0255,	0.
19,	0.027,	0.
20,	0.0285,	0.
21,	0.03,	0.
22,	0.,	0.0006
23,	0.0015,	0.0006
24,	0.003,	0.0006
25,	0.0045,	0.0006
26,	0.006,	0.0006
27,	0.0075,	0.0006
28,	0.009,	0.0006
29,	0.0105,	0.0006
30,	0.012,	0.0006
31,	0.0135,	0.0006
32,	0.015,	0.0006
33,	0.0165,	0.0006
34,	0.018,	0.0006
35,	0.0195,	0.0006
36,	0.021,	0.0006
37,	0.0225,	0.0006
38,	0.024,	0.0006
39,	0.0255,	0.0006
40,	0.027,	0.0006
41,	0.0285,	0.0006
42,	0.03,	0.0006
43,	0.,	0.0012
44,	0.0015,	0.0012
45,	0.003,	0.0012
46,	0.0045,	0.0012
47,	0.006,	0.0012
48,	0.0075,	0.0012
49,	0.009,	0.0012
50,	0.0105,	0.0012
51,	0.012,	0.0012
52,	0.0135,	0.0012
53,	0.015,	0.0012
54,	0.0165,	0.0012
55,	0.018,	0.0012
56,	0.0195,	0.0012
57,	0.021,	0.0012

58,	0.0225,	0.0012
59,	0.024,	0.0012
60,	0.0255,	0.0012
61,	0.027,	0.0012
62,	0.0285,	0.0012
63,	0.03,	0.0012
64,	0.,	0.0018
65,	0.0015,	0.0018
66,	0.003,	0.0018
67,	0.0045,	0.0018
68,	0.006,	0.0018
69,	0.0075,	0.0018
70,	0.009,	0.0018
71,	0.0105,	0.0018
72,	0.012,	0.0018
73,	0.0135,	0.0018
74,	0.015,	0.0018
75,	0.0165,	0.0018
76,	0.018,	0.0018
77,	0.0195,	0.0018
78,	0.021,	0.0018
79,	0.0225,	0.0018
80,	0.024,	0.0018
81,	0.0255,	0.0018
82,	0.027,	0.0018
83,	0.0285,	0.0018
84,	0.03,	0.0018
85,	0.,	0.0024
86,	0.0015,	0.0024
87,	0.003,	0.0024
88,	0.0045,	0.0024
89,	0.006,	0.0024
90,	0.0075,	0.0024
91,	0.009,	0.0024
92,	0.0105,	0.0024
93,	0.012,	0.0024
94,	0.0135,	0.0024
95,	0.015,	0.0024
96,	0.0165,	0.0024
97,	0.018,	0.0024
98,	0.0195,	0.0024
99,	0.021,	0.0024
100,	0.0225,	0.0024
101,	0.024,	0.0024
102,	0.0255,	0.0024
103,	0.027,	0.0024
104,	0.0285,	0.0024
105,	0.03,	0.0024
106,	0.,	0.003
107,	0.00150001,	0.003
108,	0.003,	0.003
109,	0.0045,	0.003
110,	0.006,	0.003
111,	0.0075,	0.003
112,	0.009,	0.003
113,	0.0105,	0.003
114,	0.012,	0.003
115,	0.0135,	0.003
116,	0.015,	0.003
117,	0.0165,	0.003
118,	0.018,	0.003
119,	0.0195,	0.003
120,	0.021,	0.003
121,	0.0225,	0.003

122,	0.024,	0.003
123,	0.0255,	0.003
124,	0.027,	0.003
125,	0.0285,	0.003
126,	0.03,	0.003

*ELEMENT, TYPE=CPE4R , ELSET=CERAMIC

1,	1,	2,	23,	22
2,	2,	3,	24,	23
3,	3,	4,	25,	24
4,	4,	5,	26,	25
5,	5,	6,	27,	26
6,	6,	7,	28,	27
7,	7,	8,	29,	28
8,	8,	9,	30,	29
9,	9,	10,	31,	30
10,	10,	11,	32,	31
11,	11,	12,	33,	32
12,	12,	13,	34,	33
13,	13,	14,	35,	34
14,	14,	15,	36,	35
15,	15,	16,	37,	36
16,	16,	17,	38,	37
17,	17,	18,	39,	38
18,	18,	19,	40,	39
19,	19,	20,	41,	40
20,	20,	21,	42,	41
21,	22,	23,	44,	43
22,	23,	24,	45,	44
23,	24,	25,	46,	45
24,	25,	26,	47,	46
25,	26,	27,	48,	47
26,	27,	28,	49,	48
27,	28,	29,	50,	49
28,	29,	30,	51,	50
29,	30,	31,	52,	51
30,	31,	32,	53,	52
31,	32,	33,	54,	53
32,	33,	34,	55,	54
33,	34,	35,	56,	55
34,	35,	36,	57,	56
35,	36,	37,	58,	57
36,	37,	38,	59,	58
37,	38,	39,	60,	59
38,	39,	40,	61,	60
39,	40,	41,	62,	61
40,	41,	42,	63,	62
41,	43,	44,	65,	64
42,	44,	45,	66,	65
43,	45,	46,	67,	66
44,	46,	47,	68,	67
45,	47,	48,	69,	68
46,	48,	49,	70,	69
47,	49,	50,	71,	70
48,	50,	51,	72,	71
49,	51,	52,	73,	72
50,	52,	53,	74,	73
51,	53,	54,	75,	74
52,	54,	55,	76,	75
53,	55,	56,	77,	76
54,	56,	57,	78,	77
55,	57,	58,	79,	78
56,	58,	59,	80,	79
57,	59,	60,	81,	80
58,	60,	61,	82,	81

59,	61,	62,	83,	82
60,	62,	63,	84,	83
61,	64,	65,	86,	85
62,	65,	66,	87,	86
63,	66,	67,	88,	87
64,	67,	68,	89,	88
65,	68,	69,	90,	89
66,	69,	70,	91,	90
67,	70,	71,	92,	91
68,	71,	72,	93,	92
69,	72,	73,	94,	93
70,	73,	74,	95,	94
71,	74,	75,	96,	95
72,	75,	76,	97,	96
73,	76,	77,	98,	97
74,	77,	78,	99,	98
75,	78,	79,	100,	99
76,	79,	80,	101,	100
77,	80,	81,	102,	101
78,	81,	82,	103,	102
79,	82,	83,	104,	103
80,	83,	84,	105,	104
81,	85,	86,	107,	106
82,	86,	87,	108,	107
83,	87,	88,	109,	108
84,	88,	89,	110,	109
85,	89,	90,	111,	110
86,	90,	91,	112,	111
87,	91,	92,	113,	112
88,	92,	93,	114,	113
89,	93,	94,	115,	114
90,	94,	95,	116,	115
91,	95,	96,	117,	116
92,	96,	97,	118,	117
93,	97,	98,	119,	118
94,	98,	99,	120,	119
95,	99,	100,	121,	120
96,	100,	101,	122,	121
97,	101,	102,	123,	122
98,	102,	103,	124,	123
99,	103,	104,	125,	124
100,	104,	105,	126,	125

*SOLID SECTION, ELSET=CERAMIC, MATERIAL=LUXIDE
0.010

*MATERIAL, NAME=LUXIDE

*DENSITY

2740.

*USER MATERIAL, CONSTANTS=3

132.E9,0.29,300E6

*DEPVAR

4, DELETE=4

*NSET,NSET=XSYSM

1,22,43,64,85,106

*BOUNDARY

XSYSM,XSYMM

21,2,2

*STEP

*DYNAMIC, EXPLICIT

,0.1

*BOUNDARY, TYPE=VELOCITY

106,2,2,-0.04

*END STEP

EXAMPLE OF INPUT FILE FOR T-SECTION (MODELLED WITH 79 ELEMENTS)

*HEADING

THREE POINT BENDING UNDER LOAD FOR T-SECTION

*RESTART,WRITE, NUM=50

*PREPRINT,ECHO=NO,HISTORY=NO,MODEL=NO

*NODE

1,	0.,	0.
2,	0.,	-0.00072
3,	0.,	-0.00144
4,	0.,	-0.00216
5,	0.,	-0.00288
6,	0.,	-0.0036
7,	0.0051,	0.
8,	0.0051,	-0.00072
9,	0.0051,	-0.00144
10,	0.0051,	-0.00216
11,	0.0051,	-0.00288
12,	0.0051,	-0.0036
13,	0.0102,	0.
14,	0.0102,	-0.00072
15,	0.0102,	-0.00144
16,	0.0102,	-0.00216
17,	0.0102,	-0.00288
18,	0.0102,	-0.0036
19,	0.0153,	0.
20,	0.0153,	-0.00072
21,	0.0153,	-0.00144
22,	0.0153,	-0.00216
23,	0.0153,	-0.00288
24,	0.0153,	-0.0036
25,	0.0204,	0.
26,	0.0204,	-0.00072
27,	0.0204,	-0.00144
28,	0.0204,	-0.00216
29,	0.0204,	-0.00288
30,	0.0204,	-0.0036
31,	0.0255,	0.
32,	0.0255,	-0.00072
33,	0.0255,	-0.00144
34,	0.0255,	-0.00216
35,	0.0255,	-0.00288
36,	0.0255,	-0.0036
37,	0.0306,	0.
38,	0.0306,	-0.00072
39,	0.0306,	-0.00144
40,	0.0306,	-0.00216
41,	0.0306,	-0.00288
42,	0.0306,	-0.0036
43,	0.0357,	0.
44,	0.0357,	-0.00072
45,	0.0357,	-0.00144
46,	0.0357,	-0.00216
47,	0.0357,	-0.00288
48,	0.0357,	-0.0036
49,	0.0375,	-0.0036
50,	0.0375,	-0.00288
51,	0.0375,	-0.00216
52,	0.0375,	-0.00144
53,	0.0375,	-0.00072
54,	0.0375,	0.
55,	0.03705,	-0.0036
56,	0.03705,	-0.00288

57,	0.03705,	-0.00216
58,	0.03705,	-0.00144
59,	0.03705,	-0.00072
60,	0.03705,	0.
61,	0.0366,	-0.0036
62,	0.0366,	-0.00288
63,	0.0366,	-0.00216
64,	0.0366,	-0.00144
65,	0.0366,	-0.00072
66,	0.0366,	0.
67,	0.03615,	-0.0036
68,	0.03615,	-0.00288
69,	0.03615,	-0.00216
70,	0.03615,	-0.00144
71,	0.03615,	-0.00072
72,	0.03615,	0.
84,	0.0375,	-0.00553333
85,	0.03705,	-0.00553333
86,	0.0366,	-0.00553333
87,	0.03615,	-0.00553333
88,	0.0357,	-0.00553333
89,	0.0375,	-0.00746667
90,	0.03705,	-0.00746667
91,	0.0366,	-0.00746667
92,	0.03615,	-0.00746667
93,	0.0357,	-0.00746667
94,	0.0375,	-0.0094
95,	0.03705,	-0.0094
96,	0.0366,	-0.0094
97,	0.03615,	-0.0094
98,	0.0357,	-0.0094
99,	0.0375,	-0.0113333
100,	0.03705,	-0.0113333
101,	0.0366,	-0.0113333
102,	0.03615,	-0.0113333
103,	0.0357,	-0.0113333
104,	0.0375,	-0.0132667
105,	0.03705,	-0.0132667
106,	0.0366,	-0.0132667
107,	0.03615,	-0.0132667
108,	0.0357,	-0.0132667
109,	0.0375,	-0.0152
110,	0.03705,	-0.0152
111,	0.0366,	-0.0152
112,	0.03615,	-0.0152
113,	0.0357,	-0.0152

*ELEMENT, TYPE=CPE4R , ELSET=CERAMIC

1,	1,	2,	8,	7
2,	2,	3,	9,	8
3,	3,	4,	10,	9
4,	4,	5,	11,	10
5,	5,	6,	12,	11
6,	7,	8,	14,	13
7,	8,	9,	15,	14
8,	9,	10,	16,	15
9,	10,	11,	17,	16
10,	11,	12,	18,	17
11,	13,	14,	20,	19
12,	14,	15,	21,	20
13,	15,	16,	22,	21
14,	16,	17,	23,	22
15,	17,	18,	24,	23
16,	19,	20,	26,	25

17,	20,	21,	27,	26
18,	21,	22,	28,	27
19,	22,	23,	29,	28
20,	23,	24,	30,	29
21,	25,	26,	32,	31
22,	26,	27,	33,	32
23,	27,	28,	34,	33
24,	28,	29,	35,	34
25,	29,	30,	36,	35
26,	31,	32,	38,	37
27,	32,	33,	39,	38
28,	33,	34,	40,	39
29,	34,	35,	41,	40
30,	35,	36,	42,	41
31,	37,	38,	44,	43
32,	38,	39,	45,	44
33,	39,	40,	46,	45
34,	40,	41,	47,	46
35,	41,	42,	48,	47
36,	49,	50,	56,	55
37,	50,	51,	57,	56
38,	51,	52,	58,	57
39,	52,	53,	59,	58
40,	53,	54,	60,	59
41,	55,	56,	62,	61
42,	56,	57,	63,	62
43,	57,	58,	64,	63
44,	58,	59,	65,	64
45,	59,	60,	66,	65
46,	61,	62,	68,	67
47,	62,	63,	69,	68
48,	63,	64,	70,	69
49,	64,	65,	71,	70
50,	65,	66,	72,	71
51,	67,	68,	47,	48
52,	68,	69,	46,	47
53,	69,	70,	45,	46
54,	70,	71,	44,	45
55,	71,	72,	43,	44
56,	49,	55,	85,	84
57,	55,	61,	86,	85
58,	61,	67,	87,	86
59,	67,	48,	88,	87
60,	84,	85,	90,	89
61,	85,	86,	91,	90
62,	86,	87,	92,	91
63,	87,	88,	93,	92
64,	89,	90,	95,	94
65,	90,	91,	96,	95
66,	91,	92,	97,	96
67,	92,	93,	98,	97
68,	94,	95,	100,	99
69,	95,	96,	101,	100
70,	96,	97,	102,	101
71,	97,	98,	103,	102
72,	99,	100,	105,	104
73,	100,	101,	106,	105
74,	101,	102,	107,	106
75,	102,	103,	108,	107
76,	104,	105,	110,	109
77,	105,	106,	111,	110
78,	106,	107,	112,	111
79,	107,	108,	113,	112

```
*SOLID SECTION, ELSET=CERAMIC, MATERIAL=LUXIDE
0.010
*MATERIAL, NAME=LUXIDE
*DENSITY
2740.
*USER MATERIAL, CONSTANTS=3
140.E9, 0.29, 30E6
*DEPVAR
4, DELETE=4
*****
*NSET, NSET=XSYSM
49,50,51,52,53,54,84,89,94,99
104,109
*BOUNDARY
XSYSM, XSYMM
6,2,2
*****
*STEP
*DYNAMIC, EXPLICIT
,0.1
*BOUNDARY, TYPE=VELOCITY
54,2,2,-0.04
*END STEP
```


VUMAT SUBROUTINE FILE for CHAPTER 4

```

subroutine vumat(
C Read only (unmodifiable) variables -
1 nblock, ndir, nshr, nstatev, nfieldv, nprops, lannea
2 stepTime, totalTime, dt, cmname, coordMp, charLength
3 props, density, strainInc, relSpinInc,
4 tempOld, stretchOld, defgradOld, fieldOld,
5 stressOld, stateOld, enerInternOld, enerInelasOld,
6 tempNew, stretchNew, defgradNew, fieldNew,
C Write only (modifiable) variables -
7 stressNew, stateNew, enerInternNew, enerInelasNew)

C
C   include 'vaba_param.inc'

C
C   dimension props(nprops), density(nblock), coordMp(nblo
1 charLength(nblock), strainInc(nblock,ndir+nshr),
2 relSpinInc(nblock,nshr), tempOld(nblock),
3 stretchOld(nblock,ndir+nshr), defgradOld(nblock,ndir
4 fieldOld(nblock,nfieldv), stressOld(nblock,ndir+nshr
5 stateOld(nblock,nstatev), enerInternOld(nblock),
6 enerInelasOld(nblock), tempNew(nblock),
7 stretchNew(nblock,ndir+nshr), defgradNew(nblock,ndir
8 fieldNew(nblock,nfieldv), stressNew(nblock,ndir+nshr
9 stateNew(nblock,nstatev), enerInternNew(nblock),
1 enerInelasNew(nblock)

C
C   character*8 cmname
C
C   open(unit=15,file='/home/mech/jsoh/vumat/isovuout.add')
C
C The specimen constants: depth,d=0.003, length,L=0.06,
C Young modulus,E=132GPa and Possion ratio,anu=0.29
C matrix stress=150MPa
C
C   E0      = props(1)
C   anu     = props(2)
C   smm     = props(3)
C Calculate twice the initial shear modulus and Lamé constant
C   twoG0   = E0/(1. + anu)
C   ala0    = anu*twoG0/(1. -2*anu)
C
C Loop on the number of data blocks.
C
C   do 100 i = 1,nblock
C
C
C Calculate the new strain tensor.
C   stateNew(i,1) = stateOld(i,1) + strainInc(i,1)
C   stateNew(i,2) = stateOld(i,2) + strainInc(i,2)
C   stateNew(i,3) = stateOld(i,3) + strainInc(i,3)
C   stateNew(i,4) = stateOld(i,4) + strainInc(i,4)
C
C
C Update the elastic Secant modulus according to some damage
C
C
C   if (stateNew(i,1).lt.(smm/E0)) then
C     D = 0.0
C   else
C     D = 100*stateNew(i,1) - 0.076
C   endif
C

```

```

C
C
      if (D.gt.1.) then
      D = 1.0
      endif
C
      E = E0*(1. -D)
      twoG = E/(1.0 + anu)
      ala  = anu*twoG/(1.0 - 2*anu)
C
C
      trace = stateNew(i,1) + stateNew(i,2) + stateNew(i,3)
      stressNew(i,1) = twoG*stateNew(i,1) + ala*trace
      stressNew(i,2) = twoG0*stateNew(i,2) + ala0*trace
      stressNew(i,3) = twoG0*stateNew(i,3) + ala0*trace
      stressNew(i,4) = twoG0*stateNew(i,4)
C
C
      100  continue
C
      return
      end

```